Electronic Transport in Semiconductor Nanocrystal Thin Films

A DISSERTATION
SUBMITTED TO THE FACULTY OF THE GRADUATE SCHOOL
OF THE UNIVERSITY OF MINNESOTA
BY

Brian T. Benton

IN PARTIAL FULFILLMENT OF THE REQUIREMENTS
FOR THE DEGREE OF
DOCTOR OF PHILOSOPHY

Prof. Stephen A. Campbell, Adviser

June 2018

To Grandpa Denny

Acknowledgements

I would like to acknowledge all the support I've received in getting to this point. I never could have gotten here on my own, and I owe a great deal to so many people. First, I need to thank my adviser, Prof. Campbell, for all his assistance, guidance, and patience throughout the last seven years. I could not be more grateful for the opportunity he gave me to join his group when I was first starting in graduate school. The generosity he has shown with his time and insight through all the challenges made them far easier to overcome. I am a better student, scientist, and person today because of his mentorship.

I also want to thank my committee, Prof. Ruden, Prof. Stadler, and Prof. Kortshagen most specifically, for their willingness to offer their time and energy for this thesis. Prof. Kortshagen welcomed me into his lab, and without him, none of this would have been possible. The knowledge and enthusiasm he has for this work drives all of us to accomplish more, and the work environment he has fostered in his research group made the time spent working and analyzing data a more enjoyable experience. Prof. Ruden and Prof. Stadler were both exceptional teachers for the classes I was fortunate to take from them, and I will always remember them for their kindness and for always demanding the best from me. In addition, I would also like to make special thanks for Prof. Aydil and Prof. Shklovskii, who both contributed greatly to this work, both directly and indirectly.

The excellent support and knowledge provided by all the staff at the University of Minnesota labs made this work flow much more smoothly than it otherwise might have. The scientists and technicians in the Characterization Facility were always there to provide training and answer questions and inspired my curiosity in learning more about the nature of materials. The machinists in the CSE machine shop always provided service and results above and beyond anything I could have imagined. The support I received from the MNC staff, both in the lab and in the office, was unbelievable and made working in the cleanroom a really enjoyable experience.

The students and postdocs that I have been privileged to work with have made this experience truly special, and I will always remember them for their intelligence, determination, and hard work, but mostly for all the conversations and experiences we've had together that my graduate work so fun and memorable. I'd specifically like to mention Rick Liptak, Sreejith Karthikeyan, Brian Olmsted, Forrest Johnson, Liyuan Zhang, Jeslin Wu, and Ting Chen for being there through my earlier years when I had no idea what I was doing, for being patient and generous with their time, and for providing such great examples for me to follow. The other students in Prof. Kortshagen's lab, especially Ben Greenberg, Katharine Hunter, and Sam Ehrenberg, welcomed me into their group and gave me more support than I could have expected. I learned so much from them and enjoyed all the time we spent together. My officemates for the last several years, Mandip Sibakoti, Sehyun Hwang, and Tim Bontrager have made coming into work fun and interesting every single day, and their discussions and humor always got me through difficult times.

Finally, I need to thank all my friends and family for being there for me long before I ever decided to go to graduate school and still being there for me now. My friends have always been there to remind me that there is more to life than the lab and to enjoy every second we have together. My oldest friend Kevin has always been a supportive and caring friend that I can count on through anything and who inspires me every day. He may not have gotten a mention in my Eagle Scout ceremony, but he's definitely getting one now. My entire family has always supported me and given me the confidence to do whatever I wanted. I am lucky to have all of them. My sister, Julie, has always been there to lead the way and set the bar for me to reach for. I couldn't have asked for a better sister to grow up with, and I wouldn't be who I am today without her. My parents have always been there to cheer me on, support me, and sometimes give me a bit of a push when I needed it. Their love lets me know that I can do anything. Last, my extraordinary wife, Kirsten, makes all of this so much more special. Her love and support have and will always mean more to me than she will ever know. She inspires me to work harder and be better than I think I can, and her intelligence, kindness, strength and humor are the light that I live by.

Abstract

Semiconductor nanocrystal (NC) thin films have emerged as intriguing materials for low cost synthesis of electronic devices with size-tunable optical and electronic properties that enable unique control over operating characteristics. However, in order to fully realize the potential of these materials so that they can be effectively integrated into useful devices, greater understanding of the electronic transport properties is needed. In particular, the relationship between film morphology, surface chemistry, and disorder leads to unique challenges in engineering the performance of NC-based devices. The standard measurement techniques and modeling schemes developed for bulk semiconductors are not necessarily well suited for these challenges, so a deeper understanding of how they can be applied to semiconductor NC films and how to properly interpret the results is needed.

In this thesis, the electronic conduction in two semiconductor NC material systems was explored. First, ZnO was used as a wide bandgap material that was known to have high native doping levels and electronic conduction that can approach metallic behavior. Atomic layer deposition (ALD) Al_2O_3 was used to passivate thin films of porous ZnO NCs, which have electronic properties that are extremely sensitive to surface oxidation reactions with ambient water vapor. This property was utilized to systematically control the conductivity of ZnO films by photochemically desorbing surface hydroxyl groups in vacuum and performing subsequent electrical measurements *in situ*. With this technique, we observed conductance increases of up to 10^5 and associated changes in transport mechanism between Mott and Efros-Shklovskii variable range hopping regimes. Through this analysis, we were able to determine the role of defect states and NC surface depletion in determining the coupling between NCs.

Second, Ge NCs were studied as a narrow bandgap material with large quantum confinement effects leading to bandgap increases of up to 50%. Thermal admittance spectroscopy (TAS) and field-effect transistor (FET) measurements were used together to study charge injection in these films. We observed a change from electron conduction to hole conduction in Ge NC FETs after infilling with ALD Al_2O_3.

The dominant barrier for transport in these FETs was determined to be minority carrier injection to the channel due to NC charging. Contact material was not observed to have any effect on the FET polarity, which, along with large hysteresis observed in I-V and C-V measurements, indicates that the transport properties are largely dominated by trap states.

Contents

Figures

1 Introduction

1.1 Research Motivation

Semiconductor nanocrystals (NCs) have emerged as promising new materials for electronic,[1–4] optoelectronic,[5–10] and thermoelectric[11–14] applications. The bandgap of these materials can be tuned by adjusting the NC size, enabling a degree of control that is usually only possible with chemical changes in bulk materials. With this tunability, the alignment of energy levels, the density of states, and the optical absorption and emission spectra can all be adjusted to suit the intended application. To fully realize the potential of these materials, however, more knowledge of the physics governing charge transport in NC thin films is necessary. Most applications require conductive films, which means that electronic states between NCs must be strongly coupled to one another. On the other hand, the size-dependent properties that make NCs so interesting also inherently require isolation. Understanding the interaction of these parameters and how they can be made to work together is necessary for further development. To achieve this, we need more detailed knowledge concerning surface engineering in NC thin films and how the charge concentration, density of states, and electronic coupling interact to govern the conductivity.

In particular, this work looks to focus on NC materials that show long-term potential for sustainability and stability, with earth-abundant materials and a low degree of environmental hazard. Work in the Kortshagen group has focused on developing plasma synthesis methods for such materials, with a particular concentration on Group IV materials (Si and Ge) and metal oxides, particularly ZnO, which does not share the same environmental concerns as some other commonly studied II-VI materials like PbSe, PbS, CdSe and CdS. The Group IV materials, in particular, are uniquely suited for our unique plasma synthesis techniques due to the high crystallization temperature associated with these materials,[15] giving our group unique opportunities to explore these important materials in detail. ZnO has shown great potential in applications that require high conductivity, such as replacement films for transparent conducting materials containing rare elements such as indium tin oxide, and thus increasing our understanding the transport properties of ZnO NC films could lead to new technological opportunities.

1.2 Plasma Synthesis of Semiconductor Nanocrystals

Most semiconductor nanocrystals found in the literature are produced using colloidal synthesis techniques.[16,17] The resulting NCs are of high-purity with low size dispersion (standard deviations of 5-10% are typical).[17–21] The mean crystal size can be tuned by adjusting the temperature and/or time of the synthesis process. The resulting NC suspensions can be used for optical measurements directly or deposited onto substrates as films with standard solution process techniques (i.e. spin coating, drop casting, roll-to-roll deposition, ink jet printing, etc.) that can produce dense films, with ordered arrays possible through proper control of the processing.[17,22–26] Such NCs have been shown to achieve high photoluminescent quantum yield (PLQY),[9,27] good electrical conductivity,[28–30] and have been utilized in NC devices from solar cells[7,8,31–33,33] to LEDs[9,10,34–39] to MOSFETs[1–4,40–45] and more.

A significant limitation to colloidal NC techniques, however, is the necessity of using long, electrically insulating ligands to form stable suspensions and avoid NC agglomeration. In order to achieve significant electrical conductivity, the initial ligands must be exchanged for shorter ligands[8,46] or conductive surface passivation.[28] This complicates the processing and forces the engineer to make decisions in processing that may not be desirable for the ultimate utility of the device.

Nonthermal plasma synthesis can avoid these limitations. Generally, a radio frequency (RF) Ar plasma is used to generate high-temperature electrons (~40,000 K) while the gas remains near room temperature. Most of the power from the RF field is absorbed by the electrons. The heavier components (ions and neutrals) absorb very little kinetic energy from collisions with the high-energy electrons. Precursors for the desired material are injected into the plasma with pressures typically maintained in the range of 1-10 Torr. The precursors dissociate and ionize, creating extremely reactive radicals. These nucleate and grow to form the high-purity crystals, and the growing crystals are isolated by Coulomb repulsion due to a buildup of negative charge from collisions with electrons in the plasma. As a result, relatively low size dispersions are achievable, approaching that of colloidal synthesis techniques without the need for ligands. Furthermore, collisions with energetic electrons leads to heating of the NCs providing

sufficient thermal and adatom energy to ensure highly crystalline NCs.[47,48] Following the initial synthesis stage, secondary gases can be introduced to facilitate etching and/or surface passivation[49,50] or to grow core/shell structures in-flight. Finally, in order to achieve measurable conductivities, relatively dense films are required. In some circumstances, NCs can be collected as a loose powder on a stainless steel mesh and then dispersed into solution and functionalized with ligands to continue processing in the same manner as standard colloidal NCs. Some plasma-synthesized NCs have even been found to form stable suspensions without the use of ligands.[51] However, to avoid the use of ligands altogether, the synthesis stage can be carried out upstream of a nozzle through which the gas flow rapidly expands into the low-pressure (<100 mTorr) deposition chamber. The stream of particles can reach supersonic velocities and be collected via inertial impaction as a dense film on top of virtually any chosen substrate that can is scanned below the nozzle.[52,53] An example of this design is shown in Figure 1.1.

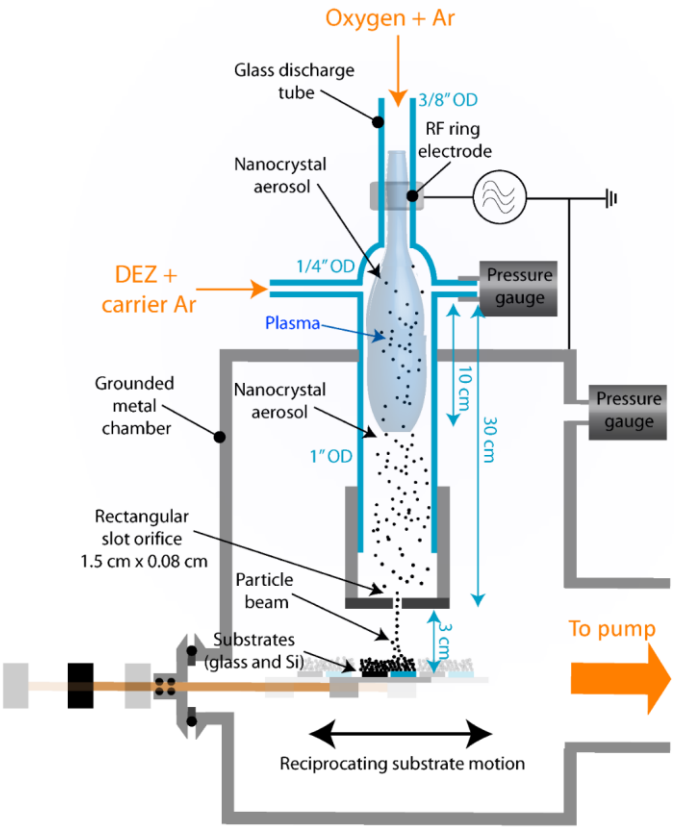

Figure 1.1: Plasma reactor diagram for ZnO NC synthesis. Figure extracted from Thimsen *et al.*[53]

This reactor design has been used for a variety of NC materials. It was initially developed for growing Si NCs,[54] using a 5% SiH_4/95% He precursor gas along with H_2 injected downstream into the afterglow of the plasma for etching and passivation (Figure 1.2). In this work, the same basic design was used to grow two NC materials: ZnO[55] using diethylzinc (DEZ) and O_2 as precursors as developed by Felbier *et al.* (Figure 1.3), and Ge[56] using $GeCl_4$ as a precursor with H_2 injected to encourage nucleation and provide surface treatment as developed by Gresback *et al.*

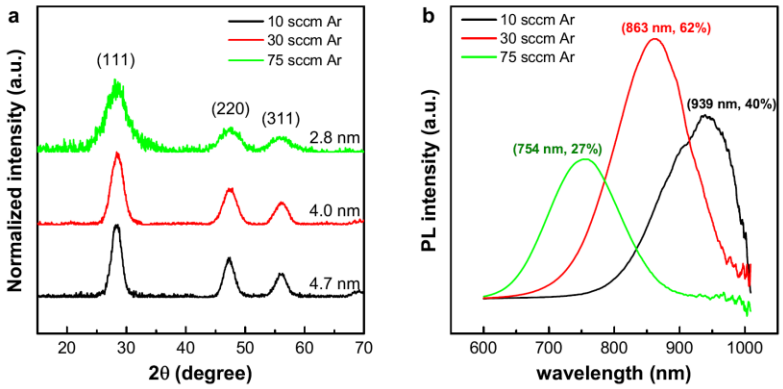

Figure 1.2: XRD and PL spectra for Si NCs. a) XRD spectra for Si NCs showing crystal size tuning from 2.8 nm to 4.7 nm with varying Ar flow rate. b) Corresponding PL intensity showing a maximum PLQY >60%. Figure extracted from Chen.[57]

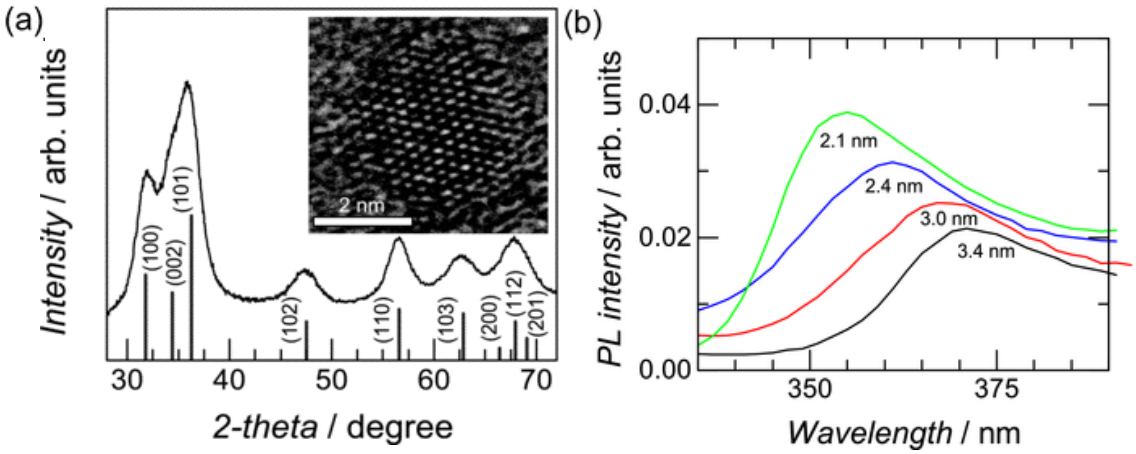

Figure 1.3: XRD and PL spectra for ZnO NCs a) XRD spectra and TEM image for ZnO NC. b) Photoluminescent emission showing exciton wavelength shift with NC size. Figure extracted from Felbier *et al.*[55]

After deposition, further processing is often used to adjust or improve the charge transport characteristics. For example, thermal annealing and UV treatment are both common techniques. We also used atomic layer deposition (ALD) to infill our films with passivating material (most commonly Al_2O_3) to reduce the concentration of surface defects and to alter the dielectric environment of the film. The high aspect ratios that can be conformally coated using ALD make it ideal for filling in the small pores of NC films, even in the case of films on the order of 1 μm thick with pore diameters on the order of 1 nm (Figure 1.4). This process has been used in a variety of NC films and has been shown to improve device performance and stability.[53,58,59]

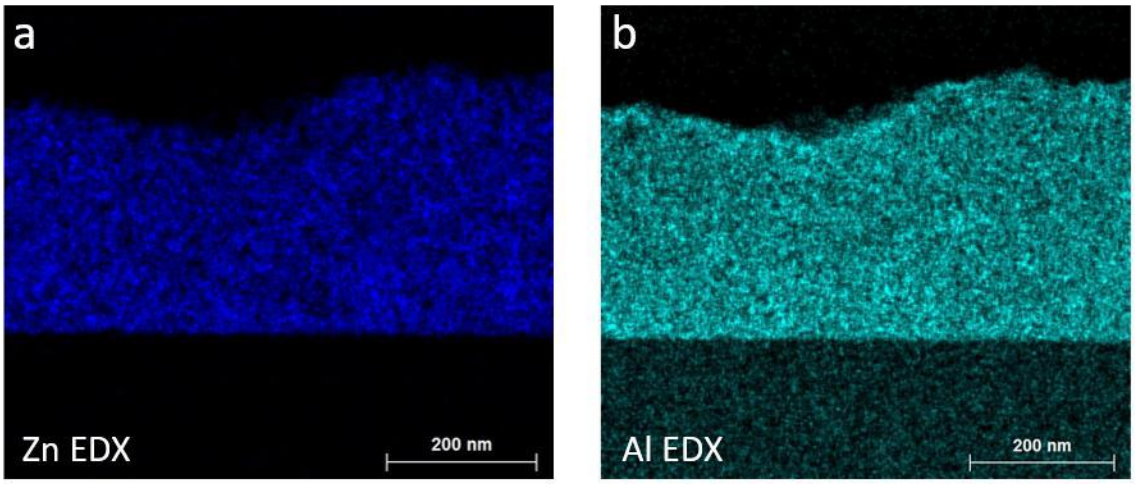

Figure 1.4: STEM-EDX elemental maps of ZnO NC films infilled with ALD Al_2O_3 for a) Zn and b) Al. This shows the penetration of infill throughout the entire depth of the film. Figure extracted from Greenberg.[60]

1.3 Thesis Overview

This thesis focuses on the role of disorder and defect states in electronic transport in NC thin films synthesized using the nonthermal plasma techniques and deposited directly from the gas phase, as discussed in Section 1.2. These methods allow us to bypass the use of insulating ligands for passivation and processing in order to more directly probe the properties of the NCs and their surfaces.

- Chapter 2 provides an overview of electronic theory in semiconductor NCs, including energy level quantization, disorder in NC films and the transport regimes that emerge as a result, and the role of defect states in these processes.
- Chapter 3 summarizes some of the most common electronic measurement techniques for semiconductor NC films. Examples from the literature are included to demonstrate some of the potential applications of these techniques and advantages/disadvantages are discussed. Both dc and frequency-dependent, spectroscopic techniques are covered.
- Chapter 4 covers our work on ZnO NCs, focusing on the role of surface defects in determining the temperature dependence of hopping conduction in these films. This extends the work of the Kortshagen group, specifically that of Elijah Thimsen and Benjamin Greenberg[48,53,61] by focusing on the role of defects in the insulating conduction regime and further understanding the role of surface chemistry and ALD passivation.
- Chapter 5 details our work on Ge NCs, specifically understanding the impact of defect states and surface passivation using atomic layer deposition on the characteristics of field-effect transistors using these films. This work was builds on previous work by the Kortshagen group, with Ge NC synthesis and deposition performed by Katharine Hunter and original FET measurements performed by Zachary Holman.[2]

2 Electronic Transport in Nanocrystal Films

2.1 Introduction

Understanding the fundamental rules of electrical transport has always been necessary for the development of semiconductor devices. In bulk materials, this is generally considered to be governed mainly by critical parameters such as carrier concentration (determined by the density of dopants and traps), mobility (a measure of scattering and loss within the material), and energy barriers (bandgap, Schottky barrier height, and deep trap energies). Most crucially, the electronic properties of a semiconductor can be predictably and reliably tuned by adjusting the concentration of free charge carriers through the intentional introduction of dopant impurities. It is this capability that gives semiconductors their unique position in the world of materials and enable the creation of devices such as transistors, solar cells, LEDs, and more. While these same phenomena are at work in NC films, there are other equally, or often more, important factors to consider.

The electronic structure of NCs differ from their bulk counterparts due to quantum confinement effects, increasing the bandgap and altering the density of states. This is one of the reasons that there is such great interest in developing them for use in a wide range of applications. The bandgap of a bulk material, generally the primary factor in setting the semiconductor's emission and absorption spectra and thus critical to devices such as solar cells, is essentially constant in the bulk. However, the size-tunable bandgap of NCs enables this property to be easily adapted for the specific application. In order to fully realize these advantages, however, further understanding of the complexities involved in NC charge transport is needed. The importance of interfaces and disorder, relevant to any polycrystalline material, is amplified to its extreme in NC films. Inhomogeneity in NC size, spatial distribution, and chemical makeup can cause electrons to spontaneously redistribute, resulting in a realignment of energy levels between NCs due to charging. Combined with the large degree of electron localization usually observed in a NC, this leads to dramatic changes in tunneling rates that often dominate charge transport.

2.2 Quantum Confinement in Nanocrystals

In a bulk crystalline material, the electronic structure consists of states distributed continuously in energy and delocalized spatially across the crystal as a result of the interaction between the periodicity of the crystal structure and the electron wave functions. For a crystalline semiconductor the density of states exhibits a sharp bandgap, an energy range devoid of electronic states. The band of states below this gap is defined as the valence band, whose electrons are localized, participating in chemical bonds. The band above the gap is the conduction band whose electrons are free to move due to a high concentration of unoccupied states.

Semiconductor NCs can range in size from diameters as large as ~100 nm to as small as 1 nm. When the radius becomes small enough, comparable to the size of bound electron-hole pairs in the material (known as the Bohr exciton radius), the bandgap will increase with decreasing crystallite size. This is generally observed near a diameter of 5-10 nm, although the specific values vary depending on the material. Silicon, for example, has a Bohr radius of ~2.4 nm,[62] and previous work has shown tuning of the emission across the full visible spectrum at NC diameters <4 nm, shown in Figure 2.1.

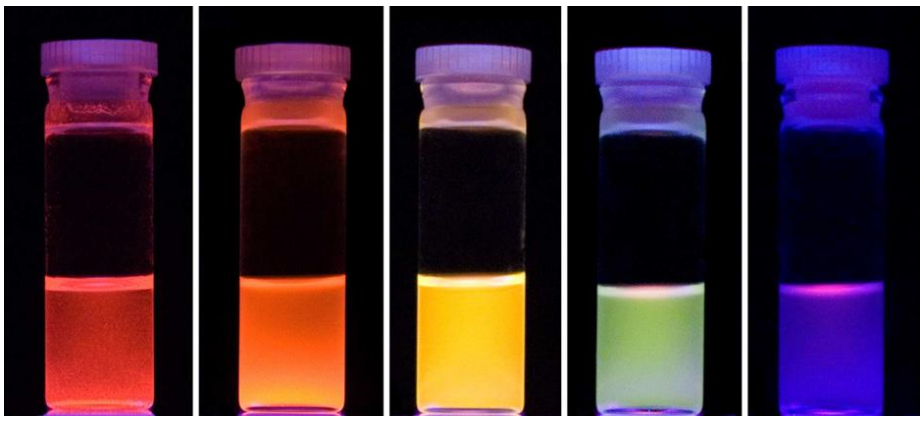

Figure 2.1: Size tunable emission across the visible spectrum for Si NCs. Figure is extracted from Pi *et al*.[63]

In a NC, the lowest energy electrons in the conduction band (or holes in the valence band) have wavelengths comparable to the size of the crystal, such that quantum confinement effects dominate, while higher energy electrons have wavelengths progressively shorter and thus less affected by confinement.

The difference between these bulk and confined energy levels is shown in Figure 2.2. Following this diagram, the first electron excited to the conduction band will fill the confined 1S level, which can also contain at least one additional electron of opposite spin, with more allowed in materials that have multiple degenerate conduction band states. For example, Ge has a four-fold degeneracy allowing 8 electrons in this 1S level, while Si and ZnO have six-fold degeneracy allowing 12 electrons. Further electrons will fill the confined 1P level above this, which has higher degeneracy, and so on upwards. This energy level notation is taken from atomic electron orbitals, which follow similar rules.

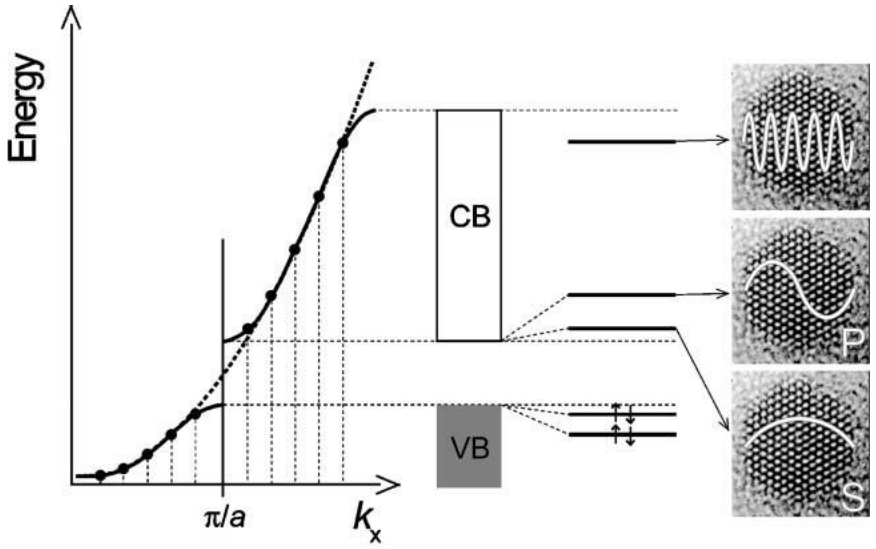

Figure 2.2: Comparison of bulk and quantum confined energy levels, showing electron wavefunction for 1S, 1P, and higher orbitals. Figure is extracted from Vanmaekelbergh and Liljeroth.[64]

This is directly comparable to the simple particle in a box problem, which assumes an infinitely deep square potential well in three dimensions to solve the time-independent Schrödinger equation.

$$\left[-\frac{\hbar^2}{2}\nabla_r \frac{1}{m^*(r)}\nabla_r + V(r)\right]\varphi(r) = E\varphi(r) \tag{2.1}$$

This gives an estimate for the energy levels in a NC of diameter d with an electron (or hole) effective mass m*, here assuming no extra degeneracy in the energy levels.[62] These first three (nonzero) energy levels correspond to 1S (two-fold degenerate), 1P (six-fold degenerate), and 1D (ten-fold degenerate).

$$E_Q(n) = \frac{\hbar^2}{m^* d^2} \begin{cases} 0, & n = 0 \\ 19.74, & n = 1,2 \\ 40.38, & 3 \leq n \leq 8 \\ 66.43, & 9 \leq n \leq 18 \end{cases} \tag{2.2}$$

The simplified picture presented here applies well to isolated NCs. However, when NCs are assembled into films for use in electronic devices, additional factors related to variability in NC size, spacing, and chemical composition must be taken into account. The disorder inherent to these systems leads to what is known as hopping conduction.

2.3 Hopping Conduction in Nanocrystal Films

Due to the limitations of colloidal synthesis and deposition methods, many NCs require surface ligands to stabilize the suspensions during processing. When these NC are deposited as films, these ligands necessarily create gaps between NCs due to their finite lengths.[5,9,16,17,46,65] However, even in the case of direct contact without ligands, there are still large barriers to conduction caused by disorder in the network.[51,53,59,61] In either case, these systems are governed by several key parameters, namely 1) site-to-site energy disorder (characterized by $\Delta\alpha$) which leads to Anderson localization[66] (Figure 2.3), 2) the tunneling rate between NCs (Γ), and 3) the NC charging energy (E_c). Together, these factors lead to hopping conduction, a term general used to describe a phonon-assisted tunneling process that involves a combination of thermal activation and long-range tunneling.

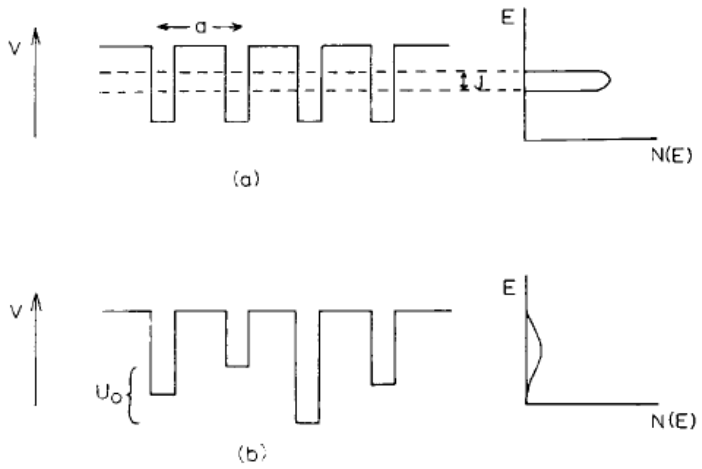

Figure 2.3: Diagram of energy disorder in a periodic lattice. The density of states as a function of energy for each case is also shown. Figure is extracted from Mott.[67]

The energy disorder parameter, $\Delta\alpha$, is primarily related to variation in NC size. Even in the best case, NC size distributions generally exhibit standard deviations of a few to 5% with up to 10-15% not uncommon.[68] Following Equation 2.2, NC energy levels vary as $1/r^2$, therefore a 5-10% variation in diameter would lead to a 10-20% variation in energy. Confinement energies can vary widely, but values in the range of 0.1-0.5 eV are typical, leading to $\Delta\alpha$~0.01-0.1 eV. These values can be larger than thermal broadening even at room temperature but will dominate at low temperatures.

The second important factor is the tunneling rate, Γ, which can be compared to energy scales through the exchange coupling energy $\beta \approx h\Gamma$, where h is Plank's constant, which defines the strength of interaction between neighboring NCs.[64,69] At large distances, the electron wave functions are completely confined to isolated NCs.[70,71] As NCs are brought closer together, either through the removal of long, insulating ligands[46] or direct NC-NC contact, the electron wavefunctions can spread across neighboring NCs or even multiple NCs, leading to delocalization. The tunneling rate is defined as[72]

$$\Gamma \propto exp[-2\Delta x/a] \tag{2.3}$$

where $a = \sqrt{\frac{\hbar^2}{2m^*\Delta E}}$ is the decay length, Δx is the tunneling distance, and ΔE is the barrier height for tunneling. The exponential dependence on distance shows why such strong dependence on interparticle

spacing is observed. The tunneling rate can also be increased by lowering the energy barrier, which requires changing the interparticle medium (i.e. different ligands or infilling with smaller bandgap material).

Increases in this coupling strength can lead to band-like transport and delocalization across multiple NCs. This can be observed as a broadening and red shift in the excitonic feature (transition between the lowest quantum energy levels in the valence and conduction bands) in the absorption spectrum, as observed by Liu *et al.* for films of PbSe NCs.[46] By performing a ligand exchange process, they are able to decrease the interparticle separation and thereby increase the tunneling rate. This is shown Figure 2.4, where the optical bandgap decreases along with ligand length while the measured mobility and coupling energy both increase.

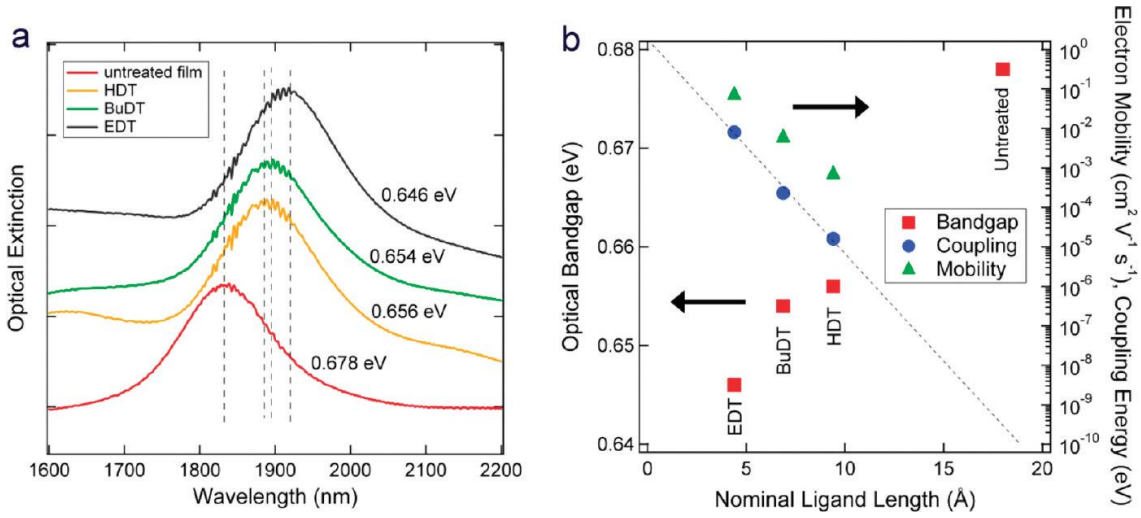

Figure 2.4: Emission and absorption spectra dependence on ligand length. a) Excitonic absorption feature shifts to lower energies upon exchange with shorter ligands. b) This trend also corresponds with an increase in the measured coupling energy and electron mobility. Figure extracted from Liu *et al.*[46]

Similar trends have also been observed by Choi *et al.* by annealing dense films of CdSe NCs to increase the coupling strength (Figure 2.5).[73] In this case, the effect is not explicitly linked to a decrease in distance between NCs, and could be attributed to a change in the barrier height between NCs.

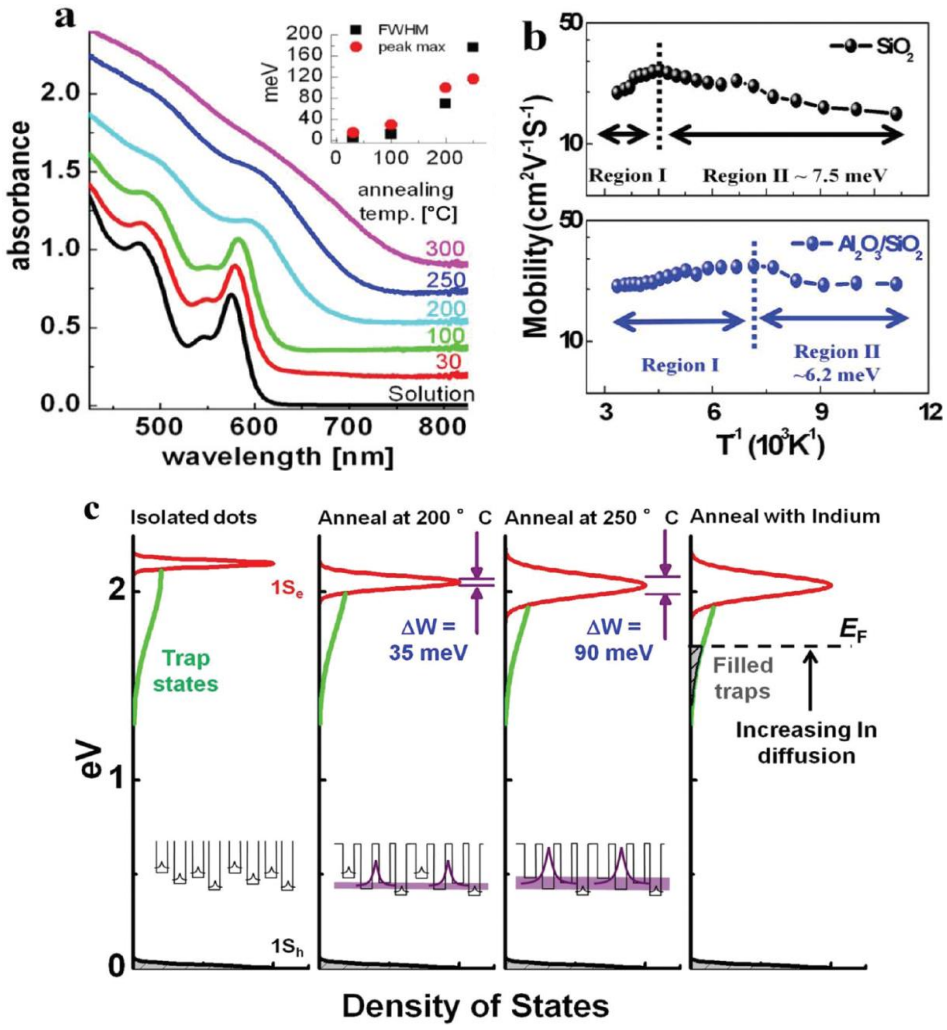

Figure 2.5: Evidence of increased NC coupling energy due to shift in the excitonic absorption feature. a) The negative trend in mobility with increasing temperature b) also supports the theory of band-like transport. c) The diagram shows the increasing coupling with thermal annealing resulting in the formation of extended bands. Figure extracted from Choi *et al.*[73]

Finally, the charging energy accounts for the Coulomb repulsion between excess charge on a NC (from an excess free carrier on a NC without any dopants, for example) and the induced charge at the NC surface due to dielectric polarization between the NC dielectric environment (ε_{NC}) and the dielectric environment of the surrounding medium (ε_i). This results in a charging energy

$$E_c = \frac{e^2}{4\pi\varepsilon_0\varepsilon_i d} \tag{2.4}$$

where $4\pi\varepsilon_0\varepsilon_i d$ is the self-capacitance of the NC. This is correct for a single NC of high dielectric constant ($\varepsilon_{NC} \gg \varepsilon_i$). However, a better result can be obtained by using an effective dielectric constant ε_r in place

of ε_i. In the case of large spacing between NCs (as is the case with long ligands), the canonical Maxwell-Garnett formula applies, which depends on the volume fraction of NC, ϕ.[74]

$$\varepsilon_r = \varepsilon_i \frac{\varepsilon_{NC}+2\varepsilon_i+2\phi(\varepsilon_{NC}-\varepsilon_i)}{\varepsilon_{NC}+2\varepsilon_i-\phi(\varepsilon_{NC}-\varepsilon_i)} \tag{2.5}$$

However, this formula breaks down as the interparticle spacing decreases (or even becomes less than zero in the case of faceted NC arrays). This was shown by Reich and Shklovskii[75] who developed a formula based on the interparticle spacing s, particle diameter d, and a parameter δ defined as $\delta = d\frac{\pi^{6/5}}{2^{11/5}}\left(\frac{\varepsilon_i}{\varepsilon_r}\right)^{6/5}$.

$$\varepsilon_r(s) = \begin{cases} \frac{\pi}{2}\varepsilon_i\left(\frac{d}{2s+2\delta}\right)^{1/3} & s > 0 \\ \varepsilon_{NC}\sqrt{2\frac{|s|+\delta}{d}} & s < 0 \end{cases} \tag{2.6}$$

The difference with this model is highlighted in Figure 2.6, showing good agreement with numerical calculations. This model agrees completely with Maxwell-Garnett in the limit of large separation, as would be expected, but deviates significantly as the separation drops below ~5% of the NC diameter.

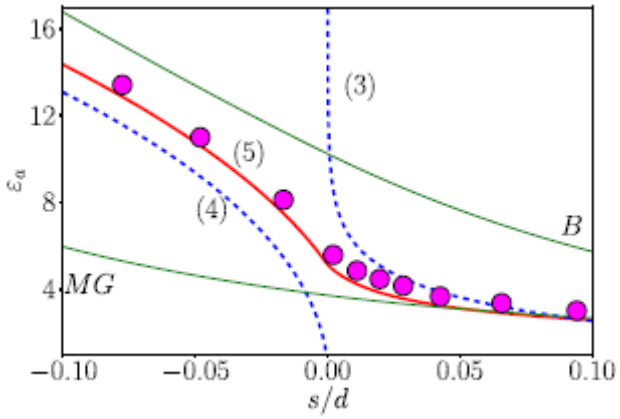

Figure 2.6: Effective medium approximations for NC film dielectric constant. Solid red line (5) indicates values calculated from equation 2.6 for $\varepsilon_i = 1$ and $\varepsilon_{NC} = 30$, with the dashed lines (3 and 4) indicating the limiting cases used to determine this model. Solid lines labeled B and MG show corresponding calculation from Bruggeman and Maxwell-Garnett model, respectively. Circles show numerical calculations from Sareni *et al.*[76] Figure extracted from Reich and Shklovksii.[75]

Returning to the charging energy itself, values can vary widely from entirely negligible in the case of large effective dielectric constant and/or NC diameter to hundreds of meV in the case of sparse metallic

NCs of small size (<5 nm) with free space as the medium ($\varepsilon_r \sim \varepsilon_i = 1$). For example, in the case of 3 nm Ag NCs, a charging energy of 340 meV has been reported.[77]

The general starting point for deriving the resulting equation for hopping transport is modeling the NC network as a Miller-Abrahams resistor network,[78,79] consisting of resistance values that depend exponentially on both tunneling distance and energy difference.

$$R_{ij} = R_0 exp\left[\frac{2r_{ij}}{\xi} + \frac{\varepsilon_{ij}}{k_B T}\right] \tag{2.7}$$

In Equation 2.7, r_{ij} is the distance between sites, ξ is the localization length, ε_{ij} is the energy difference for the transition (relative to the site *i* or the Fermi level), k_B is the Boltzmann constant, T is the temperature, and R_0 is a constant. From here models can be used to describe the distribution of distances and energies, from which the total resistance among all pairs can be minimized. From this, there are broadly three distinct regimes that we concern ourselves with, although special cases can occur, such as 1D or 2D conduction. These regimes are illustrated in Figure 2.8 and correspond to Nearest Neighbor Hopping (NNH), Mott Variable Range Hopping[80] (Mott VRH or M-VRH), and Efros-Shklovskii Variable Range Hopping[78] (ES-VRH). The NNH regime occurs at high temperatures (where thermal energy is sufficient to easily overcome the barrier between neighboring sites) and/or low density of states (where distances for longer-range, lower-energy tunneling become increasingly large). This process has a simple Arrhenius dependence of

$$\rho \propto \exp\left[\frac{\mathrm{E_a}}{\mathrm{k_B T}}\right] \tag{2.8}$$

where E_a is an activation energy. This behavior has been observed in a variety of NC systems.[65,81–85] Kang *et al.* related the measured activation energy to a sum of the charging energy E_c and the site disorder energy $\Delta\alpha$ (which they refer to as E_D), as shown in Figure 2.7.[81]

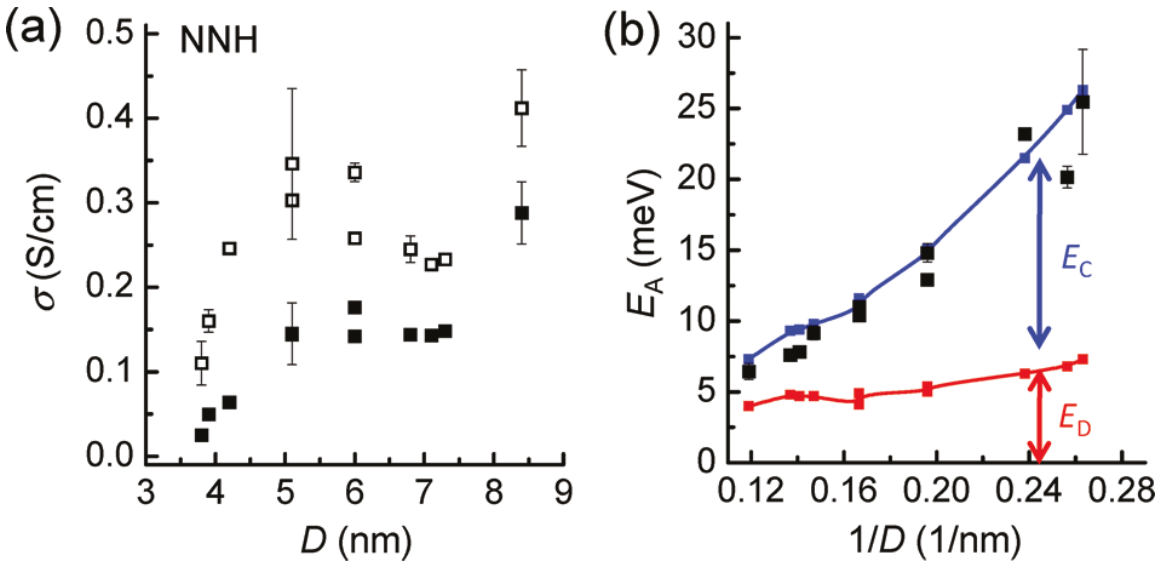

Figure 2.7: Size-dependent conductivity of PbSe NCs and measured hopping energy. a) Conductivity of PbSe NCs is observed to decrease with NC size. b) Extracted activation energy (black squares) is related to a sum of the Coulomb charging energy and site disorder energy. Figure extracted from Kang *et al.*[81]

As the temperature is reduced, the variation in site energy becomes significant and electrons will tunnel over longer distances to find sites with less energy mismatch, corresponding to variable range hopping and resulting in a weaker temperature dependence:

$$\rho \propto \exp\left[\left(\frac{T_0}{T}\right)^m\right] \tag{2.9}$$

with $m < 1$ and T_0 corresponding to a characteristic temperature. In the model proposed by Mott,[86] the density of states (DOS, g) is assumed to be constant at the Fermi level, E_F, from which he derived a value of $m = \frac{1}{4}$ for the case of 3D materials and $T_0 = T_M = \frac{\beta}{k_B g_0 \xi^3}$ where $\beta = 21.2$ and g_0 is the DOS at the Fermi level. In general, however, the DOS is not constant. This is due to the Coulomb interaction between electrons that causes some NCs to obtain a negative charge while others obtain a positive charge as electrons spontaneously redistribute through the network. As a result, the DOS at the Fermi level goes to zero in a parabolic Coulomb gap.[87] The resulting conductivity (ES-VRH) shows a temperature dependence with $m = \frac{1}{2}$ in any dimension and $T_0 = T_{ES} = \frac{Ce^2}{4\pi\varepsilon_0\varepsilon_r k_B \xi}$ where C is a constant generally given as 2.8 for 3D systems and $\varepsilon_0\varepsilon_r$ is the macroscopic dielectric constant of the material.

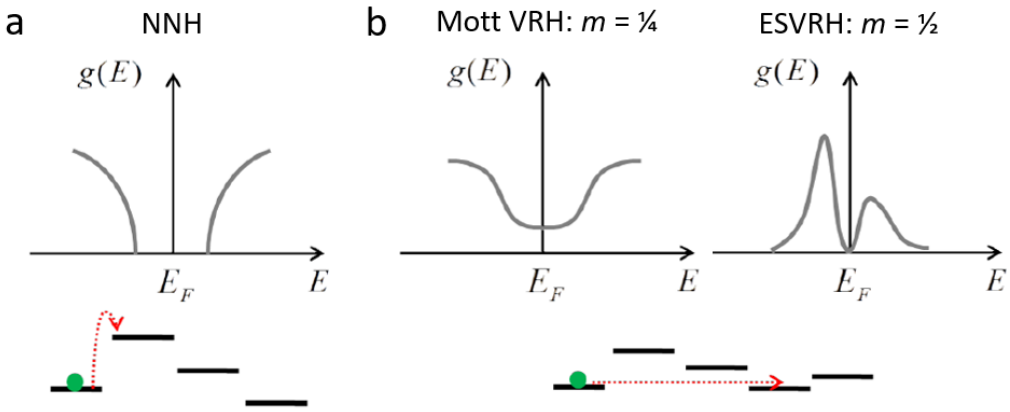

Figure 2.8: Comparison of hopping transport mechanisms. a) Nearest Neighbor Hopping (NNH). b) Variable Range Hopping (VRH) for both Mott and Efros-Shklovskii models. Figure extracted from Chen.[57]

2.4 The Impact of Defect States

Up to now, we have only discussed NC films in an assumed pure state. In reality, a certain concentration of defects will exist in any material, NC or otherwise. These can be errors in the crystal structure such as vacancies, interstitials, and dislocations. It could also be impurities, although current NC synthesis techniques are generally capable of producing crystals of outstanding purity. More commonly associated with NC films are defects associated with bonding at the surface, where the otherwise perfect crystal ends and interfaces with the environment. Any of these defects can potentially lead to a nonzero DOS in the forbidden gap of the material, either at a single energy level or across a distribution of energies. Defect levels near the band edges can easily be filled or emptied due to thermal energy, resulting in a contribution of carriers to the bands, so these are referred to as donors or acceptors. States that lie deeper in the gap will not be readily thermalized and can act as trap states, reducing the carrier concentration. Such states can also enhance the nonradiative recombination rate and produce a corresponding reduction in the photoresponse. This is of particular concern in applications such as LEDs and solar cells. This trap-assisted recombination is described by the Shockley-Read-Hall (SRH) equation[88–90] and leads to a reduction in the internal quantum efficiency η_{int}.

$$\eta_{int} = \frac{1/\tau_{rad}}{1/\tau_{rad}+1/\tau_{SRH}} \tag{2.10}$$

where τ_{rad} is the radiative lifetime and τ_{SRH} is the nonradiative SRH recombination lifetime, defined as

$$\frac{1}{\tau_{SRH}} = \frac{(pn-n_i^2)N_T v_{th}\sigma}{p+n+2\sqrt{N_C N_V}e^{-E_G/2kT}cosh(\frac{E_i-E_T}{kT})} \tag{2.11}$$

In Equation 2.11 the relevant trap parameters N_T and E_T represent the trap state density and energy relative to the conduction (or valence) band, respectively. This effect was observed by Anthony *et al.*[91] with the reduction in defect density, measured by electron paramagnetic resonance (EPR), upon injection of H_2 into the afterglow of the synthesis plasma and a corresponding increase in the photoluminescent quantum yield (Figure 2.9).

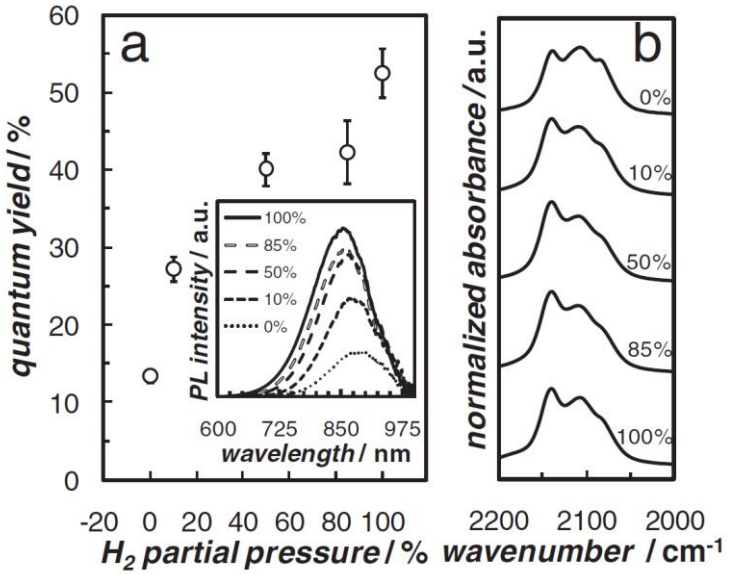

Figure 2.9: Hydrogen passivation of Si NCs. a) Quantum yield as a function of H_2 injection rate. b) The corresponding Fourier Transform Infrared Spectroscopy (FTIR) measurements showing a change in the Si-H_x bonding at the surface of the NCs. Figure extracted from Anthony *et al.*[91]

The transport properties are also affected due to the reduction in free carrier concentration. Almeida *et al.* performed EPR measurements to track the population of Se vacancy defect states in CdSe NCs as a function of controlled doping with Ag.[92] They found an initial increase in the signal as introduction of Ag acted as a donor to raise the Fermi level and charge more of the trap states, followed by a decrease as additional Ag atoms act as acceptors in CdSe and lower the Fermi level, diagramed in Figure 2.10.

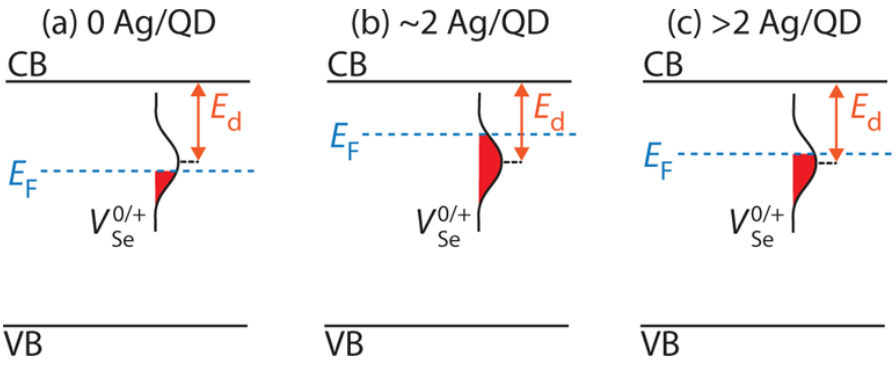

Figure 2.10: Diagram of the population and emptying of Se vacancies in CdSe by the progressive increase of Ag atoms. Figure extracted from Almeida *et al.*[92]

Similarly, Bozyigit *et al.* have performed a variety of studies on transport in NC films with the aim of understanding the influence of traps.[93–96] A summary of one such measurement is shown in Figure 2.11, where they measured trap response in a Schottky diode solar cell fabricated using EDT treated PbS NCs. They observed a shift in the Fermi level after aging the film in air and a corresponding change in the I-V characteristics under illumination.

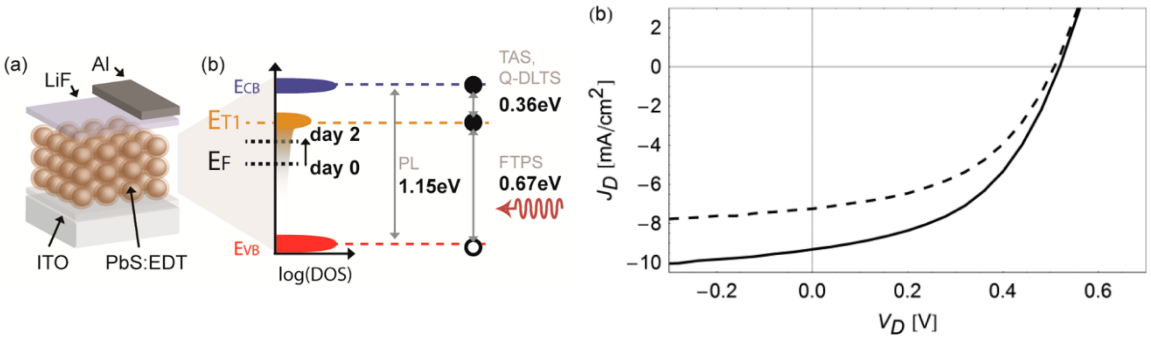

Figure 2.11: Trap response in PbS NC solar cell. a) Device design and energy diagram showing the model of a mid-gap trap state distribution, with a measured increase in the Fermi level after 2 days in air. b) I-V characteristics under AM1.5G illumination before (solid) and after (dashed) aging in air for 2 days. The reduction in current after aging is consistent with an increase in the Fermi level. Figure extracted from Bozyigit *et al.*[93]

Nagpal and Klimov used a field-effect transistor (FET) architecture combined with photoexcitation (they refer to this as an optical FET or OFET) to explore the role of mid-gap states in 3.3 nm PbS NCs with oleylamine ligands.[97] Their work supports a model of a distribution of weakly-coupled mid-gap states associated with the surface ligands, which is mostly full in equilibrium but can be partially emptied with application of negative gate bias, enabling conduction through this "mid-gap band" or MGB. Upon

illumination with light of high enough energy to excite electrons from the valence band into these MGB states, increased conductivity through the more conductive valence band states is observed. They also make note of reports indicating relatively easy change of conductivity from n-type to p-type with small thermal or chemical treatments, indicating that a MGB model might help to explain this behavior given that the Fermi level only needs to move a small amount to change the band from mostly full to mostly empty.[4,46,83,98,99] Figure 2.12 shows their model and conductance data, including the photoconductance spectra as a function of gate bias in Figure 2.12c, showing the appearance of the $1S_h$ (valence band 1S level) to MGB transition at 0.9 eV, well below the band to band transition at 1.3 eV.

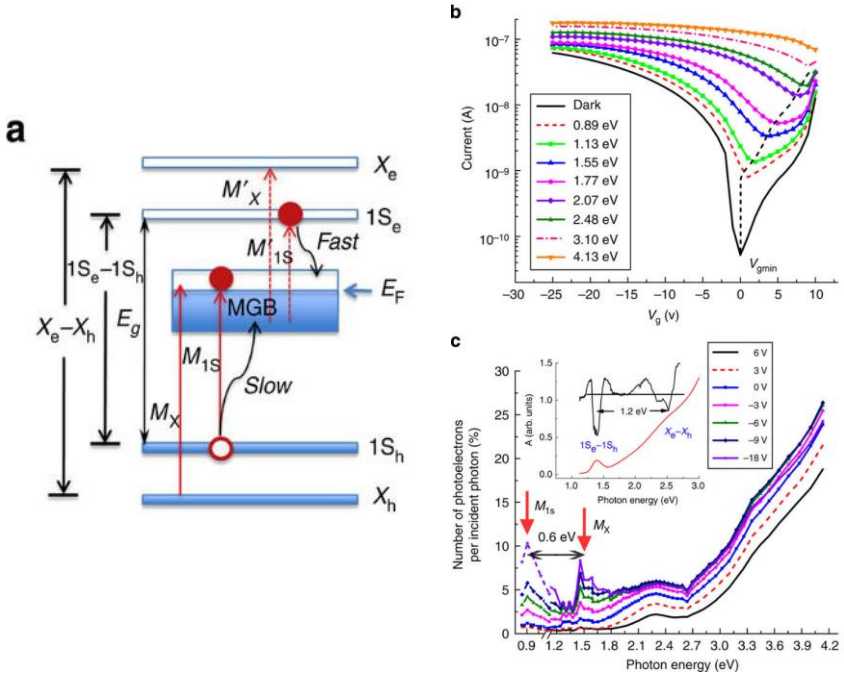

Figure 2.12: Mid-gap states in PbS NC FET. a) Model for mid-gap band density of states in PbS NCs. b) I_{SD} vs V_g as a function of incident photon energy. c) Photocurrent as a function of photon energy and gate bias, showing the transitions to the MGB (M_{1S} and M_X). Figure extracted from Nagpal and Klimov.[97]

It is noteworthy that in this discussion of trap states we have essentially neglected the formalism for hopping transport discussed in the previous section. The reason for this is that these two models for transport have not been well integrated in the broader research community. Most work focuses on one approach or the other, and in fact the general expectation is that the onset of hopping transport would

dominate over the presence of trap states, or even be mediated through those trap states themselves. It is important to keep both models in mind when carrying out transport measurements on NC films, as assumptions involved with either can lead to different interpretations of the same data.

2.5 Conclusion

It should now be clear that electronic transport in NC films, while still governed by the same physics at work in models of standard semiconductor transport, is greatly complicated by the strong confinement potentials and barriers between individual NCs. In NCs of small enough diameter, this leads to quantized energy levels with high densities of states in small energy ranges dictated by the size and variability of the NC ensemble. In addition, large disorder in NC size, chemical composition, and spatial position through the NC film lead directly to the dominance of hopping transport across a wide range of temperatures. These transport processes involve a temperature-dependent optimization of thermal activation and long-range tunneling, from which different regimes of hopping can be identified. At high temperatures, thermal activation is rapid, leading to hopping conduction that takes place only across the shortest available distances. This is referred to as nearest neighbor hopping and is indicated by a log-linear relationship between resistance and inverse temperature. As the thermal energy decreases, longer-range tunneling is favored, so the film enters the Mott variable range hopping regime. Finally, at significantly low temperatures, the coulomb interaction between charge carriers becomes significant, and the soft gap in the density of states associated with this interaction begins to dominate transport. This regime is known as Efros-Shklovskii variable range hopping. In addition to these disorder-related phenomena, defect states can be just as significant as they are in bulk semiconductor transport by localizing charge carriers in mid-gap trap states. In NC films, where the crystalline core can be of exceptionally high purity, these defects are often located at or near the NC surfaces. As a result, their influence on conduction is magnified by the resultant decrease in electronic coupling across these surfaces.

3 Electronic Measurement Techniques for Semiconductor Nanocrystals

3.1 Introduction

Using the theory and models detailed in Chapter 2, we can now discuss some of the measurement techniques used for NC thin films. These can be broadly separated into two categories: time-independent (dc) techniques and time-dependent (spectroscopic) techniques. The dc techniques are all based on conceptually straightforward I-V measurements, either in thermodynamic equilibrium (Section 3.2) or with electrostatic or electrochemical control used to tune the concentration of charge carriers in the film and observe a wider range of transport properties. The later involves the use of devices such as field-effect transistors (Section 3.3) or electrochemical cells (Section 3.4) to induce high electric fields in the NC films and modulate the density of charge.

Two spectroscopic techniques developed for the analysis of bulk semiconductors are discussed. The first is a large-signal transient technique known as deep level transient spectroscopy (DLTS), which uses transient voltage pulses to produce large changes in NC charge levels and time-resolved measurement of the charge redistribution to obtain information about trap states and thermally activated conduction mechanisms (Section 3.5). The second is a small-signal harmonic technique known as thermal admittance spectroscopy (TAS), in which resonances in the complex admittance are measured in response to a small modulation of charge in the film. These resonant features can be measured as a function of temperature to extract transport properties, including trap state energies and densities (Section 3.6). In general, both of these spectroscopic techniques have the advantage of separating distinct rate transport processes to different spectral locations, and thus have inherently more information than the dc techniques. However, properly interpreting the frequency response of NC films is not always straightforward and can be complicated by the large energy barriers and weak coupling between NCs.

3.2 Temperature-Dependent Conductance

Conductance measurements are typically the first method for electrical characterization of any material or device due to the simplicity of device design, measurement process, and data analysis. This is also true for NC films, for which simple two-point I-V measurements have proven an invaluable tool for investigating a wide range of materials. While the basic physics does not necessarily change, these films usually behave quite differently due to their discrete granular nature and relatively large degree of disorder, along with the extreme influence of surfaces, which can more easily be neglected in bulk materials. As a result, the dominant physical and chemical features for conduction and the appropriate experimental tools for measuring and characterizing these factors are still being developed.

While direct comparisons of room temperature conductivity between samples can give insight into the underlying transport phenomena, the knowledge gained is limited, as in any material system, due to the large number of factors that contribute to this single value. If, as in a standard Schottky junction, there is a barrier that is discrete in both energy and space, field-dependent measurements that yield non-linear conductance can be used as in standard analysis to extract the barrier height. However, due to the extreme disorder and high density of states in NC materials, this does not always occur as one would expect, as the Fermi level at NC/metal junctions can be strongly pinned and barriers to conduction can be dominated by mechanisms that are not relevant in standard semiconductor analysis.

In two separate papers,[65,100] Chen *et al.* used temperature-dependent conductance measurements of intrinsic colloidal Si NCs passivated with surface ligands and ligand-free Si NCs doped with P in the gas phase before direct film deposition. As would be expected, intrinsic NCs with surface ligands were highly resistive, with $\rho > 10^8\ \Omega\ cm$ at room temperature. As a result, a vertical geometry was used to get reasonable current levels, with a device area in the range of 1-5 mm^2 and film thicknesses on the order of 100 nm. The potential concern with a device structure of this nature is that contacts can dominate the measured conductance. However, for low-conductivity films, this should not be a concern and can usually be neglected, as they did. Figure 3.1 shows the results for films before and after aging in air, with an

increase in conductivity due to aging of almost 10^3. In all measurements, they observe thermally activated charge transport that they associate with NNH (see Section 2.3) with an activation energy related to the NC charging energy (Equation 2.4).Figure 3.1: Temperature-dependent conductance for intrinsic Si NCs.

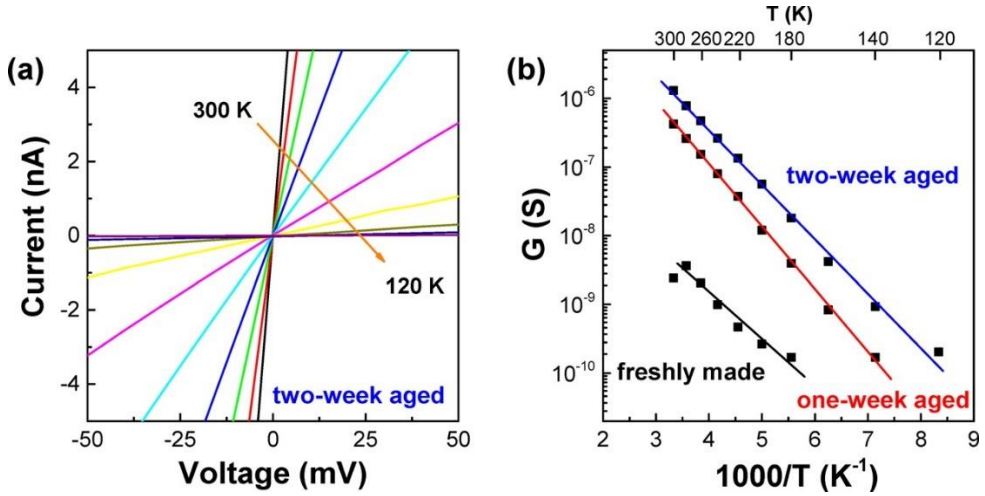

Figure 3.1: Temperature-dependent conductance for intrinsic Si NCs. Figure extracted from Chen *et al.*[65]

They also saw non-linear conduction at high electric fields, shown in Figure 3.2. The temperature dependence of the high field conductance decreased with field strength, eventually reaching approximately temperature-independent conduction at the highest measured field. They associate this with a lowering of the barrier for ionization from a NC to its nearest neighbor due to the Poole-Frenkel effect[101,102] rather than diode behavior due to a Schottky junction. In addition, they use the field dependence at low temperature to describe the long-range field-assisted tunneling process by which conductance is enhanced at low temperature where thermal energy is insufficient to overcome barriers in the film. This tunneling distance can be given as $x \sim 2E_c/eF$,[103] with a corresponding conductivity of $G \propto \exp\left(-\frac{x}{\xi}\right)$. From this and the charging energy measured at high temperatures, they are able to extract the localization length ξ as 1.1 nm.

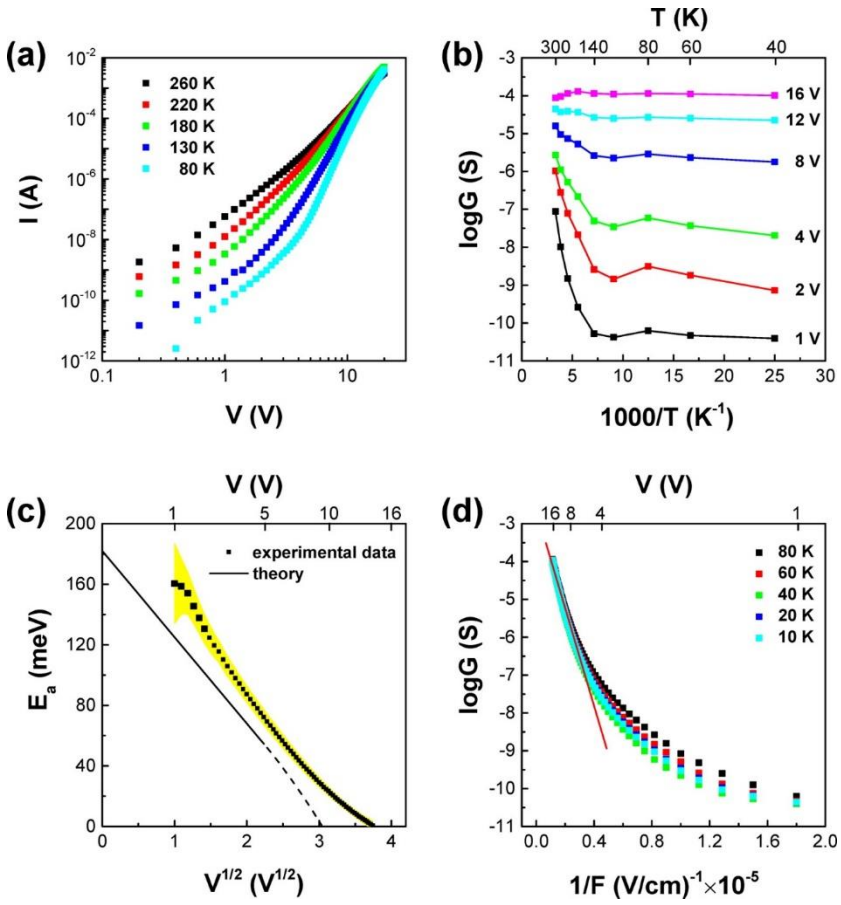

Figure 3.2: Field-dependent conductance for films of intrinsic Si NCs. Extracted from Chen *et al.*[65]

With the more highly conductive doped Si NC films, they were able to perform a similar analysis. However, in these films, they observed E-S VRH (i.e. $lnG \propto T^{1/2}$) with the slope of the exponential temperature dependence decreasing with increasing doping levels. Using the relationship for the slope of $T_{ES} = \frac{Ce^2}{4\pi\varepsilon_0\varepsilon_{eff}k_B\xi}$, they could again extract the localization length, shown in Figure 3.3. From this, they demonstrated that the increase in doping level resulted in an increase in the localization length, which they associated with an approaching transition from insulating behavior to metallic behavior, in which carriers are completely delocalized ($\xi \rightarrow \infty$). This is a good example of the kind of analysis that can be done with simple two-point I-V measurements to gain further insight into the processes underlying charge transport in these films.

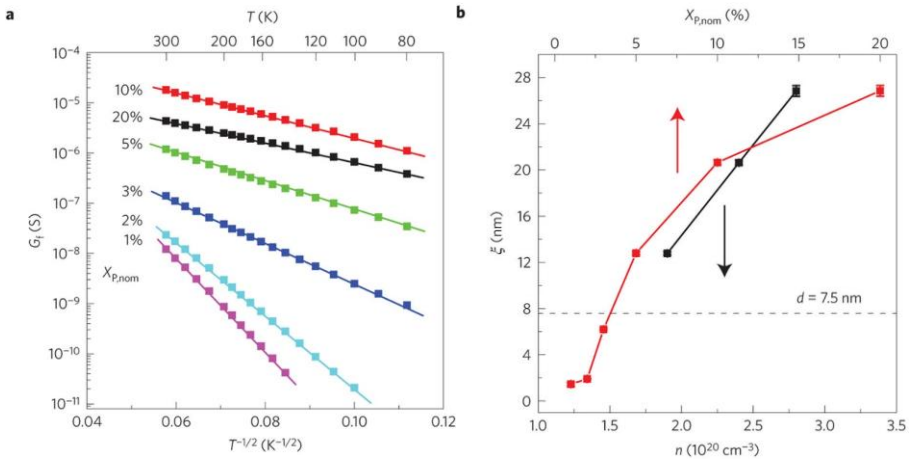

Figure 3.3: Temperature-dependent conductance for films of doped Si NCs. Extracted from Chen *et al.*[100]

Romero and Drndic[85] reported similar findings for films of undoped PbSe NCs. The results are shown in Figure 3.4, where they reported two regimes of thermally activated transport at high temperatures (>200 K) and a transition to E-S VRH at lower temperatures. Such a transition is expected, as discussed in Section 2.3, and being able to characterize this process in NC films provides crucial insight into the mechanisms that dominate the electronic transport. Similar to the work of Chen *et al.*, they associated the thermally activated transport with a combination of NC charging energy and thermal generation of charge carriers across the bandgap, indicating in this case that the Fermi level was positioned far from the band edges. In the E-S VRH regime, they found a localization length of 3.3 nm.

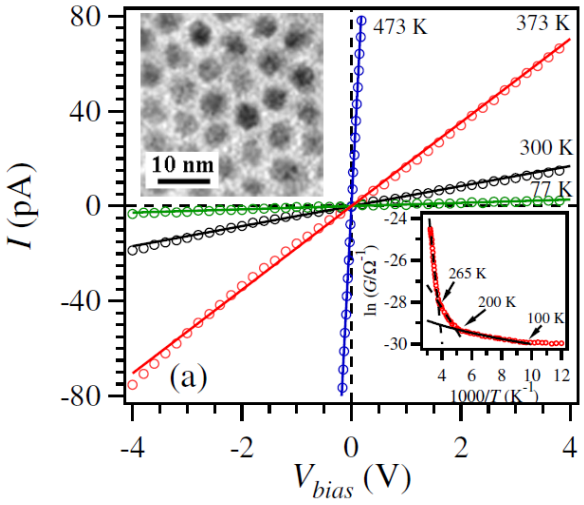

Figure 3.4: Temperature-dependent conductance for undoped PbSe NCs. Extracted from Romero and Drndic.[85]

Making comparisons between different reports is problematic due to the vast differences in NC films, but for the sake of demonstration, we can attempt to learn about the differences in these materials through these measurements. The PbSe NC film shows a three-fold increase in localization length relative to intrinsic Si NCs, but has a room temperature conductivity five orders of magnitude lower. This may be indicative of this PbSe film having a much lower intrinsic carrier concentration and higher energy barriers for transport while simultaneously having material parameters that increase the localization length. This type of analysis allows us to characterize different materials or processing steps in ways that can be used to guide further NC material and device development.

3.3 Field-Effect Transistor

Using the device structure of field-effect transistor (FET) is an excellent method to expand the range of measurements available and gain further insight into charge conduction physics in NC films. In its simplest form, experiments with such a device allow conductance measurements to be performed on a single film with a range of carrier concentrations by controlling the bias applied to an insulated electrode. This applied bias creates a strong electric field near the surface of the NC film, drawing in excess carriers (holes or electrons) depending on the strength of the bias. Generally, this device consists of a metal electrode (gate) isolated from the semiconductor film by an insulating film (gate dielectric) in what is

referred to as a metal-oxide-semiconductor FET, or MOSFET. The operation of this device is described by the capacitance as $C' = dQ'/dV$ where C' is capacitance per unit area, Q' is the charge density per unit area, and V is the voltage across the capacitor. Under bias conditions such that the entire differential gate bias is dropped across the oxide, the capacitance becomes independent of bias and $\Delta Q' = C'\Delta V$ describes the density of charge added to the surface of the NC film in the active area of the device, referred to as the channel.

Most measurements for NC films are performed in a bias regime such that the lateral field between the conducting contacts, referred to as the source and drain contacts, can be neglected. In this case, the FET shows ohmic behavior with a resistance that can be modulated by the gate bias and

$$I_d = \mu C'_{ox} \frac{W}{L}\left[(V_g - V_{th})V_d - \frac{V_d^2}{2}\right] = \mu Q' \frac{W}{L} V_d \tag{3.1}$$

where I_D is the drain current, μ is the mobility, W and L are the channel width and length, respectively, V_g and V_d are the gate and drain biases, respectively, and V_{th} is the threshold voltage, which is defined as the gate bias for which $I_d = 0$. At high enough lateral field strengths, the vertical potential near the end of the channel approaches zero, pinching off the conductive channel. This operating regime is referred to as saturation, where the drain current becomes independent of drain bias as $I_d = \mu C'_{ox} \frac{W}{L}(V_g - V_{th})^2$. For most material characterization experiments, it is preferred to operate in the ohmic regime, avoiding saturation.

Figure 3.5 shows data collected by Turk *et al.* using a MOSFET structure with a CdSe NC film.[43] This experiment tells a similar story to that of Figure 3.3, where E-S VRH conduction at various Si NC doping levels was used to show an increasing electron localization length. In this case, a slightly different temperature dependence is found, with $ln\rho \propto 1/T^{2/3}$, which the authors associate with E-S VRH along with thermal broadening effects.[104] From this model, they are able to extract the localization length, showing similar increasing behavior with carrier concentration to the data in Figure 3.3. In this case, however, the measurements were performed on a single device, rather than requiring the synthesis of films

with a range of doping levels. From a practical device standpoint, the capability for controlled doping is obviously a major synthesis requirement. However, from a characterization perspective, the ability to observe a range of conduction properties with a single device makes FET measurements very useful.

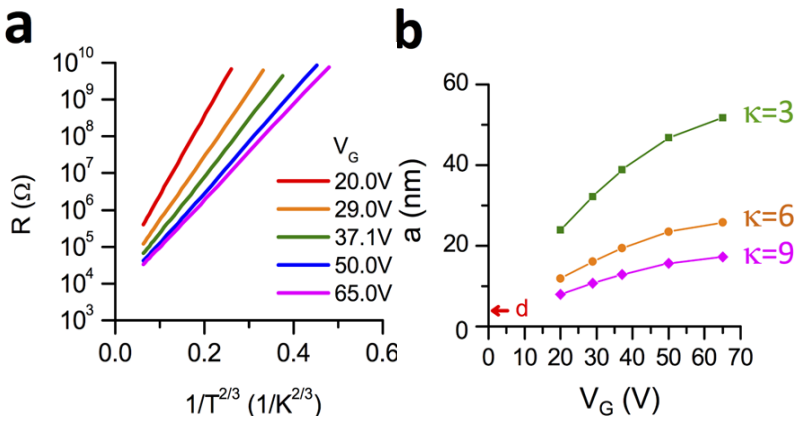

Figure 3.5: CdSe MOSFET measurements as a function of temperature. Gate bias dependence of resistance as a function of temperature. b) Extracted localization length as a function of gate bias. For different assumed values of dielectric constant. Figure extracted from Turk *et al.*[43]

Another example of the advantages of FET devices is shown in Figure 3.6.[42] These measurements used PbS NCs with a double gate design in which the NC film is deposited on a traditional SiO_2 MOSFET substrate followed by subsequent deposition of polymer dielectric on top of the NC film. From this they could compare the conductance as a function of carrier density, shown on the left side of Figure 3.6, for the two gate dielectric materials, showing comparable current levels at much lower charge densities for the top gate with polymer dielectric. They used numerical analysis developed for modeling the drift and diffusion currents in organic thin film transistors with a mid-gap density of states[105] to extract the interface trap densities for the two dielectrics, shown on the right side of Figure 3.6. They observed a dramatic reduction in trap concentration using the polymer dielectric, which explains the higher conduction at low carrier densities. In this way, NC FET characterization can inform device design decisions for NC films.

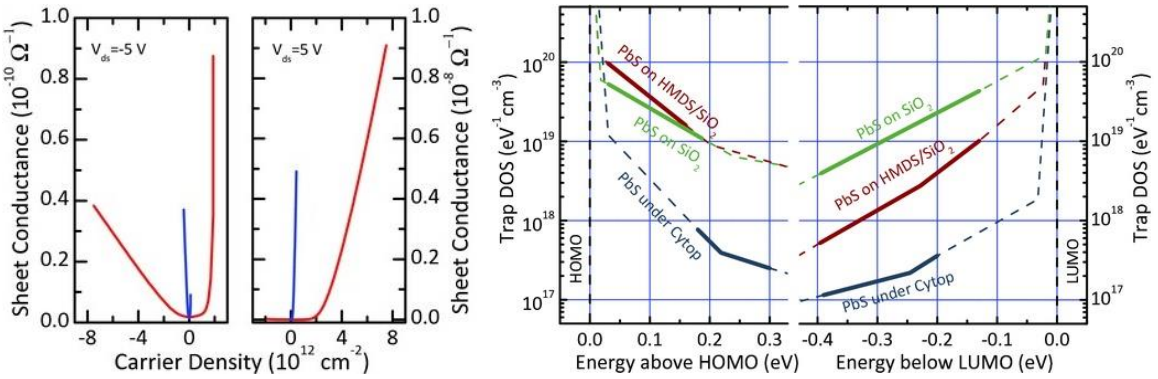

Figure 3.6: PbS FET measurements with SiO_2 bottom gate and polymer top gate. Left: Channel conductance as a function of gated carrier density for SiO_2 (blue) vs polymer (red). Right: Trap density of states vs energy calculated from models of semiconductor charge transport with a mid-gap DOS. Figure extracted from Nugraha *et al.*[42]

Finally, two studies from Kang *et al.* using PbSe NCs show further use of the FET device for characterization of fundamental NC conduction physics. In one study, they used a heavily doped Si wafer as the gate material and substrate with a thermal oxide as a gate insulator, with a PbSe NC film deposited from solution as the active layer to form a MOSFET.[81] They observed ambipolar behavior, as shown in Figure 3.7a with a temperature dependent mobility resulting in decreasing current levels down to 28 K. They were interested in investigating the transport properties as a function of NC size, so their studies did not take advantage of the ability to vary the gate bias. However, by having this ability, they were able to use NC films that were otherwise poorly conductive, as indicated by the off current in Figure 3.7a, and gate them to a more conductive state by applying a gate bias of V_g-V_{th}=50 V, giving a sheet charge concentration of 4×10^{12} cm^{-2}, avoiding the necessity of altering the NC synthesis and deposition processes to fabricate conductive films. Under these bias conditions, they observe a size-dependent transition from ES-VRH to NNH as a function of temperature, as shown in Figure 3.7b-d. Such a study could be extended to include similar measurements at various gate biases and develop a more detailed picture, including the differences between hole and electron transport due to the ambipolar behavior.

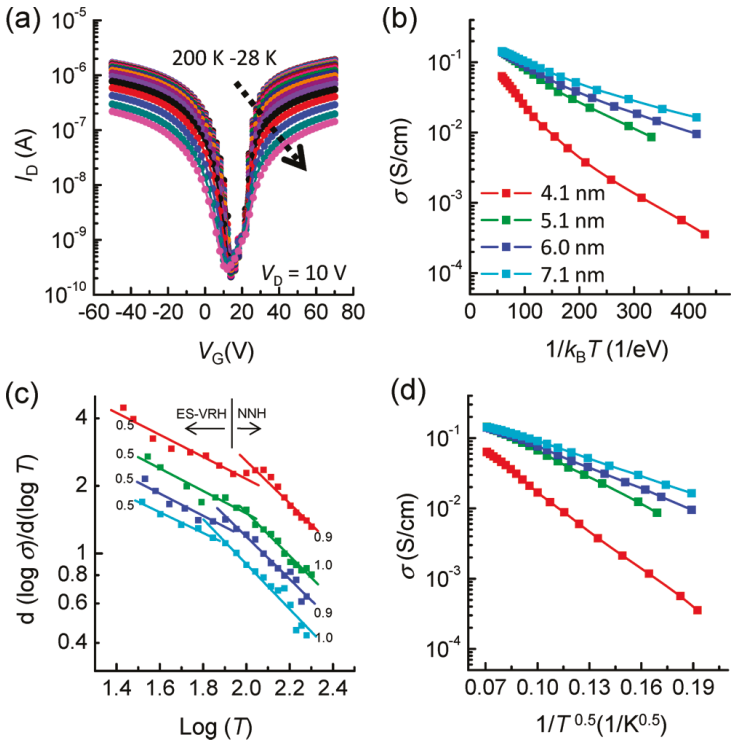

Figure 3.7: PbSe MOSFET measurements for hopping conduction. a) Current vs gate bias as a function of temperature. b-d) Hopping conduction measurements at electron injection levels corresponding to ~4×10^{12} cm^{-2}, showing a NC size-dependent temperature transition from NNH to ES-VRH. Figure extracted from Kang *et al.*[81]

The other study from Kang *et al.*[98] shows a different method for fabricating a FET device that is particularly well suited for many NC film applications. Here, they use an ion gel gate dielectric in which mobile ions form a high-capacitance nanometer-sized double layer in response to an applied electric field, which is capable of inducing high charge densities >10^{14} cm^{-2}.[106] This is fundamentally quite similar to electrochemical gating (see Section 3.4, below) but maintains the solid state device structure that is often desirable for measurements, particularly for vacuum and cryostat systems. These high charge densities are also useful for NC materials that may be highly resistive due to large surface state densities, as these may prevent significant Fermi level modulation with standard MOSFET devices due to capacitance and breakdown field limitations.

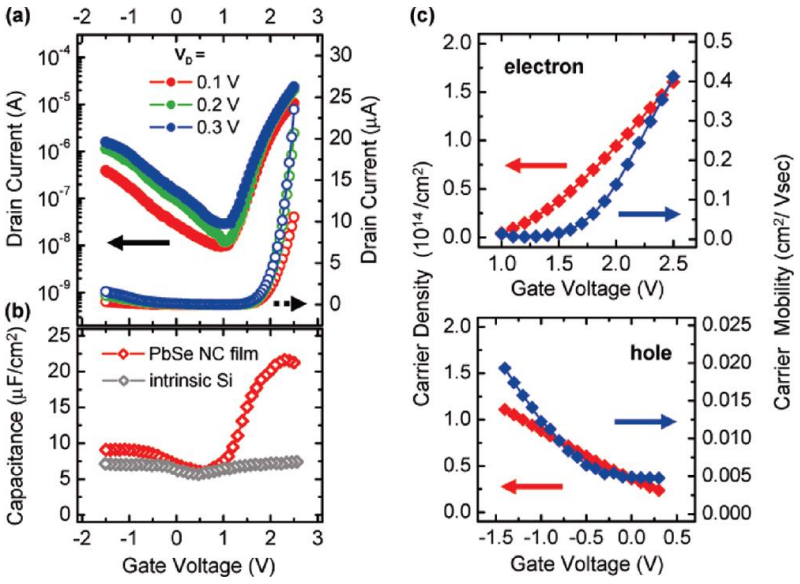

Figure 3.8: PbSe ion gel FET characteristics. Drain current vs gate voltage showing ambipolar behavior. b) C-V data used to calculate surface charge density for mobility measurements. c) Electron and d) hole carrier densities and calculated mobilities as a function of gate bias. Figured extracted from Kang *et al.*[98]

Figure 3.8 shows the results from this work on PbSe ion gel FETs. In this case, temperature-dependent measurements were not performed, although there is no reason such a measurement could not be made with this structure to obtain the kinds of information discussed above. However, these results do show the potential of these structures for characterizing NC films over a wide range of carrier densities. Figure 3.8b shows the measured C-V characteristics for the PbSe FET (red) and a test device on an intrinsic Si wafer (gray). This demonstrates an interesting feature of these devices that can be problematic, but also useful if properly understood. The capacitance values for hole accumulation (negative gate bias) for the NC and Si test devices are similar at 9 μF/cm^2 and 7 μF/cm^2, respectively, demonstrating the large capacitance possible with ion gel gating. However, electron accumulation tells a very different story, with the NC FET capacitance exceeding that of the Si test device by a factor of 3.

The authors offer several potential explanations, but the most plausible explanation for the increase in capacitance for NC devices compared to Si test devices is that they are in fact not operating in a surface gating regime but are instead operating in an electrochemical (bulk) regime. By applying large electric fields, the mobile ions within the gel can diffuse into the porous NC film, thus effectively increasing the

device area and inducing charge throughout the thickness of the film, rather than only at the surface. The diffusion coefficients for the cations ($[EMIM]^+$) and anions ($[TFSI]^-$) are given as 5.0×10^{-7} cm^2/s and 3.1×10^{-7} cm^2/s, respectively, explaining the difference between electron and hole accumulation. As mentioned before, this effect can be problematic if not properly accounted for because it appears that more charge carriers are induced per NC than is actually the case. However, if the effect is properly understood and analyzed, this effect allows for charge gating throughout the entire film, which can prove very useful since the limitations of surface conduction, such as surface roughness and 2D geometry, are no longer a problem. These capacitance measurements are used to calculate the carrier concentration as $N' = \int C' \, dV_g / e$, which is shown in red for electrons and holes in Figure 3.8c-d, along with the corresponding mobilities calculated as $\mu = \frac{L}{W} \frac{I_d}{eN'V_d}$. The change in mobility with carrier concentration can be used to learn more about the density of states, trap concentration, and conduction mechanisms.

3.4 Electrochemical Gating

Continuing from this discussion, it is worth briefly addressing the pure electrochemical gating measurements that can be performed on NC films.[107–112] In such measurements the NC film and substrate are immersed in an electrolyte solution with a reference electrode and counter electrode that set the potential of the solution. Due to the porous nature of the NC films, ions in the electrolyte can readily diffuse into the film, inducing changes in carrier concentration uniformly throughout the film thickness. As in the ion gel gated FETs discussed above, these measurements have the capability of inducing very large charge densities, such that the NC conduction can be varied over a wide range and the influence of large trap densities can be overcome.

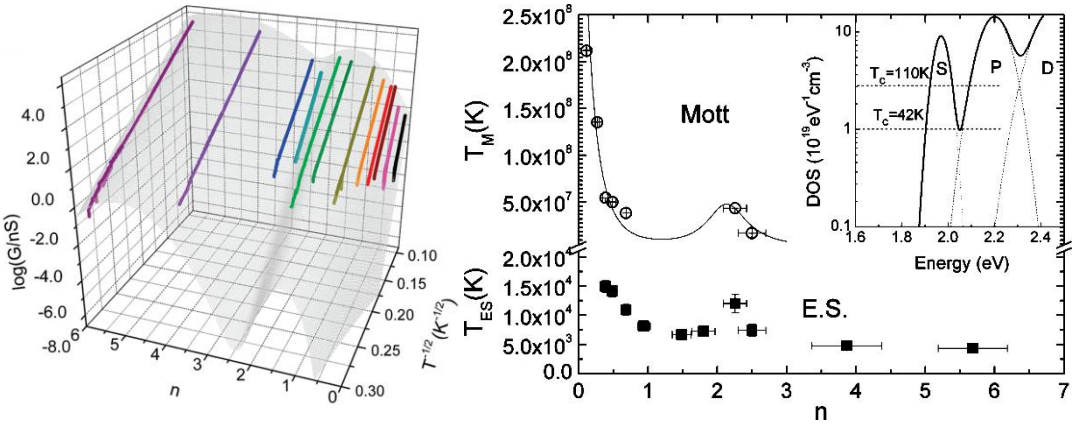

Figure 3.9: Variable range hopping conduction in CdSe NCs observed with electrochemical gating. Left: Conductance as a function of temperature and average carrier density per NC. Right: Mott and E-S VRH slopes as a function of carrier density, correlated to the NC quantized orbital density of states. Figure extracted from Liu *et al.*[107]

Liu *et al.* used electrolyte gating in a cryostat measurement system to demonstrate changes in hopping conduction as a function of carrier density in CdSe NC films.[107] The left side of Figure 3.9 shows temperature-dependent conductance as a function of carrier concentration, shown as average number of electrons per NC. The gray overlay maps the trend to visualize the peaks and valleys associated with the filling of NC orbitals. The conduction band of CdSe does not have any degeneracy, so the 1S and 1P levels can accommodate 2 and 6 electrons, respectively, which can be seen in the conductance measurements where a local maximum is observed at n=1, corresponding to a half full 1S level, followed by a local minimum at n=2 when the 1S level is filled. The density of states, shown in the inset on the right side of Figure 3.9, has a minimum at this point, leading to the low conductance. The measured conductance peaks again near n=5 with the 1P level half full, with larger conductance measured in the higher DOS 1P level compared to the 1S level.

For temperature-dependent measurements, they set the charging level while cooling the sample and electrolyte through the electrolyte's freezing point before disconnecting the electrolyte electrodes and locking in the charge concentration. By measuring conductance as a function of temperature below this point, they were able to observe a transition from Mott VRH to E-S VRH. The temperature of this transition is proportional to $g_0\xi^2$ with g_0 the Fermi level DOS and ξ the electron localization length.

They used the E-S VRH relations (Section 2.3) to calculate ξ based on the dielectric constant of the NC film and the Mott VRH regime to subsequently calculate g_0. An interesting feature of the characteristic temperature reported in the right side of Figure 3.9 is the increase in T_{ES} in the low-DOS regions. As discussed in Section 2.3, this slope is related to the film properties by $T_{ES} = Ce^2/\kappa k_B \xi$, with κ being the dielectric constant and C a constant generally given as 2.8. Liu *et al.* attempt to explain this increase in T_{ES} through changes in the dielectric constant as a function of DOS, but they note that the typical model for this behavior, understood as a change in the oscillator strength between the interband transition and the lower energy intraband (1S-1P) transition, should only account for approximately a 10% change in dielectric constant. However, the change in T_{ES} would require a three-fold decrease in dielectric constant. An alternative explanation is that electrons lying in the low DOS portions of the conduction band are more localized that those in the higher DOS peaks, resulting in a smaller localization length ξ in the valleys. In any case, this work demonstrates the capability of electrochemical gating to modulate the carrier density in NC films over a wide range such that filling of multiple quantized energy levels can be observed along with the corresponding changes in hopping conduction.

Another demonstration of electrochemical gating in NC films is shown in Figure 3.10, showing quantized energy level filling of ZnO NCs. Capacitance data from these measurements is used to calculate the injected charge, as shown in the upper left of Figure 3.10, which is used to calculate mobility values in the right side for two different NC diameters, 3.9 nm and 4.3 nm. The solid lines shown along with the charge measurements represent models calculated from absorbance measurements, showing excellent agreement. The integrated absorbance data is also shown in arbitrary units in the lower left of Figure 3.10 to demonstrate the correlation between absorption and charge density. On the right side, stepwise increases in mobility are observed with filling of the NC energy levels, with the smaller NCs showing sharper transitions between orbitals. The larger NCs also show higher charge densities, reaching the level of the 1D orbital.

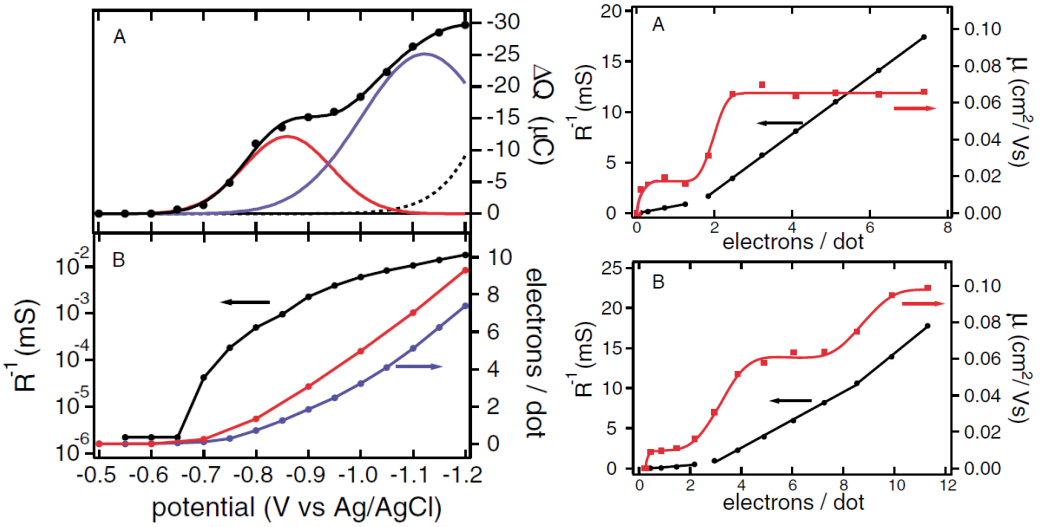

Figure 3.10: ZnO NC electrochemical charge injection and corresponding conductance measurements. Left: a) Injected charge as a function of applied bias. The black line is a sum of the red and blue gaussian distributions. b) Film conductance (black) and average electron density per NC (blue), along with integrated absorbance change (red), as a function of electrochemical bias. Right: Conductance and mobility as a function of carrier density for a) 3.9 and b) 4.3 nm NCs, showing stepwise increase due to energy level filling. Figure extracted from Roest *et al.*[108]

3.5 Deep Level Transient Spectroscopy

Deep level transient spectroscopy (DLTS) is the first of two spectroscopic techniques that will be covered here. The measurement was developed in the 1970s by D. V. Lang for characterizing mid-gap trap states in semiconductors.[113–115] This is a large signal measurement, in which a voltage pulse is applied for a short length of time to fill electronic states before returning the bias to the measurement level. The carriers now occupying nonequilibrium states will emit and redistribute to an equilibrium state with a rate that depends on temperature, the energy barrier for emission, and the strength of the underlying interactions. This process is shown in Figure 3.11a-c.

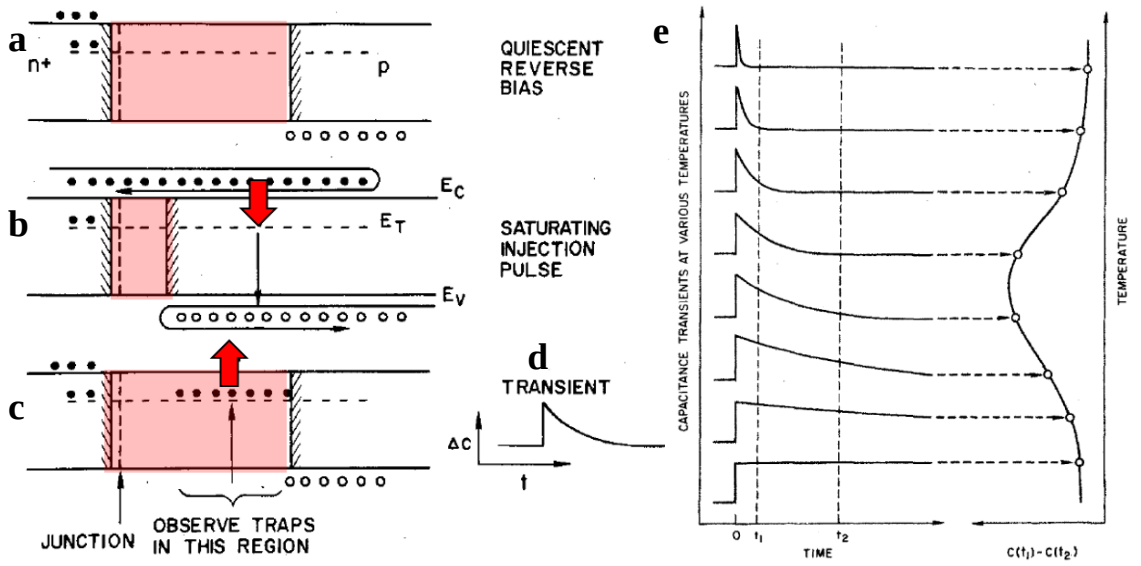

Figure 3.11: Theory of DLTS measurement technique. A one-sided p-n junction is shown. a) A reverse bias chosen for measurement establishes an equilibrium depletion region. b) An injection pulse reduces the width of this depletion region, filling mid-gap states at energy E_T. c) The bias is then returned to the original state, and the non-equilibrium trapped carriers emit to the band with a time constant determined by the temperature, E_T, and interaction strength. The corresponding depletion width relaxes back to its initial value as this trapped charge is removed. d) This is measured as a capacitance transient. e) Ratewindow analysis shows a peak as a function of temperature in the magnitude of the capacitance change $\Delta C(\Delta t = t_2 - t_1)$. The temperature of this peak will depend on the value of Δt, so different values of t_2 and t_1 are chosen during analysis to determine the temperature dependence of the emission process. Figure extracted from Lang.[113]

The standard DLTS measurement is a capacitance transient (Figure 3.11d) measured at a frequency of 1 MHz. This is sufficiently fast that the trapped carriers cannot follow the signal, so the measured capacitance corresponds to the depletion capacitance described by the Mott-Schottky model as

$$C' = \frac{\varepsilon}{W} = \sqrt{\frac{e\varepsilon N_{scr}}{2(V_{bi}-V)}} \tag{3.2}$$

for a diode with built-in voltage V_{bi}, dielectric constant ε, and space charge region of width W containing a total charge density of eN_{scr} at an applied bias V. The same basic technique can be used with current transients, which is referred to as Q-DLTS[116] and has the advantage of not relying on the frequency response of the material being tested, which can be particularly important with NC films where it is not necessarily true that free carriers can respond at high frequencies.[95]

The capacitance changes along with the depletion width in response to trap emission to maintain charge neutrality and keep $N_{scr} = N_D^+ - n_T^-$ (or $N_{scr} = N_D^+ + p_T^+$ for donor traps) constant. Therefore, the capacitance as a function of time can be given as

$$C(t) = C_0\sqrt{1 - \frac{n_T(t)}{N_D}} = C_0\sqrt{1 - \frac{N_T}{N_D}\exp\left(-\frac{t}{\tau_e}\right)} \tag{3.3}$$

where N_T is the total trap concentration, N_D is the donor concentration (all of this analysis assumes an n-type semiconductor, although it is equally valid for p-type materials), and τ_e is the trap emission time constant. This time constant can be related to trap characteristics as

$$\frac{1}{\tau_e} = e_n = \nu_0 \exp\left(-\frac{E_T}{k_B T}\right) \tag{3.4}$$

with E_T being the energy difference between the trap and the band edge and the prefactor ν_0 being the attempt frequency characterizing the strength of the interaction between the trap and the band.

In order to analyze the capacitance transients, ratewindow analysis is used, as shown in Figure 3.11e. In this analysis, the magnitude of the capacitance change $\Delta C = C(t_2) - C(t_1)$ is calculated at a range of chosen values for t_2 and t_1. These times set a measurement time constant as $\tau_e = (t_2 - t_1)/\ln(t_2/t_1)$, which can then be related to the trap parameters through Equation 3.4, with the temperature determined as the position of the peak in $\Delta C(T)$. By varying the chosen time constant τ_e, the position of the peak in $\Delta C(T)$ shifts to different temperatures. One of the main advantages of DLTS is that the sign of the capacitance transient can be directly related to the polarity of the charge being trapped, making the distinction between majority and minority traps trivial.

DLTS has not yet been extensively applied to NC films, due to some of the difficulties in interpreting the frequency response of these materials. Indeed, any capacitance measurements can prove difficult to work with in NC films due to the high density of states in the quantized energy levels and potentially large mid-gap state densities associated with the large surface-to-volume ratio of small spheres. As a result, it is not unusual for depletion widths to extend over as little as a few or a single layer of NCs, resulting in

relatively small changes in capacitance that can be difficult to analyze quantitatively and which are easily interfered with by parasitic capacitances and series resistance in the system. In addition, the large barriers to conduction created due to disorder and weak electronic coupling throughout the film, as discussed in Section 2.3, make interpreting the results within the standard framework of semiconductor analysis difficult or impossible.

Despite these challenges, some valuable work has been reported. Bozyigit *et al.* reported on the use of Q-DLTS for the analysis of trap states in colloidal PbS NC solar cells.[95] They used Q-DLTS instead of the traditional capacitance method because of the concerns mentioned above, namely that the depletion capacitance does not respond at high frequencies. As a result, they showed the capacitance is bias independent at these frequencies, so the DLTS capacitance transients would not indicate show any response, either. However, using dc current transients, they are able to measure the total charge emitted as a function of time and temperature and perform the same basic analysis. The results and models for this work are shown in Figure 3.12. They reported two separate response signals, which they label T1, corresponding to the slower, higher temperature response, and X, corresponding to the weakly temperature-dependent response observed at lower temperatures. By supporting the DLTS data with photoconductance measurements, they model these processes as shown in the right side of Figure 3.12. The T1 signal corresponds to emission from a mid-gap band of states to the conduction band, while the X signal is related to hopping conduction through this mid-gap band. Unfortunately, they do not attempt to analyze this mid-gap hopping conduction further, but similar conduction methods have been proposed for NC films elsewhere.[97]

In some NC systems, the lack of free carrier response at high frequencies could be taken as evidence of hopping conduction freeze-out, whereby the large barriers and weak coupling prevent free carriers from tunneling between NCs over short times. However, an inherent advantage in this regard of a material like PbS is its high dielectric constant. As a result, even a fairly porous film, should be expected to have charging energies (see Equation 2.4) on the order of <10 meV, indicating that this can be neglected at

most temperatures and certainly cannot account for the 400 meV activation energy that they reported. Because of this, their analysis probably is correct, with the understanding that there are very few free carriers present in the NC film, leading to full depletion and bias-independent capacitance at high frequencies. Conduction only proceeds via emission from the mid-gap states or more weakly via hopping within the mid-gap states.

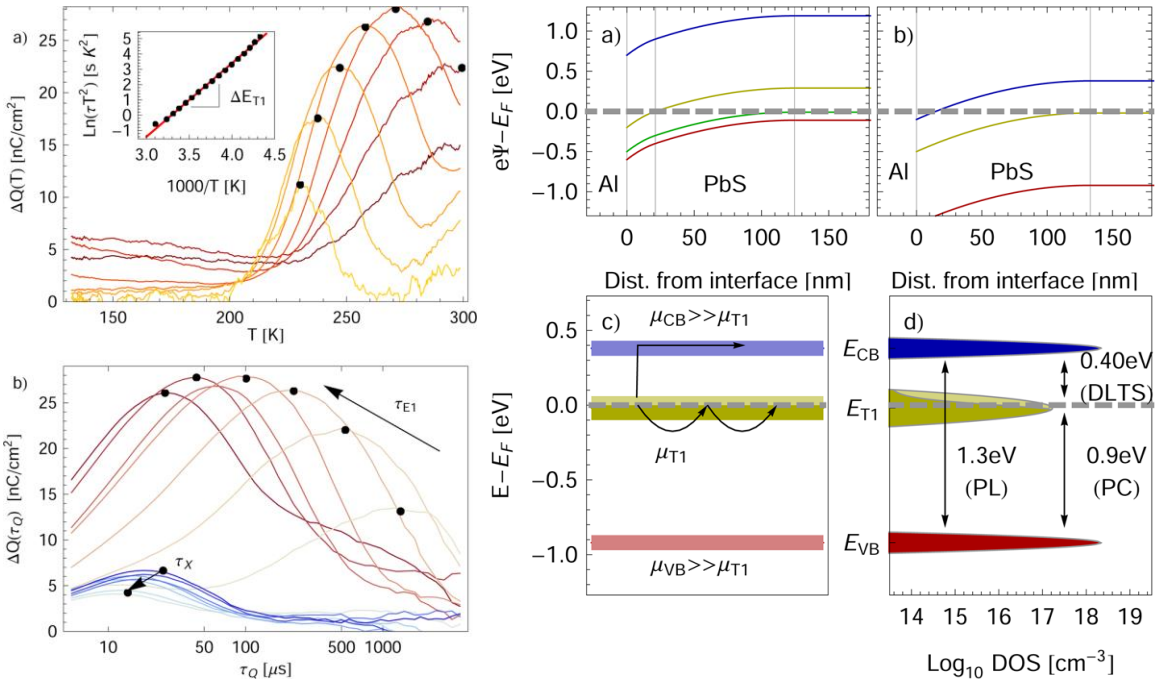

Figure 3.12: DLTS results for PbS NC solar cells. Left: a) Total charge emitted as a function of temperature at different measurement time constants with the corresponding Arrhenius plot shown for extracting the trap energy. b) The same data plotted as a function of time constant at different temperatures, showing the different rates of time constant decay with temperature for the processes labeled E1 and X. Right: Proposed models for the DLTS results. a) Band diagram for PbS NC Schottky diode assuming normal p-type doping of PbS. b) Alternative model assuming that the trap state forms a distributed mid-gap band in the upper half of the gap. c) Transport in this model showing conduction both in the conduction band states and via hopping through the mid-gap band. d) Density of states and energetic location of band energy levels and T1 mid-gap states. Figure extracted from Bozyigit *et al.*[95]

There is another device structure that has been used more extensively for DLTS NC characterization, although it has been almost exclusively used for NC grown using chemical vapor deposition (CVD), molecular beam epitaxy (MBE), or similar non-freestanding growth methods.[117–125] These devices, most commonly metal-oxide-semiconductor (MOS) capacitors with NCs embedded in the oxide layer to act as charge storage centers in a floating gate device, employ charge tunneling from a semiconductor (typically

Si) substrate into a NC layer. Generally, these devices have been fabricated for memory applications, where the long-lived charge storage in the NCs is utilized for its own purposes, rather than as a characterization tool for understanding NC energy states explicitly. However, there is no reason that this must be the case. In such a device, the depletion capacitance of the bulk semiconductor substrate is used as a transducer for the charge stored in the NCs. In this way, so long as the NCs can be assumed to be localized to a thin layer at the semiconductor surface, these states act effectively as interface states at the semiconductor/oxide interface, which have been studied extensively.[126–136] The charging or discharging of these states alters the electric field in the bulk semiconductor, with a corresponding increase or decrease in the depletion width.

Figure 3.13 shows the band diagram model for a measurement scheme from Antonova *et al.*[124] using DLTS techniques to analyze charge states in Ge NC embedded in dielectric films of either SiO_2 or Al_2O_3 by sputtering and subsequent annealing of nonstoichiometric films with varied percentages of amorphous Ge. In this study, they observed several separate trap signals, which they associated with quantized energy levels in the Ge NC as well as defect levels due to low-quality surfaces formed during NC growth during the annealing.

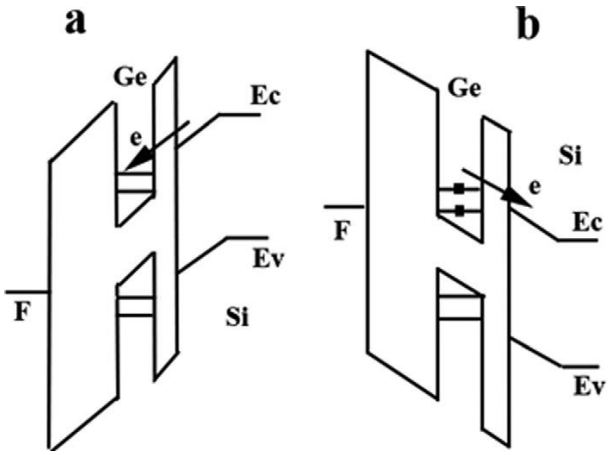

Figure 3.13: Band diagram for DLTS using MOS device with embedded Ge NCs. Figure extracted from Antonova *et al.*[124]

Another example of this type of DLTS measurement is shown in Figure 3.14, which used Si NCs grown in a qualitatively similar way to the Ge NCs discussed above, using thermal annealing of nonstoichiometric SiO_2 to precipitate Si NCs. The data shown demonstrates the signal observed in the DLTS measurements using the depletion capacitance in the Si substrate as a measurement of the charge in the Si NCs. They were also able to correlate these emission signals with quantized energy levels in the NCs.

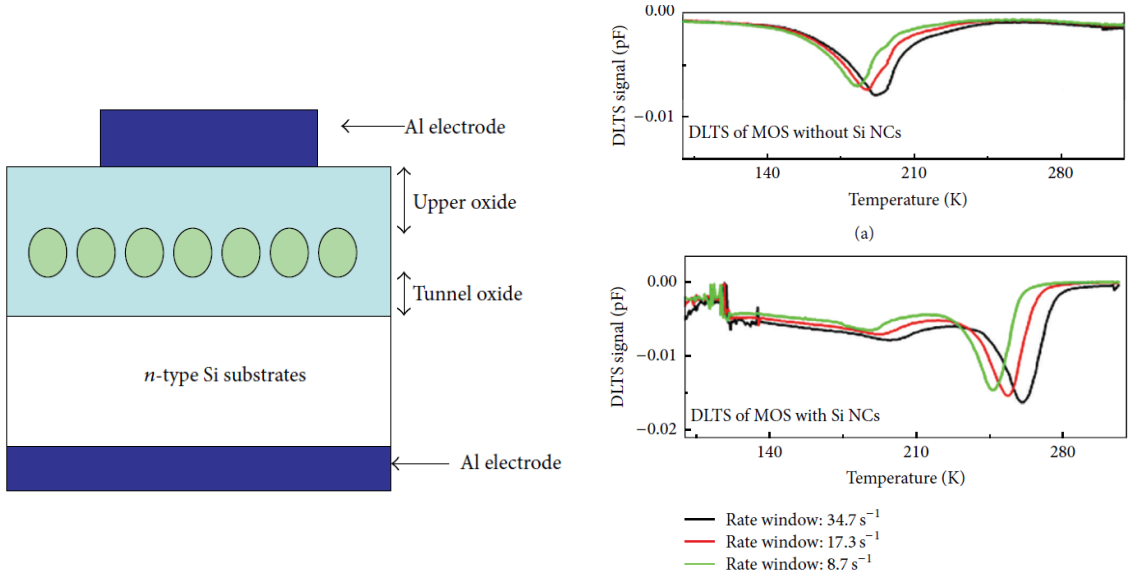

Figure 3.14: MOS DLTS of Si NCs showing schematic device design and examples of DLTS data in devices with and without NCs. Figure extracted from Lv and Zhao.[125]

In general, these types of measurements have not been explored for free-standing NCs. There are certainly difficulties to proper device design and measurement interpretation, such that these measurements should mostly be considered as an advanced technique to include once more basic conduction measurements have been performed. The main difficulties in utilizing this structure for NC measurements center around eliminating or addressing unintended alterations of the emission time, specifically effects related to coupling between the substrate and the NC. If one desires to measure the emission processes taking place within the NCs, then it is desirable for the tunneling rate between the NCs and the substrate to be fast enough as to be neglected. If this is not the case, then it needs to be addressed properly. In addition, interface states associated with substrate surface should be minimized so as not to

interfere with the NC processes. Also, large charge densities can make measure setup and data analysis difficult, particularly if significant hysteresis is observed, so this should be addressed before proceeding further. However, with proper care in passivating the substrate surface and deposition of NC and insulating layers, these techniques should be capable of accurately resolving specific energy levels in the NCs, both the quantized levels and mid-gap defect states. Such a measurement would also have the advantage of being adaptable to a wide range of semiconductor NC material systems, which would allow for rapid characterization of new materials for further device development. It should be noted that the methods and structures discussed here for DLTS can also be used with the TAS measurement (see Section 3.6 below), with particular reference to a technique known as the conductance method.[126,129,128,131]

3.6 Thermal Admittance Spectroscopy

The other spectroscopic technique we will discuss here is known as thermal admittance spectroscopy (TAS). This measurement technique was developed around the same time as DLTS by D. L. Losee.[137] The underlying physics of trap emission rates are the same as those discussed with DLTS, however, the key distinction is that TAS is a small signal harmonic measurement. In this case, a small perturbation of the bias level is applied at frequency $f = \omega/2\pi$ creating an oscillation in the charge distribrution, shown in the left portion Figure 3.15.[138] The complex admittance is measured as $Y(\omega)=Y'(\omega)+iY''(\omega)$, where Y' and Y'' are the real and complex (in phase and out of phase) components. If the device is modeled as capacitance and conductance in parallel, this gives $Y'=G$ and $Y''=\omega C$. A more detailed model would show several capacitance and conductance components in parallel. These parallel impedances correspond to the depletion and trap responses, corresponding to the response of free charge carriers and trapped charge carriers, respectively. The response of trapped charge carriers near the Fermi level will show a resonant step in capacitance at a frequency $\omega_0 = \nu_0 \exp(-E_T/k_B T)$, just as described for DLTS in Equation 3.4. This step in the capacitance corresponds to a peak at ω_0 in the logarithmic slope of the

capacitance $-dC/dln\omega = -\omega dC/d\omega$ and in the dielectric loss function $\varepsilon'' = G/\omega$. This can be seen in the data shown in the right portion of Figure 3.15.

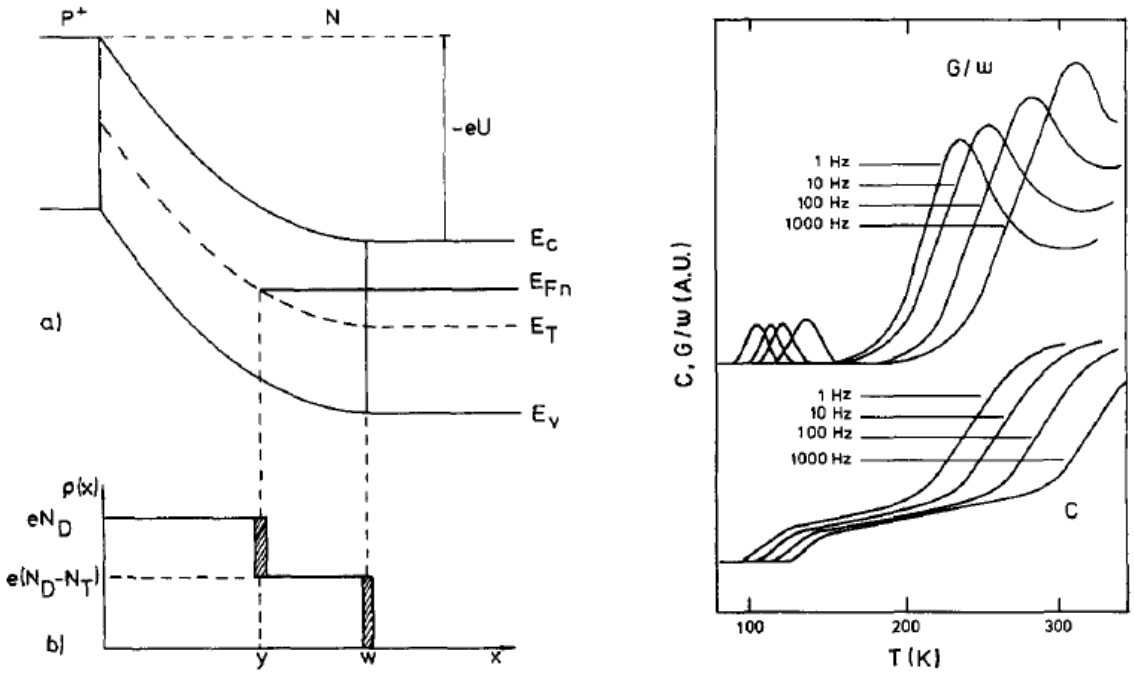

Figure 3.15: Band diagram, charge distribution, and data for TAS. Peaks in G/ω and inflection points in C indicate resonant trap responses. Figure extracted from Barbolla *et al*.[138]

Compared to capacitance DLTS, TAS has the advantage of operating over a range of frequencies, so we don't need to worry specifically about certain assumptions concerning free carrier response at 1 MHz. This, along with simplified measurement setup due to the equilibrium (small signal) nature of the technique and simplified data analysis due to no longer needing to use the ratewindow analysis described above, makes the TAS technique more easily adopted for new materials like NC films.[93,94] However, one must be careful in interpreting the data from this measurement. For example, if a capacitance DLTS measurement does not work because the depletion capacitance does not respond at the 1 MHz measurement frequency, then the high-frequency capacitance will correspond to the geometrical capacitance of the device $C'_{HF} = \varepsilon_{NC}/t_{NC}$ and the resonant step response in the capacitance spectra will be due to the resonant response of free carriers, not trapped carriers. If any trapped carriers can emit charge and respond at higher frequencies than this, then their resonance will not be observed. From a physical

perspective, this can be understood as saying that it doesn't matter if a charge is localized to a surface state or free to move about a NC if it can't subsequently transport away from that NC. This is a situation that would essentially never occur in bulk semiconductors because of delocalized band transport but can be quite possible in NC films due to localization of charge within NCs.

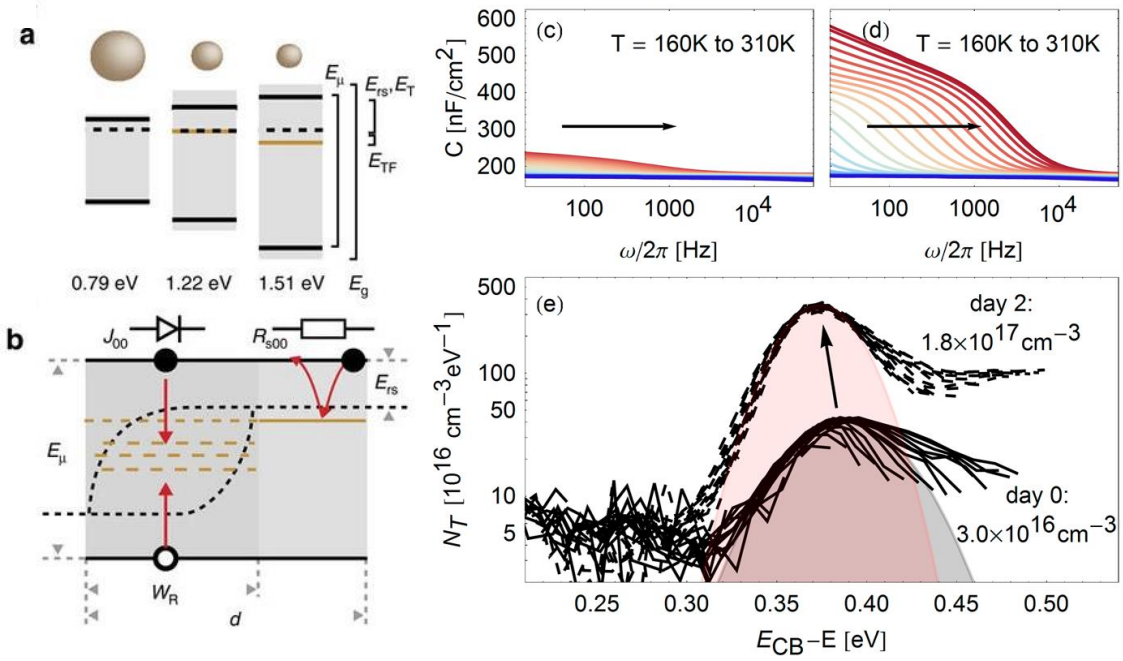

Figure 3.16: TAS measurements and model for PbS NC solar cell. a) Model for NC bandgap and trap position as a function of NC size. b) Model for charge transport in PbS NCs developed from TAS and supporting I-V measurements. Series resistance is attributed to hopping transport while diode behavior is attributed to Schottky contact and deep trap response. c) TAS data for fresh PbS NCs showing weak spectral response. d) Capacitance increases by a factor of 2-3 after aging in air. e) Model for trap density of states based on TAS data. Figure extracted from Bozyigit *et al.*[93] and Bozyigit and Wood.[96]

TAS has so far seen little use in the field of NC device characterization, although a few attempts have been made to utilize this technique.[33,93,94,139–143] A particular detailed and useful example, building off of their work on DLTS referenced above, is the work of Bozyigit *et al.*[93,94,96] shown in Figure 3.16. These results support the DLTS data, where they find a deep state associated with hopping transport. As before, this energy is far too large to be related to a NC charging energy in PbS films, so it is most likely related to a deep trap state. It should be noted that in the model shown in Figure 3.16b, they show a distribution of deep trap states included in the depletion region of the solar cell. In most TAS analysis, it would be

these states that are measured. However, as already discussed, the large hopping series resistance often observed in NC films results in these responses being unobservable as the signal is dominated by the resistance of the undepleted film, labeled R_{s00} in their model. They relate the mechanism of this series resistance to Fermi pinning in the film due to a mid-gap state that increases in density with oxidation. They show that this state is actually a mid-gap band of states, as they suggested in the DLTS work shown in Section 3.5, and they relate the increase in density to a shift in the Fermi level to a higher DOS position within this band upon oxidation.

In this analysis, they develop a fairly complete picture of charge transport in these PbS films, demonstrating the potential value of spectroscopic techniques for NC films. However, it should be noted that they also report large shifts in conductivity in response to relatively small changes in measured trap density, which would be difficult to justify in standard semiconductor models. What this may fail to take into account is the potential for defects localized at or near the NC surface to simultaneously trap free carriers and decrease the coupling between NCs, resulting in conductivity changes that may be orders of magnitude greater than one would expect. It is also important to remember the relatively favorable properties of PbS, namely the high dielectric constant, that allow charge transport to be dominated by mid-gap trap responses more easily. In lower dielectric constant materials, the charging energy can be an order of magnitude higher or more, potentially rendering models like SRH recombination (see Equation 2.11) irrelevant for electronic transport. This, along with other film disorder and NC coupling considerations, mean that one must be cautious in using these techniques developed for bulk semiconductor characterization.

3.7 Conclusion

Due to the combination of high density of states, weak coupling, and large degree of disorder in NC films, along with large uncertainty and variability in making ohmic contact to NC films compared to bulk semiconductors, simple dc measurements have a relative advantage over spectroscopic measurements for these films. In many if not most samples, electronic transport is completely dominated by a single time

constant associated with disorder and coupling (hopping conduction), making the advantages of spectroscopic analysis far less useful. However, in the case of NC films that show strong coupling and a reasonable degree of space charge modulation, where depletion widths of several NC diameters are possible, these frequency-dependent measurements should still prove quite useful in determining the position and concentration of mid-gap defect states. Due to the complexities involved with the device fabrication and data analysis, these should generally be considered as more advanced techniques for further work after detailed analysis of dc measurements has already been completed.

4 Variable Range Hopping Conduction in ZnO Nanocrystal Thin Films

4.1 Introduction

Zinc oxide thin films have been heavily studied as a wide bandgap semiconductor for thin film transistor applications and photovoltaic devices. It can be heavily doped with aluminum and retain a mobility of more than 60 cm^2/V-sec, providing an optically transparent material with a conductivity approaching that of indium tin oxide.[144] A variety of zinc oxide nanostructures have also been reported[145] including nanowires,[146] nanobelts,[147] and nano propellers.[148] The most commonly studied nanostructure of ZnO, however, are nanocrystals (NCs). Available commercially as powders and dispersions, they are used for their antibacterial, anti-corrosive, antifungal and UV filtering properties. The electrical properties of ZnO NC films however are somewhat more difficult to study due to their high surface area.[149] Adsorbed species makes the conductivity of such films differ significantly from that of bulk single-crystals or even amorphous or polycrystalline thin films.[150] Obtaining reproducible results in this type of material can be difficult. Recent work looked at the behavior of heavily doped ZnO NC films, specifically investigating the possibility of transition to metallic behavior.[61] Here we investigate moderately doped ZnO NC films, detailing the effect of infill and surface contamination, as well as thermal and optical treatments to modify the surface.

Lateral dc conduction measurements of ZnO NC films have shown that transport is dominated by hopping,[61] as described in section 2.3. This type of conduction has a stretched exponential temperature dependence $\rho = \rho_0 \exp\left(\frac{T_0}{T}\right)^{\gamma}$, with γ depending on the details of the hopping physics.[104,110,151–153] The most commonly observed values in NC films are

γ=1/2 (Efros-Shklovskii variable range hopping or ES-VRH[78,87,154]), and γ=1/4 (Mott 3D variable range hopping or M-VRH[80]). In general, NC devices transition from Mott to ES once the temperature drops below a critical value[155–158] $T_C = {16T_{ES}^2}/{T_M}$ where T_M and T_{ES}, which are defined in the discussion section, are the Mott and Efros-Shklovskii temperatures, respectively. This crossover has been previously studied in nanocrystal films of CdSe.[107] In both cases, the conductivity coefficient ρ_o depends on the strength of the electron-phonon interaction and the degree of electron localization.[159] Highly conductive films of ZnO NCs, where the carrier density approaches its maximum value, follow ES-VRH over a wide range of temperatures.[61] At sufficiently low carrier concentration, we expect a further transition to nearest-neighbor hopping (NNH), which would follow direct thermal activation $\rho = \rho_0 \exp\left(\frac{E_a}{k_B T}\right)$ with an activation energy associated with the energy difference between a NC with a free carrier and its neighbors. This has been observed in a variety of NC-based materials.[65,81–85]

The room temperature resistivity of ZnO NC films has been shown to decrease by approximately 10^7 with the addition of a passivating Al_2O_3 infill grown via atomic layer deposition (ALD). This was correlated with a decrease in the concentration of surface-bound OH and a corresponding increase in the carrier concentration, as measured by an increasing localized surface plasmon resonance (LSPR) absorption feature.[53] It was later observed that both resistivity and OH concentration could be decreased in both infilled and non-infilled films through exposure to UV light with wavelength less than ~380 nm, with non-infilled films showing rapid reversal in air compared to infilled films, which showed long-lived conductivity increases over months.[61] Similar observations of photochemical

related changes in conductivity have been reported in ZnO previously.[160–169] This presents us with a convenient method for systematically controlling the carrier concentration and corresponding conductivity independent of infill, which can be used to expand our understanding of the hopping conduction in these films.

The formation of surface hydroxyls has been studied for a wide variety of metal oxides in water. It is found that oxide anion and cation exchange sites accept protons from adsorbed water to form acid and base surface hydroxyl groups.[170] The creation of these groups leads to a charge modulation across the surface that ultimately attracts polar molecules such as water through a van der Waals interaction. Indeed, many ALD processes involve the deposition of metal oxides using water vapor and so require such a process. The hydroxyl areal density depends weakly on the metal valence, but is generally saturates at about $2x10^{15}$ cm^{-2}. Thus, a 10 nm diameter spherical particle would accommodate more than 6000 surface hydroxyls.

In this case, the NCs are hydrolyzed by both air exposure and during ALD infilling. Hydrolysis from water vapor occurs for many metal oxides[171] for water vapor pressures greater than ~1 mtorr.[172] In the case of Al_2O_3 ALD, most of hydroxyls created by water vapor exposure are converted to $O\text{-}(CH_3)_2$ bonds by trimethyl aluminum exposure and Al_2O_3 by subsequent hydrolysis. Surface hydroxyls will deplete NC charge since Zn-OH formation will create localized states with an energy well below the bottom of the conduction band of ZnO. If the number of surface-bound OH groups is high enough, this effect will consume all of the as-deposited free carriers, estimated from LPSR to be ~400 per NC[61].

4.2 Experimental Methods

ZnO NCs were deposited using a process that was initially developed for Si NCs and adapted for ZnO and other materials.[54,55] In this method, ZnO NCs were synthesized from the reaction of diethyl zinc and oxygen in an argon plasma and subsequently accelerated via expansion of the argon carrier gas through a slit orifice.[52] The high velocity stream of ZnO NCs can then be deposited by inertial impaction onto a substrate scanned below the orifice in a reciprocating motion. The NC films were deposited at a thickness of ~100 nm.

The ALD infill procedure was performed using a Cambridge Nano Tech, Inc. Savannah series ALD system. Precursor gases were diethylzinc (DEZ) and H_2O. The infill process was modified from standard ALD recipes to allow very long precursor exposures. The precursor pulse lengths were 100 ms and the purge times were 30 s. These processes resulted in infill deposition throughout the NC film, with solid fractions approaching 100% at 70 cycles.[53]

Measurement electrodes consisting of 300 nm Al were thermally evaporated through a shadow mask after any infill or annealing treatments. Lateral test structures were used.

During measurements, samples were mounted to a copper stage with an embedded resistive heater and temperature sensor mounted to cold head and helium refrigerator. All measurements were performed in the dark under vacuum. A viewport in the chamber was used to introduce 365 nm light from a Hg vapor lamp at ~5 mW/cm^2 in measured doses in order to control the carrier concentration. Samples temperatures were kept below 250 K to minimize any backward reaction of residual H_2O within the porous films.

4.3 UV Photochemical Conductance Measurements

The data presented here was collected from ZnO NCs with an average diameter of ~10 nm synthesized using a gas phase plasma technique[54,55] that enables high quality growth of a wide variety of materials without the need for solvents and ligands. This enables greater control of surface chemistry by

removing the constraints inherent to wet chemistry such as the need for stable solutions. Post-deposition treatments, such as thermal annealing, UV annealing, and infilling of the porous structure using ALD have been shown to greatly increase the film conductivity. In particular, the use of ALD-grown Al_2O_3 to infill ZnO NC films has been shown to increase conductivity by almost seven orders of magnitude. This infill process follows the same procedure as a standard Al_2O_3 growth, but with increased pulse and purge times. This allows the precursor gasses to better penetrate the high aspect ratio structures within the film, resulting in a solid fraction approaching 100% for full infill (defined as 70 cycles). It is generally understood that this process stabilizes the NC surface against atmospheric variations and partially passivates surface states, but the details of the underlying mechanisms behind the large improvement in conductivity are still uncertain.

Fourier Transform Infrared Spectroscopy (FTIR) measurements of the LSPR absorption feature in the most highly conductive films show a carrier concentration of $7.6x10^{20}$ cm^{-3} inside the individual NCs that were fabricated identically to those studied here.[61] At a solid density of 35-40%, this equates to ~$3x10^{20}$ cm^{-3} for the entire film. CV measurements indicated that the ZnO NC films were consistently n-type, however, measured carrier concentration, as well as film conductivity, varied widely as a function of post-deposition treatment and measurement conditions such as light exposure, air exposure, and humidity, as well as the sample's history/age. To account for this, films were saturated with H_2O in the ALD chamber at the same temperature as the infill process (180 ˚C) and kept in the dark before loading into the cryostat for measurement. This ensured an as-received state with maximum OH concentration to minimize variability due to environmental factors and sample history/age.

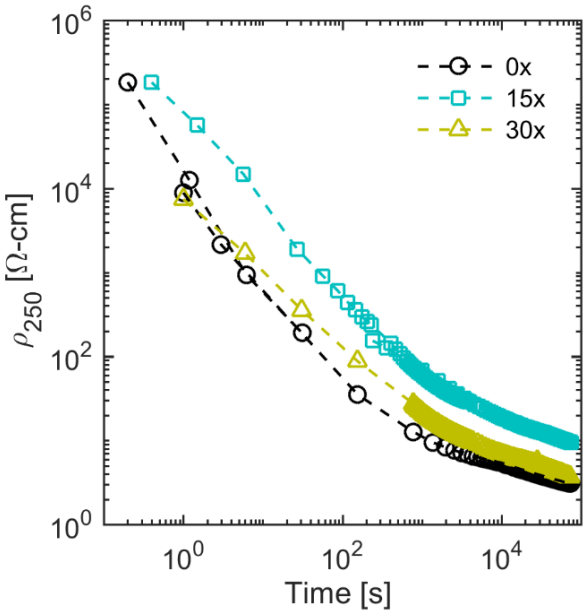

Figure 4.1: Resistivity at 250 K vs UV exposure time for ZnO NCs with partial ALD Al_2O_3 infill. 0x, 15x, and 30x denote 0, 15, and 30 ALD cycles, respectively.

Resistivity as a function of UV exposure time at 250 K for 0, 15, and 30 cycles of infill is shown in Figure 4.1. For all infill levels, the observed trend is generally the same. There is a rapid decrease in resistivity up to ~1 hour, followed by a slower response that does not quite saturate at the longest times measured (approximately 1 day). We see multiple orders of magnitude change, even without considering the as-received data (not shown), which is too high to reliably measure in some films. Regardless of infill, all films approach similar resistivity values with long exposure times, suggesting that the concentration of OH is the dominant factor in variations between samples with different levels of infill. The temperature-dependent resistivity was measured for UV exposure times from 100 ms up to 1 day. Data from a sample infilled with 15 cycles of ALD is shown in Figure 4.2a. In order to unambiguously determine the temperature dependence, we employ Zabrodskii plots[173] of the reduced activation energy, defined as $W = -\frac{dlog\rho}{dlogT}$, where the hopping exponential power factor can be determined from $\gamma = -\frac{dlogW}{dlogT}$. Figure 4.2b shows the Zabrodskii plots for the same data. Starting at 230 s of UV exposure time, a transition from a slope of ~1/4 to ~1/2 is observed, indicating a transition from Mott VRH to ES VRH. Similar transitions

are observed in samples with other degrees of infill, however samples with pre-infill annealing at 300 ˚C in air followed by partial infills follow Mott VRH at all UV exposure times measured, which we discuss below. Figure 4.3 shows the measured values of T_M and T_{ES} temperatures as a function of UV exposure time, where significant differences are observed as a function of both infill and pre-infill annealing at 300 ˚C in air. These characteristic temperatures are extracted from the temperature dependence of resistivity, with $log\rho \propto \left(\frac{T_M}{T}\right)^{1/4}$ for Mott 3D VRH and $log\rho \propto \left(\frac{T_{ES}}{T}\right)^{1/2}$ for ES-VRH.

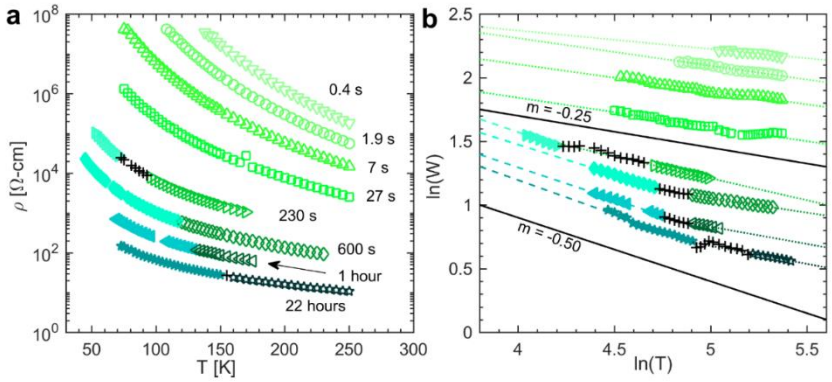

Figure 4.2: VRH transition in ZnO NC films. (a) Resistivity as a function of temperature for NC films infilled with 15 ALD cycles at various UV exposures. A transition from Mott (unfilled) to Efros-Shklovskii (filled) variable range hopping is observed. Current measurements were performed in the dark. (b) Zabrodskii plots for the same data showing the transition from Mott to Efros-Shklovskii variable range hopping. Crosses indicate transition region data points not used for fitting either model. The solid lines labeled m = -0.25 and m = -0.50 serve as guides for the eye to indicate Mott and Efros-Shklovskii VRH regimes.

FTIR absorption data for 15 cycle infill films both with and without 300 ˚C pre-infill anneal is shown in Figure 4.4. Data was collected immediately after H_2O saturation and after UV exposure for a dose equivalent to ~2 hours in the cryostat. The data confirms the suggestion that the most significant chemical change occurring as a result of UV exposure is a reduction in the OH concentration, although it should be noted that the amplitude of the OH absorption feature does not disappear entirely.

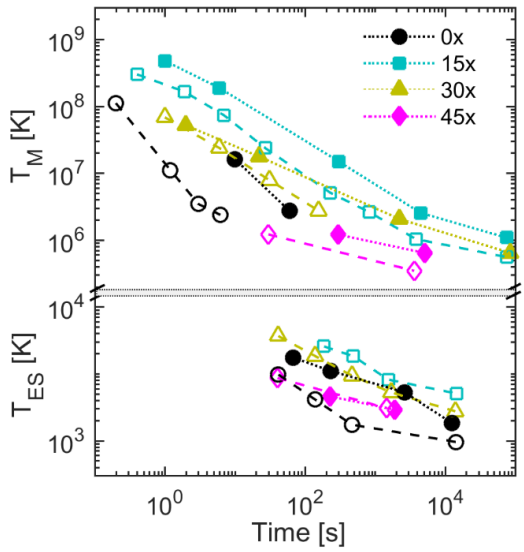

Figure 4.3: Mott and Efros-Shklovskii temperatures as a function of UV exposure time for ZnO NC films annealed at 300 ˚C (filled symbols) and films that have not been annealed (open symbols). The legend denotes the number of ALD infill cycles.

To understand the reasons for differences in conductivity between films with different anneal and infill treatments, we need to first examine the parameters measured by T_M and T_{ES}. The Mott temperature is defined as[80] $T_M = \frac{21.2}{k_B g_0 \xi^3}$ where g_0 is the density of states at the Fermi level and ξ is the electron localization length which indicates the spatial extent of the electron wave function. The average hopping distance is proportional to this localization length, so a larger localization length indicates that the electrons can hop to more distant sites with better energy alignment. The Efros-Shklovskii temperature is defined as $T_{ES} = \frac{\beta e^2}{4\pi k_{eff} \varepsilon_0 k_B \xi}$, where β is a constant given as 2.8 for 3D hopping.[78] Using these definitions, along with the previously defined critical temperature, gives $T_C = \frac{5.9 e^4 g_0 \xi}{4\pi k_{eff} \varepsilon_0 k_B}$.

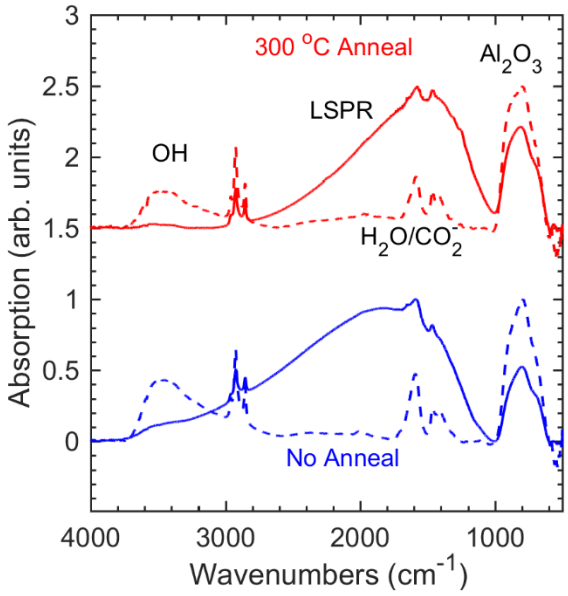

Figure 4.4: FTIR spectra of films infilled with 15 ALD cycles exposed to H_2O to saturation , before (dashed) and after (solid) UV exposure. Annealed (at 300 ˚C) and unannealed films are shown with the spectra for annealed offset by 1.5 units.

We can extract the localization length from the Efros-Shklovskii temperature, while the Mott temperature gives us the density of states. It is only in measurements that show a crossover from one hopping mechanism to the other that we can definitively measure both, although the dielectric constant must be known separately. The effective dielectric constant of the mixed-media film consisting of void (k_i=1) and NCs of ZnO coated with Al_2O_3 (similar dielectric constants taken as k_{NC}~8) at a solid volume fraction (f) from ~40% (no infill) up to ~90% (45x infill) can be calculated using the theory developed by Reich and Shklovskii for an array of touching nanocrystals.[75] From this, our effective dielectric constant is estimated as 3.2, 5.0, 6.2, and 7.5 for no infill, 15 cycles, 30 cycles, and 45 cycles, respectively.

Analysis of crossover measurements, such as those observed in Figure 4.2 starting at 230 s of UV exposure, shows that the density of states does not change significantly as a function of UV exposure time for all films. This indicates that we can assume g_0 to be a constant for a given sample, so we can determine the density of states for any sample where at least one crossover point is observed. The values of g_0 are plotted in Figure 4.5 as a function of infill cycles for both as-deposited and 300 ˚C annealed films. The

density of states increases with infill except for the initial infill of the annealed sample. This may indicate that the Al_2O_3 passivates trap states at the surface of the NCs or that Al acts as a donor near the surface of the ZnO. Both are possible.

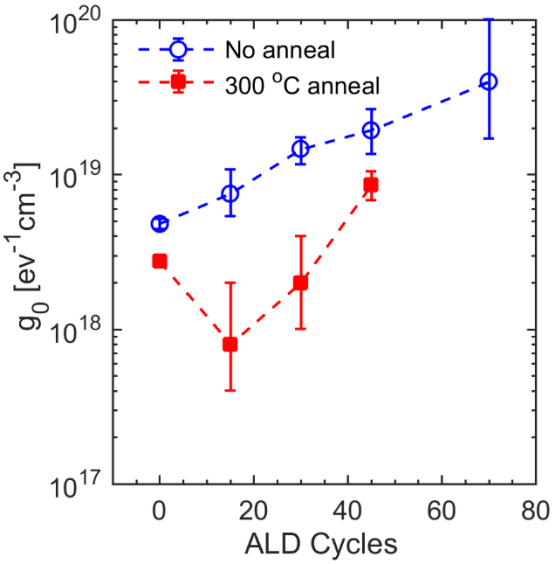

Figure 4.5: Density of states as a function of ALD infill cycles for ZnO NC films that were annealed at 300 ˚C (filled squares) and films that were not annealed (empty circles).

At this point, the localization length can be calculated for all exposure times, using the already determined density of states for times that only show Mott VRH. The data is plotted in Figure 4.6. Most films show localization lengths limited to just under the average NC diameter (d_{NC}~10 nm). There is a notable exception for the films with no infill treatment. The localization length for these films diverges beyond the NC diameter, indicating that the electrons can delocalize across multiple NCs. Similar behavior was observed previously for fully infilled NCs[61]. The localization length calculated here, shown as crosses in Figure 4.6, used the measured values of T_{ES} and assumed a minimum ES to Mott transition of 300 K. These results indicate that infill in itself does not prevent this delocalization.

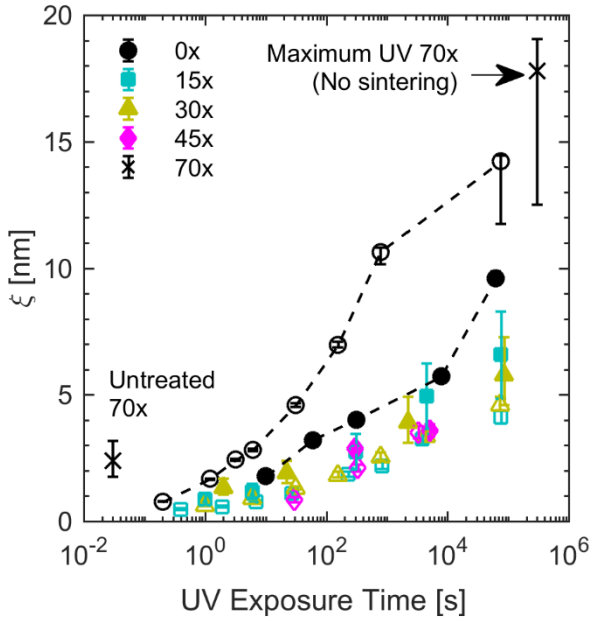

Figure 4.6: Electron localization length as a function of UV exposure time for films that were annealed at 300 ˚C (filled symbols) and films that were not annealed (open symbols) samples. The legend denotes the number of ALD infill cycles. Error bars indicate uncertainty in dielectric constant. The 70x data points are from previous work.[61]

These observations show that the removal of OH increases the localization length but does not alter the density of states for hopping conduction. A model, similarly applied to highly-doped metal oxide nanostructures previously,[174–177] that can be used to explain these results suggests that there is a quasi-neutral core of free electrons in the NC, surrounded by a shell that is depleted of free electrons by OH on the surface (Figure 4.7). As OH is removed, the core expands, increasing ξ. However, the density of states at the edge of the core remains roughly constant. In the case of no infill, the NC-NC interface has a relatively low defect density, and so the edge of the core approaches the diameter of the NC near these adjacent facets. Ultimately, the electron wave functions of adjacent NCs overlap enough to delocalize the electrons across the interface.

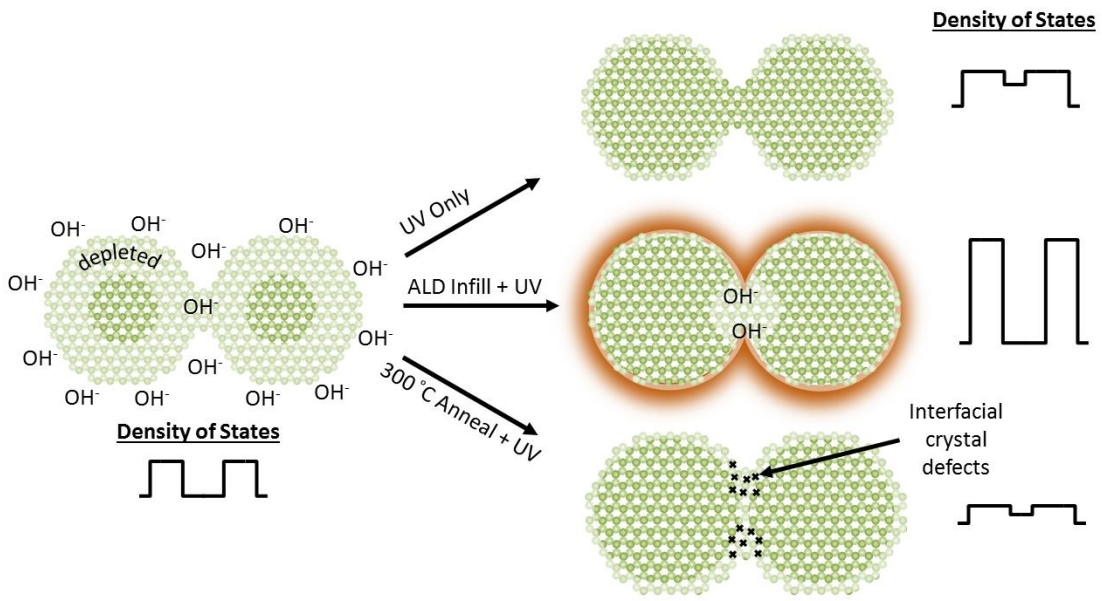

Figure 4.7: Model of surface and interface depletion in ZnO NC films before and after exposure to UV light for different post-deposition treatments.

The reason for limited delocalization in infilled films may be related to a higher concentration of traps near the NC-NC interface in these films. This interface is of primary importance to conduction as it presents the shortest tunneling distance for electrons to move from one NC to another. However, this will also be exactly the area that is most prone to defect formation resulting from the aforementioned limitations of the infill process. The variable spacing between NCs inevitably creates crevices where a small molecule like H_2O and trimethyl aluminum decomposition byproducts such as CH_3 may easily penetrate while a larger molecule like $Al(CH_3)_3$ will not. Repeated ALD cycles in these areas are likely to create ZnO surfaces that remain OH terminated or have oxygen vacancies. Thus, ALD is likely to increase trap densities at these interfaces, even as it reduces trap densities for most of the film. The infill layer may also trap species in the spaces between crystal facets, maintaining a highly localized density of defects even as UV exposure removes OH from the bulk of the film.

Previous work done with fully infilled samples showed large localization length upon UV exposure[61] in contrast to our observations. However, that work used high-intensity pulses of UV light, with each 1 ms

pulse delivering the energy equivalent to 2400 s of the present work. This high power density leads to significant heating of the NCs, enabling sintering (increasing NC-NC contact area) in films without infill, while the authors saw no evidence of further sintering when exposures were performed after infilling. However, even without any increase in contact area, it is possible that the high-intensity UV exposure is capable of removing and/or repairing defects near the interfaces. It is unlikely that this explanation applies here since the UV exposure in this work has a power density that is more than 10^6 lower.

We also note a general decrease in both g_0 and ξ in films that were annealed at 300 ˚C prior to infilling. This process was previously thought to mimic the intense UV treatment described above, as we measured a slight increase in crystal size with more pronounced growth at higher temperatures. However, there are apparent differences in conductivity, with the thermally annealed films not showing the increase in conductance expected for the larger NC-NC contact area. The likely reason for this is the aforementioned spatially localized defects near the interface. Relative to the plasma synthesis or intense UV treatment, a 300 ˚C anneal would be expected to grow a lower quality crystal with a higher concentration of defects. It is also possible that the growth of Al_2O_3 on the surface of annealed ZnO is not as effective as it is on untreated ZnO, introducing additional trap states instead of passivating the surface. In either case, the effect is not large enough to completely prevent delocalization, which should still be assisted by the increase in contact area, but does have a measurable effect on the density of states. It is for this reason that no transition to ES VRH is observed in annealed films with 15 or 30 cycles of infill. Further evidence for the reduction of density of states in annealed films is found in our FTIR data (Figure 4.4), as well. The LSPR feature is suppressed in the annealed film relative to the film without anneal, indicating a lower electron concentration.

It should be noted that, while all the changes in NC structure discussed here (infill, adsorbed chemical species, annealing/sintering) are localized to the NC surfaces and would not be expected to affect the quasi-neutral core, infilling and annealing are both associated with changes in g_0. In contrast, the desorption of

surface species appears to only affect ξ while leaving g_0 unchanged. The quasi-neutral core and depleted surface are not, in actuality, absolutely distinct as the depletion is a result of band bending in the outer volume of the NC. If the band bending occurs more steeply (due to higher charge density in the outer volume), this would allow electrons in high-density states to extend further out to the surface where they can easily contribute to the tunneling process. For more gradual band bending, electrons closer to the surface would occupy lower-density states, resulting in a lower average hopping density of states. Therefore, we suggest that thermal annealing and ALD infill affect the extracted density of states by altering the charge density in the outer volume of the NCs, which is directly connected to the slope of the band bending. In contrast, the density of states is not dependent on the concentration of adsorbed surface species because they do not have any effect on the slope of the band bending,

4.4 ZnO Admittance Spectroscopy: Applicability and Challenges

Thermal admittance spectroscopy (TAS), which has been used on other NC-based films[93,140,142,178], has not been reported on ZnO NC films. In this measurement, the complex admittance ($Y = G + j\omega C$) is measured as a function of temperature. The dielectric loss (G/ω) is maximized when $\omega=1/\tau_0$, where τ_0 is the time constant of a given charge transport process. In the typical analysis, this often corresponds to an emission time from a mid-gap trap state.

One detail of our method that had not been explored in previous work is the inclusion of a bottom oxide layer for electrostatically controlling the charge carrier concentration. We based this approach on a technique called the Conductance Method, which was developed for measuring interface states in MIS transistors[126]. By controlling the carrier concentration with the gate electrode, it may be possible to observe transitions in the conduction mechanism, such as changes in hopping behavior[107] or allow for the measurement of NC surface states[2,179].

Traditional MIS capacitors exhibit a frequency dependence in inversion due to the inability of the generation/recombination process to follow the applied signal at sufficiently high frequency. This

frequency dependence is generally related to a combination of interface states and mid-gap states that are present in the bulk. Here we see something quite different, the inability of majority carriers to follow the applied signal in accumulation. This has to be viewed not as a limitation of carrier creation/annihilation but rather transport. The dc measurements indicate that variable-range hopping dominates the conductance. In this case, the only relevant time constant is the dielectric relaxation time τ=RC. An emission or capture process within a NC is only relevant if it takes place on time scales comparable to or slower than the time that it takes for charge to be transported off of the NC.

Therefore, although the results discussed here do not directly measure conductance, conductance plays a major role in interpreting the results. This interpretation is reflected in our measurements, which show an extracted Mott temperature that is in good agreement with that found through dc measurements. Figure 4.8 shows linear fits for Mott temperatures for a 15 cycle infill film, as-received. The time constants for a range of TAS biases along with the lateral I-V resistivity data were converted into the equivalent RC time constant ($\tau = \rho\varepsilon \frac{t_{NC}}{t_{ox}}$). In all cases the values are in good agreement, demonstrating the equivalence of these measurement techniques.

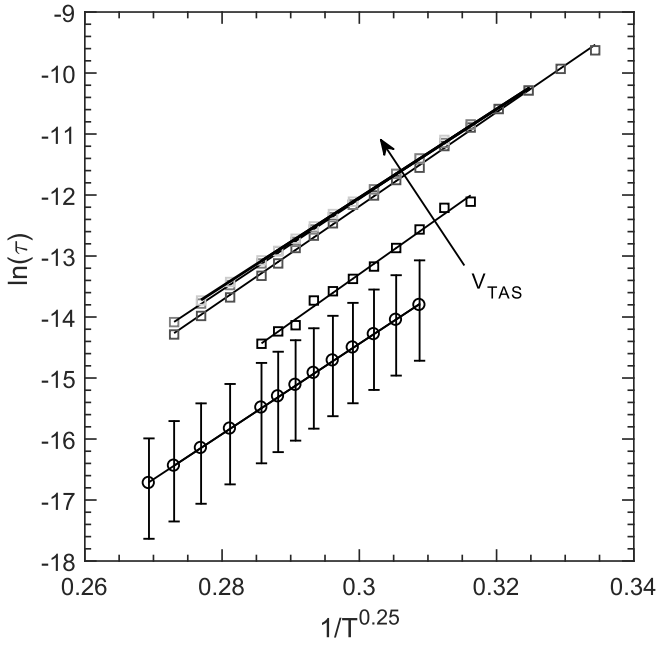

Figure 4.8: Comparison of Arrhenius plots for lateral I-V vs vertical TAS , represented by circles and squares, respectively. For the dc data, measured resistivity was converted to a time constant as $\tau = \rho k_{ox} \varepsilon_0 \frac{t_{NC}}{t_{ox}}$, and the error bars reflect uncertainties in these factors. The slope is comparable for all cases, demonstrating that the two measurements are equivalent. V_{TAS} indicates the applied dc bias for the TAS measurement, with the arrow indicating increasing bias.

In light of this, we can conclude that TAS measurements in these ZnO films do not extend the knowledge gained from simple dc conduction measurements, other than the trivial difference in accessible range due to geometry and choice of equipment that has allowed us to collect data from our most resistive samples only through TAS. It is still worthwhile to analyze the data obtained from our admittance spectroscopy measurements, particularly as it pertains to the NNH regime observed in high-resistivity films. The observed spectra and Arrhenius behavior could be interpreted as evidence of mid-gap trap states, but we propose that this is not the correct interpretation here. In analyzing any of this data, it is important to determine the appropriate temperature dependence, as this will reveal the underlying conduction mechanism. As stated earlier, previous work on fully infilled, high conductivity ZnO NC films consistently showed ES-VRH, with $\log \rho \propto T^{-1/2}$. The partially infilled films shown in Figure 4.8 generally follow M-VRH, with $\log \rho \propto T^{-1/4}$, while in their more conductive state. However, we have

observed a transition to NNH or trap-limited response with a direct T^{-1} dependence, distinct from the lateral I-V response. An example of this is shown in Figure 4.9, which shows data for a film with 20 ALD infill cycles. This is an example of the inconsistency inherent to measuring nominally as-received films, especially when one attempts to compare measurements performed laterally to those performed vertically. In this case, the volume of film active in the vertical measurement is entirely underneath the Al top contact, blocking any ambient light while also altering the relevant diffusion geometry for gaseous species. As a result, the surface chemistry of these NCs can easily be significantly or even drastically different from that of the NCs involved in the lateral measurement. Therefore, entirely different conduction mechanisms can be observed, a difference that can be difficult or impossible to precisely control.

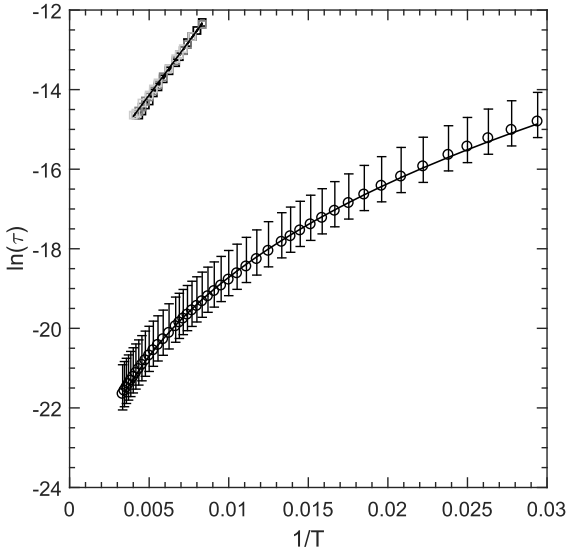

Figure 4.9: Arrhenius plots for lateral IV vs vertical TAS at a range of biases , represented by circles and squares, respectively. The TAS data is linear with 1/T instead of $1/T^{1/4}$, indicating NNH conduction. For the dc data, measured resistivity was converted to a time constant as $\tau = \rho k_{ox} \varepsilon_0 \frac{t_{NC}}{t_{ox}}$.

4.5 Conclusion

In summary, our work supports the model that delocalization across the NC-NC contact facet plays a key role in conduction in ZnO NC films proposed by Greenberg,[60] even without infill or sintering. In this model, infilling with Al_2O_3 increases the density of states by passivating defects on the NC surface and/or by doping of the ZnO with Al. However, the data suggests that the infill near the NC-NC interface is of

low quality, creating a high density of defects localized near this region. The origin of these defects remains unknown. It is possible that it is simply a high concentration of OH or decomposition byproducts that are more tightly bound and so are difficult to remove with UV exposure. The infill itself would also serve to seal in these volumes, such that desorbed OH would diffuse out much more slowly. The use of UV to controllably remove adsorbed OH appears to be a very effective technique for detailed study of semiconducting NC films.

4.6 Future Work

There are several questions from this work that remain unsolved. The first is what exactly is the difference in the NC films treated with high-intensity UV light and those treated with low-intensity UV light, particularly as it pertains to infilled films. We attribute the small electron localization lengths observed in partially infilled films treated with low-intensity UV light to defects localized to the NC contact facets and infer that these defects are repaired or removed with high-intensity UV exposure. What would happen if these films were removed from the cryostat and exposed to high intensity UV light, followed by H_2O saturation? Would the localization length now follow a similar trend to that of untreated films? Can we analyze the contact facet in more detail between these scenarios? TEM measurements might be useful for this, as well as comparing UV sintered vs thermally annealed NC contacts, although the area of interest might be difficult to resolve and compare. Previous attempts to analyze this interface to quantify the expansion of contact facet size upon sintering were inconclusive. Maybe a more detailed FTIR study can shed insight into chemical bonding differences. Additionally, given the dramatic change in localization length behavior between no infill and 15 cycles of infill, it would be interesting to test smaller numbers of infill cycles to see if a transition can be observed or if this change happens with any number of infill cycles. In line with this thought, what effect do other infill materials, such as HfO_2, TiO_2, or even PEALD TiN, have on these measurements. Is the ALD material simply acting as a barrier to hydroxyl adsorption, or does the chosen material have an effect? Can this be used to tune the conduction or plasmonic properties?

5 Defects and Transport in Ge NC Films

5.1 Introduction

Group IV materials have a long history of extensive use in semiconductor electronics, but elemental Si and Ge NC development lags significantly behind that of other materials, such as metals (Au, Ag, etc.), metal oxides (ZnO, TiO_2, etc.), and metal chalcogenides (PbSe, PbS, CdSe, CdS, etc.). This is despite the fact that Si and Ge are abundant and nontoxic materials that are already well established in device manufacturing. The main difficulty has been the high crystallization temperature for Si and Ge,[15] which makes them difficult to synthesize through common solution-based processes. The use of RF plasma reactors has enabled us to synthesize these materials with high quality[54,56] and to study them in a variety of devices.[2,6,38,179–182]

This work was motivated by an earlier study from Professor Kortshagen's group led by Zachary Holman.[2] They reported the use of Ge and Si NCs synthesized using plasma reactors in FETs, with the Ge NC devices showing particularly good performance. Hole mobilities as high as 0.02 $cm^2 V^{-1} s^{-1}$ were reported, with on/off ratios $>10^3$. Data from this work is shown in Figure 5.1.

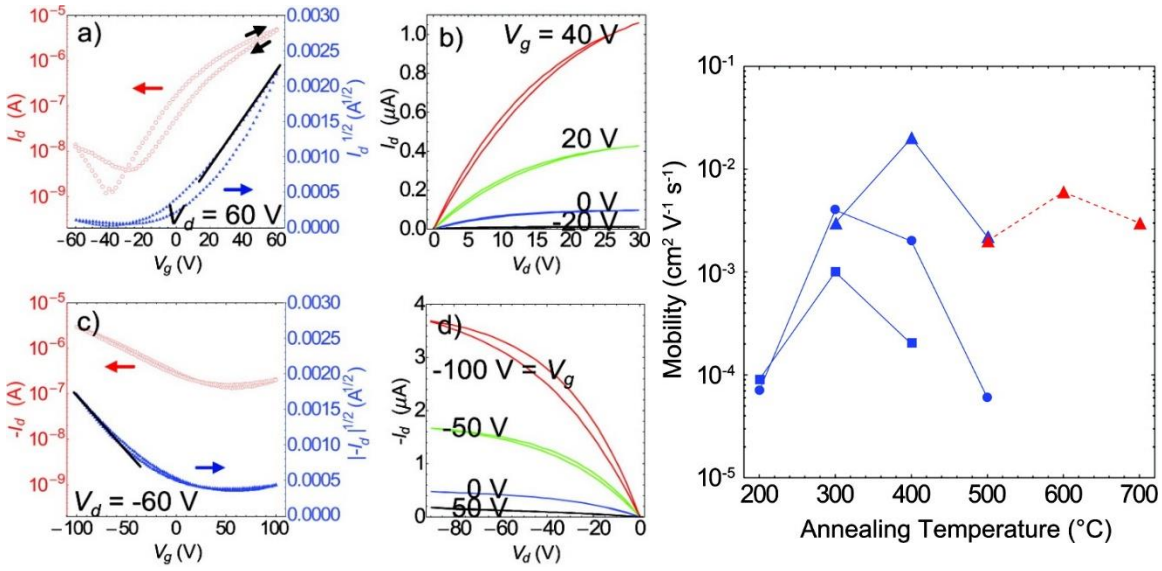

Figure 5.1: Transfer and characteristic curves for Ge NC FETs deposited from solution and annealed at 400 °C (a,b) and 600 °C (c,d). Transfer curves show fit (black line) used to extract the mobility (right). Marker shapes indicate different annealing methods, with triangles corresponding to the RTA system used in the present work. Figure extracted form Holman et al.[2]

As can be seen, there is a change in the conductivity from n-type to p-type as the annealing temperature is increased. The proposed model for these changes was a combination of: i) removal of surface bound H and Cl species at lower temperatures (up to ~400 ˚C) ii) surface oxidation and iii) NC grain growth at higher temperatures (beginning at 400 ˚C or 500 ˚C, depending on the method of annealing). Unlike the well-known passivating nature of H in Si,[183] the energetic position of H in Ge is such that the bond acquires a negative charge.[184,185] Cl is similarly electronegative in Ge,[186] and Ge dangling bonds (such as would be expected at the untreated NC surface) are generally located below mid-gap, close to or below the top of the valence band.[185,187,188] This is used to explain the increasing electron conduction as H and Cl are removed with heating. In addition, O and OH have been observed to act as donors at Ge surfaces,[189–191] providing explanation for the improved performance of Ge FETs annealed in the RTA, which required the highest exposure to air during processing. The p-type behavior and increased conductivity observed at higher annealing temperatures is most likely associated with "bulk" effects as the NC grains begin to grow and the surfaces become less important and could be related to the diffusion of surface species into the core of the NCs.

The initial work on Ge NC FETs demonstrated the feasibility of these devices along with a basic theory of their operation, but a deeper understanding of the role of defect states was left unexplored. Without this knowledge, it will not be possible to significantly advance these materials for use in practical devices. The unmeasurably low as-deposited conductivity, along with the significant hysteresis and strongly shifted threshold voltage observed in Figure 5.1a, suggest a high density of defects. Thermal annealing appears to remove these defects or otherwise lessen their impact on device performance, but further knowledge of the defects' role in the conduction process would allow further improvements to be made.

5.2 Experimental Methods

Films of Ge NCs were synthesized using the processes described in Section 1.2 and deposited via inertial impaction. Briefly, gas flow rates of 25 sccm Ar and 20 sccm H_2 were injected prior to the synthesis plasma, with an additional 10 sccm Ar injected downstream. This allows one to switch to core/shell NC growth without changing the physical setup of the system. The reactor pressure with these flow rates was ~1.75 torr, at which point $GeCl_4$ was introduced at the upstream injection point to increase the pressure by 30 mTorr. The RF plasma power source was 50 W at 13.56 MHz. These conditions produced Ge NC with a mean diameter of ~6 nm. Film thicknesses ranged from 100-300 nm, depending on the deposition times and substrate sweep rate. Film densities were not directly measured, but the work of Hollman from his development of this synthesis and deposition procedure provides an estimate of ~40% solid volume fraction.[192]

For thermal admittance spectroscopy (TAS) measurements, Ge NCs were deposited onto substrates with pre-patterned electrodes for a vertical measurement geometry. Unless otherwise noted, these bottom electrodes consisted of 15 nm Ti/60 nm Au deposited by sputtering on an oxidized Si wafer. However, some devices were made using indium tin oxide (ITO) on a glass substrate. Insulated bottom electrodes were used for electrostatic control of the surface potential in the Ge NC films. The insulator for TAS devices was 11 nm of Al_2O_3 grown using an UltraTech/Cambridge Nano Tech, Inc. Fiji 200 Gen 2 plasma-enhance atomic layer deposition (PEALD) system at 250 ˚C and annealed in a Modular Process Technology Corp. RTP-600S rapid thermal annealing (RTA) system using forming gas (95% N_2/5% H_2) for 5 minutes at 420 ˚C. The measured capacitance of these films was ~700 nF/cm^2 ($\varepsilon_r \cong 8.7$) with a leakage current <1 nA/cm^2 at 1 V. For field-effect transistor (FET) devices, the substrates were processed similarly, but the Al_2O_3 thickness was increased to 55 nm (~140 nF/cm^2) for increased reliability and to ensure low leakage across a wide range of applied fields.

Post-deposition NC treatments were used to modify the conductivity of the films, namely thermal annealing and ALD infilling with Al_2O_3. Thermal annealing was performed in the same RTA system, as per earlier work with Ge NCs,[2] consisting of a 10 minute anneal in N_2 (10 slm) at atmospheric pressure with a 3 minute purge before heating to temperatures ranging from 300 ˚C to 500 ˚C. ALD infilling followed the procedure developed for passivating ZnO NC films, discussed earlier,[3] using trimethylaluminum (TMA) and H_2O as precursors and lengthened pulse/purge times (0.1 s and 30 s, respectively) to allow for full diffusion into and out of the porous films.

Finally, top contacts were deposited through a steel shadow mask. An important detail to note for these devices is that, due to the need for low oxide leakage, the shadow mask was designed so that physical contact between the sample and the mask did not coincide with the area of metal deposition. The relatively poor mechanical strength of the NC films combined with thin insulating films allowed micro-scratches to develop as a result of contact between the mask and the sample. If metal were then deposited onto these scratches, the leakage was found to increase dramatically, even resulting in complete shorting. This is a point that should be considered in any future work. In FET samples, the same mask was used with a 250 μm or 500 μm diameter wire used to mask the channel.

The top contact material was either Al (300 nm) or Au (120 nm), as noted in the results and discussion, below. Al was deposited using a thermal evaporation system contained within a N_2 glovebox, allowing for air-free processing. However, this was generally impossible to achieve in this work due to the fact that the RTA, ALD, and measurement systems all required some exposure to air for loading/unloading. Au was deposited using an AJA International ATC 2200 sputtering system with a DC plasma. For all FET devices, the contacts were annealed at 400 °C or 300 °C for Al and Au, respectively. This anneal was performed in the same RTA system as other anneals. For TAS-specific devices (without a channel), this step was generally

neglected because we weren't sure about the effect this would have on vertical measurements with such thin films.

All electrical measurements were performed in a cryogenic vacuum test station, consisting of a copper sample stage with an embedded resistive heater and RTD sensor mounted to a cold head. The cold head was cooled by a helium compressor refrigerator and was capable of reaching temperatures of ~20 K, while the sample stage could be cooled to ~30 K. The temperature was regulated by PID-controlled operation of the resistive heater.

5.3 Results and Discussion

Room temperature lateral I-V measurements of ~100 nm thick untreated Ge NC films showed resistivity values of about $10^7\ \Omega\ cm$, while vertical C-V indicated the films were fully depleted with no bias dependence. Infilling with 70 cycles of ALD Al_2O_3, which has been shown to fill the pores of similar NC films to ~100% solid fraction,[53] gives rise to an immediate order of magnitude improvement in conductivity, with a measured room temperature resistivity of $4.7 \times 10^5\ \Omega\ cm$. Measurable C-V for these films made possible the use of TAS measurements to investigate the defect state distribution. The samples for this measurement consisted of ITO/glass substrates and Al top contacts. After cooling the sample to the chosen starting temperature (generally -120 ˚C was sufficiently cold as to remove any frequency response), the sample temperature was increased incrementally, with time for stabilization at each measurement point, up to 150 ˚C. This was followed by an extended bake (>1 hour) at this temperature and cooldown measurements to reverse the heating steps. Each measurement consisted of a frequency scan of the complex admittance $Y(\omega,T) = G(\omega,T) + i\omega C(\omega,T)$ at zero DC bias. The resonant frequency is measured as a peak in either the capacitance slope or the dielectric loss (G/ω).

$$\frac{d}{d\omega}\left(\omega\frac{dC(T)}{d\omega}\right)_{\omega=\omega_0(T)} = \frac{d}{d\omega}\left(\frac{G(T)}{\omega}\right)_{\omega=\omega_0(T)} = 0 \tag{5.1}$$

The resonant frequency depends exponentially on temperature as $\omega_0 = \frac{1}{\tau_0} \propto exp(-\frac{E_a}{k_B T})$, such that the activation energy E_a can be extracted from the linear fit of $ln(\tau_0)$ vs $1/T$. The data from before (solid

lines, diamonds) and after (dashed lines, circles) baking at 150 ˚C is shown in the left side of Figure 5.2. The extracted activation energy increases from an initial value of 410 meV to a post-bake value of 510 meV and coincides with a decrease in conductivity of ~40% and a decrease in the low-frequency capacitance of ~25%. The right side of Figure 5.2 shows the same data for a Ge NC film annealed at 500 ˚C before being infilled with ALD. The as-received conductivity of this film is much higher than that of the unannealed film, with a measured room temperature resistivity of $1.2 \times 10^3\ \Omega\ cm$, with a similar ~40% decrease in conductivity after baking at 150 ˚C. However, the frequency response does not follow the same trend. In this film, two distinct features are observed in the capacitance spectra: i) a larger time constant response with an activation energy of 300 meV and ii) a smaller time constant response with a larger activation energy of 350 meV that decreases to 310 meV after baking. It is interesting that the response with the larger activation energy has a time constant ~2 orders of magnitude lower than the smaller activation energy response, which can be explained by a dramatically different y-intercept in the Arrhenius plots, also known as the attempt frequency. The attempt frequency characterizes the strength of the interaction across the energy barrier. Such a large difference in attempt frequency would be a signal that these responses arise from very different sources.

Unlike the unannealed sample, the activation energy change in the sample annealed at 500 ˚C does not seem to track the change in conductivity. In both cases, the conductivity decreases after baking, but the activation energy in the annealed sample decreases, which is the opposite of what one would expect. It should be noted, however, that the changes in conductivity observed with baking would require only a 10-15 meV shift of the Fermi level away from the band edge, assuming $\sigma \propto exp\ (-\frac{E_F}{k_B T})$. One explanation for this data could be that the lower energy response in the annealed sample (filled symbols in Figure 5.2) is due to mid-gap states in the NCs themselves, while the larger energy response (open symbols) is related to non-ohmic contacts. Reports on contact to bulk Ge have indicated strong Fermi

pinning of contacts such that the barrier height is independent of metal work function.[193] As a result, it may not be surprising that the ITO/Ge/Al structure may include two Schottky junctions.

In order to connect our analysis to the performance of Ge NC FETs, new FET devices were fabricated, as detailed above. The long channel (250-500 μm) was intended to minimize the effect of contact resistance so that we could more specifically measure the charge transport of the NC films themselves. Transfer curves (channel sheet conductance as a function of gate bias) at drain voltages of ± 1 V are shown in Figure 5.3 for Ge NC films annealed at 500 ˚C. The first feature to note is the relatively large and variable hysteresis in all measurements. Reducing the gate bias sweep rates to 1 V/s produced only a small reduction in hysteresis. This is generally indicative of large trap concentrations, which would not be particularly surprising. In line with this, the device that was fully passivated with ALD Al_2O_3 (solid black lines) shows the smallest amount of hysteresis and the largest conductance, in general.

The blue and gold dashed lines correspond to films without ALD infill with Al and Au contacts, respectively. The reported ambipolar behavior reported in earlier work is not observed in these devices, which are nominally the same, although some device parameters and processing steps differ. Specifically, the previous work used spin coating for NC deposition instead of impaction from the gas phase. The NCs were not functionalized for solution processing, but the solvent itself may have some unintended effects. The reasonable minimum thickness of the impacted films is larger than that for spin coated films. The former is estimated as 100 nm with thickness variations of up to 5-10 monolayers (30-60 nm) while spin coating was used to deposit thinner, smoother films of ~30 nm with 10 nm roughness. Finally, the gate metal and insulator was changed for the present work. The original Ge NC FETs were deposited on heavily doped Si wafers with 300 nm SiO_2 as a gate insulator, while the current devices are deposited on pre-patterned Au electrodes with 55 nm Al_2O_3 as a gate insulator.

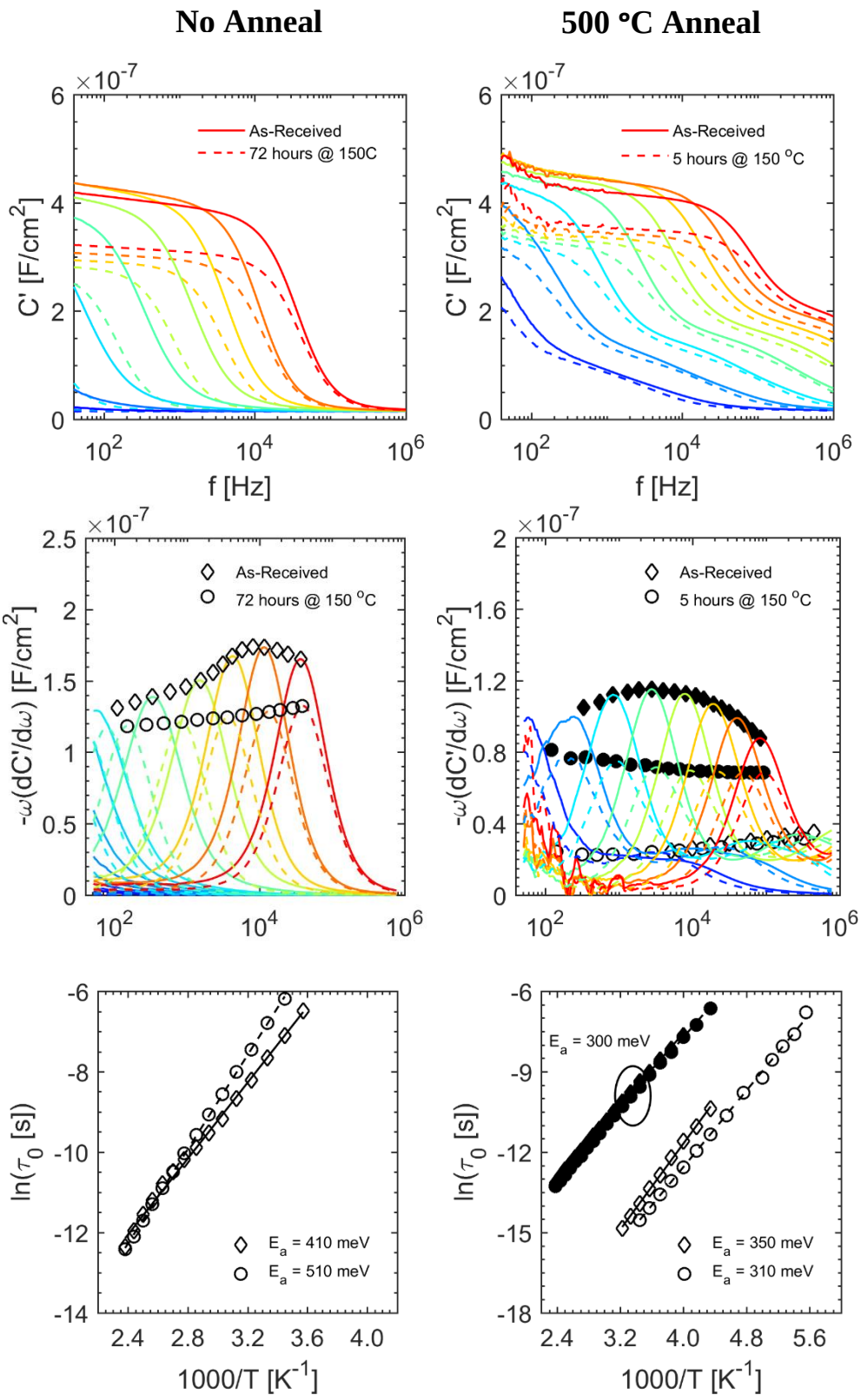

Figure 5.2: TAS data for Ge NC film infilled with 70 cycles of ALD Al_2O_3 before (solid lines, diamonds) and after (dashed lines, circles) baking in vacuum at 150 °C.

Despite these difference, the measured electron mobilities are quite similar. For an annealing temperature of 500 ˚C (see Figure 5.1), electron and hole mobilities of about $2 \times 10^{-3}\ cm^2\ V^{-1}\ s^{-1}$ were reported (the contact material was not specified, except to indicate that either Al or Au were used throughout the experiment). In the current work, the mobility was extracted from the slope of the transfer curve in the linear regime (high gate bias, low drain bias) as $\mu = \frac{1}{C_{ox}} \times \frac{L}{W} \times \frac{\partial I_D}{\partial V_g} = \frac{1}{C_{ox}} \times \frac{\partial G_{sh}}{\partial V_g}$. Using the data in Figure 5.3, the electron mobility for as-received devices is measured as 8×10^{-3} and $5.1 \times 10^{-3}\ cm^2\ V^{-1}\ s^{-1}$ for Al and Au contacts, respectively. The former is comparable to the highest mobility measured in the previous work, recorded for an annealing temperature of 400 ˚C. In both cases, after baking at 130 ˚C for 1 hour, the mobility decreases. For Al contacts the decrease is less severe, dropping to $2.6 \times 10^{-3}\ cm^2\ V^{-1}\ s^{-1}$, approximately a 67% reduction. For Au contacts, on the other hand, the mobility drops by over an order of magnitude to $2.7 \times 10^{-4}\ cm^2\ V^{-1}\ s^{-1}$. The reason for this difference is not immediately obvious, however it is worthwhile to observe that unlike Al, Au diffusion in Ge is controlled by interstitial processes with extremely low activation energies[194,195] and it is known to produce deep states. Thus, the annealing Au contacts may lead to a degradation of the contact by an increase in mid-gap traps that localize charge and increasing the relative negative effect of *in situ* baking on device conductance. Given the potential effects on the contact, it is possible that the chosen channel length was insufficient to ignore the contact voltage drop and so measure the true carrier mobility. We would also expect, in general that Au would not make ohmic contact to n-type Ge given the large offset between the work function of Au (5.1 eV) and the conduction band of bulk Ge (4.0 eV). This difference would be expected to grow even larger due to confinement effects.

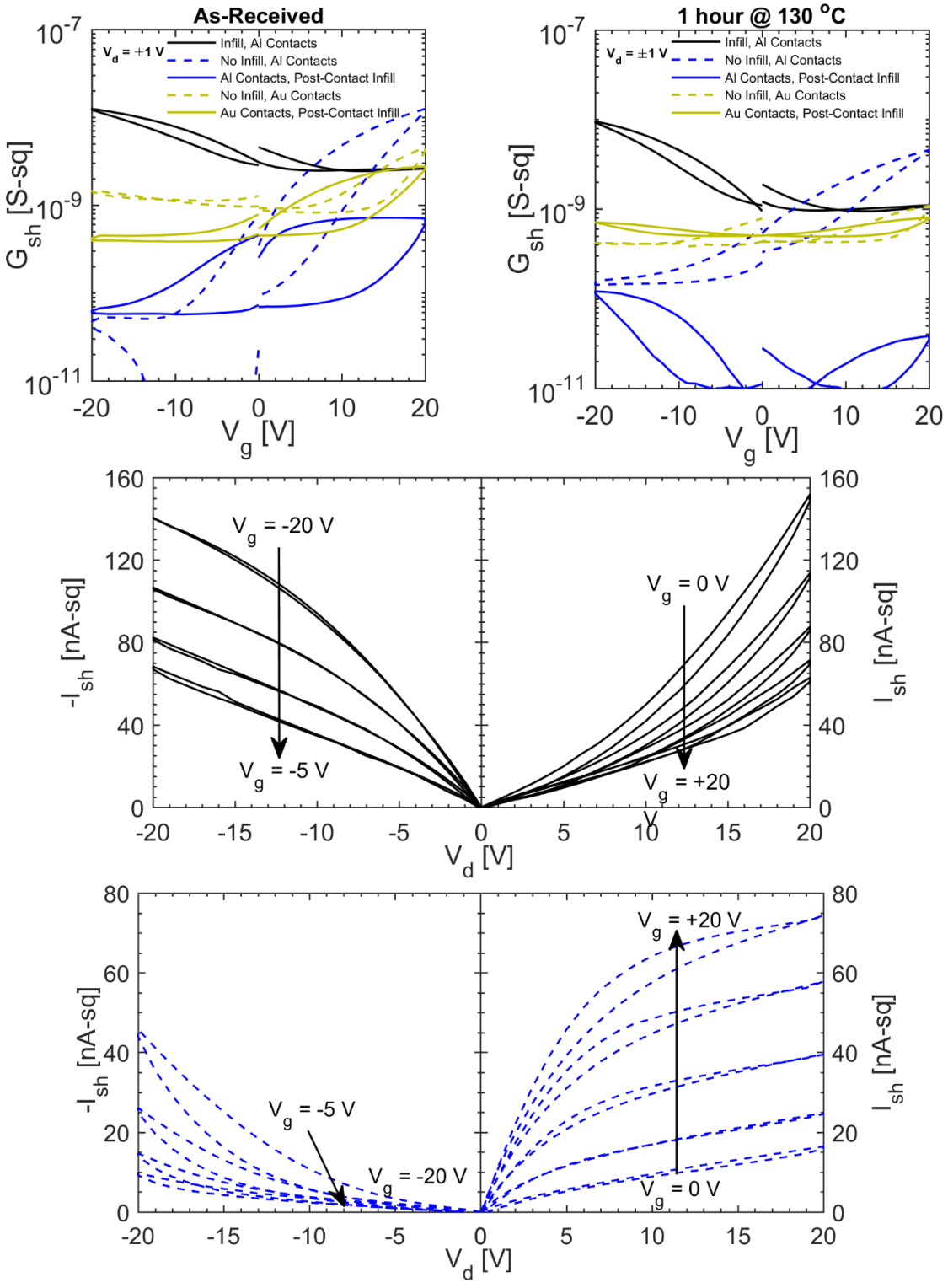

Figure 5.3: I-V measurements for Ge NC FETs deposited from the gas phase. (Top) Transfer curves for Ge NC FETs. All films were annealed at 500 °C after deposition. Left plot shows measurements after pumping down overnight, while the right plot is after a subsequent bake at 130 °C for 1 hour in vacuum. (Middle, Bottom) Characteristic curves for devices before baking.

The most interesting behavior is observed when the Ge NC film is infilled with ALD Al_2O_3 (solid lines in Figure 5.3). Infill could be performed either before or after contact deposition, with a slow etch in dilute 500:1 buffered oxide etch (BOE) to remove the ~7 nm of surface oxide on top of the NC film in the former case. This step was also included for devices with infill after contacts and had no measurable effect. If the infill is performed after contact deposition (solid blue and gold lines), a slight decrease in the conductivity is seen. In the case of Al contacts, this is at least partially explained by oxidation of the metal/NC interface during the high temperature, high humidity ALD process. However, the same trend (if less severe) is observed for Au contacts, which would not suffer from the same limitation. In the case of infilling before contact deposition (black lines in Figure 5.3), an entirely different behavior is observed. In such a device, only p-type conduction is observed, which was true even for films annealed at temperatures as low as 300 ˚C, far from the transition to p-type conduction seen in Figure 5.1, albeit with significantly reduced mobility at lower annealing temperatures. The mobility for films annealed at 500 ˚C was $4.7 \times 10^{-3}\ cm^2\ V^{-1}\ s^{-1}$ before baking and increased very slightly to $5.0 \times 10^{-3}\ cm^2\ V^{-1}\ s^{-1}$ after baking at 130 ˚C for 1 hour.

The channel material in all the devices corresponding to solid lines in Figure 5.3 is identical. However, the contacts are not, due to the fact that the ALD infill is unlikely to penetrate more than ~1 μm underneath the contacts due to geometrical factors. With a bottom gated thin film transistor, the contact essentially consists of the series combination of the metal/NC contact, the conduction vertically through the film, and the interface between the upper NC layers and the gated channel made up of the bottom most layer of NCs. TAS measurements using FET devices, either specially made without a channel or with the source and drain tied together, present a method for probing just such behavior.

Results from TAS measurements with Ge NC FET devices are shown in Figure 5.4. Figure 5.4a shows the change in resonant frequency $\omega_0 = 1/\tau_0$ relative to the frequency ω_e at the maximum positive bias for electron injection, about $2.7\ MV/cm$, measured at a single temperature (250 K for the device

with Au contacts, 300 K for all others). This matches with the FET measurements that showed n-type conduction in films without infill and p-type conduction in films with infill. Figure 5.4b shows the measured activation energies, $ln\tau_0 \propto \frac{E_a}{k_B T}$, as a function of bias. The observed trends are the same, although it is worth noting that the magnitude of energy shift with bias are not the same between the two plots, indicating that the attempt frequency is not constant with bias, as was implicitly assumed in Figure 5.4a.

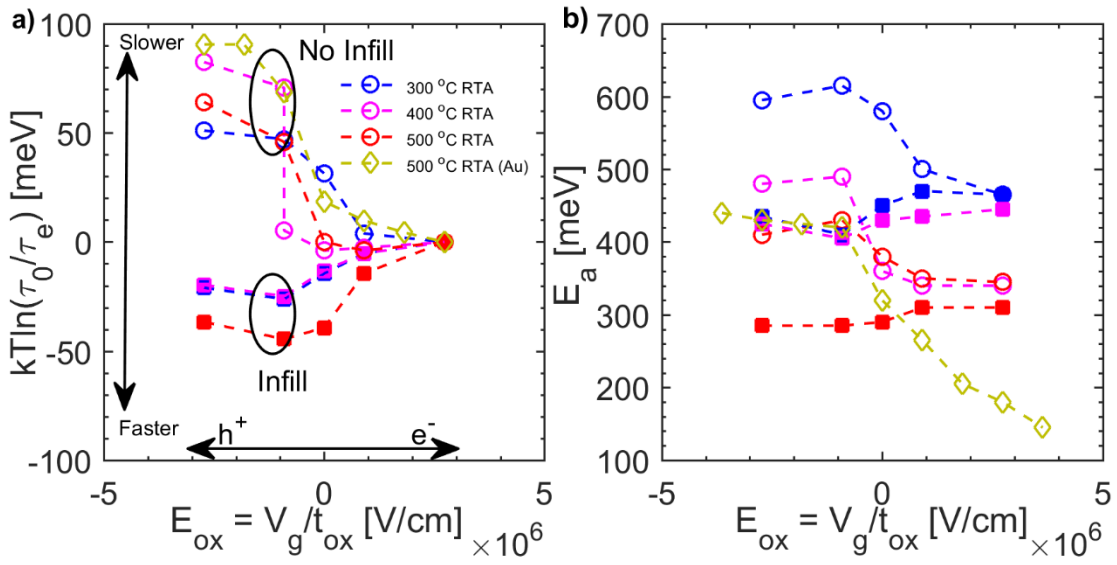

Figure 5.4: TAS measurements for Ge NC FETs. a) TAS time constant shift vs gate bias. All samples were baked in-situ for 1 hour at >100 °C. The data shown for gold contacts (gold diamonds) was collected at 250 K to observe the resonant response within the measurement window (40-10^6 Hz) at all biases. All other data was collected at room temperature. b) Activation energy vs gate bias for the same devices. Activation energies were determined by linear fits of $\boldsymbol{ln(\tau_0) = \frac{E_a}{k_B T} + b}$.

The activation energies measured for Ge NCs annealed at 500 ˚C before infilling change only on the order of 10% across the range of biases used in this measurement. This is not large enough to reasonably explain the large difference in electron and hole currents in this device. However, the TAS devices did not include a final contact anneal due to initial concerns that this step might irreversibly alter the NCs below the contacts, which we wanted to avoid. Figure 5.5 shows measured C-V characteristics for TAS devices with Al and Au contacts (left and right plots, respectively). The measured capacitance values for Al contacts without annealing (blue) are significantly smaller than those for Au contacts. This can be

explained by a large series impedance as a result of poor contact between Al and the Ge NC film, while the capacitance of the device with Au contacts approaches the Al_2O_3 capacitance ($\varepsilon_r \cong 8.5\ to\ 9.0$) at both bias extrema. After annealing the Al contacts at 400 ˚C, the capacitance increases to match the device with Au contacts. Further confirmation of the improvement in Al ohmic contact after annealing is seen in the corresponding capacitance spectra shown in Figure 5.6. On the left, a distinct resonance is observed at T=203 K for positive gate biases, with an activation energy of ~330 meV that corresponds very closely to the values measured before annealing (Figure 5.4b), while no resonance is observed for negative gate biases. On the right, the resonance for positive biases has frozen out at T=102 K while the capacitance at positive biases is still close to C_{ox}, showing no signs of thermal activation. The capacitance at zero applied bias is interesting because it shows a fairly constant slope at all frequencies, indicating the interface states have a wide spectrum of energies.

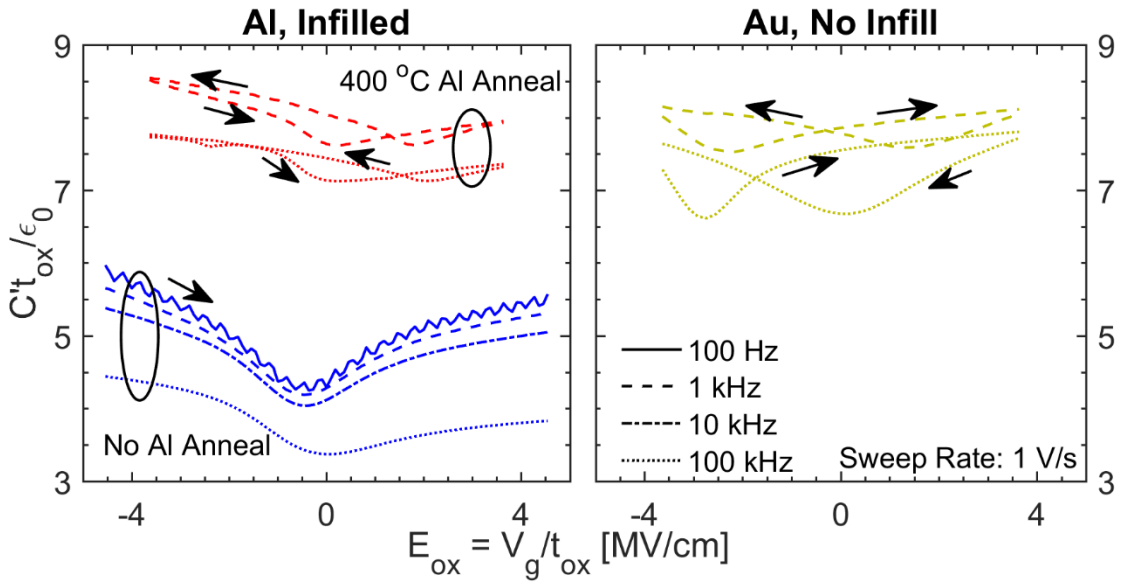

Figure 5.5: C-V measurements for Ge NC FETs.

In all cases the measured depletion width ranges from $< d_{NC}$ to $\sim 2d_{NC}$, depending on the assumed value of dielectric constant ranging between $\varepsilon_{NC} = \varepsilon_{Ge} = 16$ and $\varepsilon_{NC} = 2$ obtained from conservative estimates of the Maxwell-Garnett effective medium approximation (see Equation 2.5). As a result of this large depletion capacitance, it is a reasonably good approximation to assume $C_{NC} = C_{ox}$ for all NC FETs.

This approximation is physically reasonable due to the high density of states in the quantized orbitals of the NCs and the high concentration of surface states that would be expected in such a device, which is also supported by the large hysteresis in the C-V and I-V measurements, although this is reduced in devices that have been passivated with ALD infill.

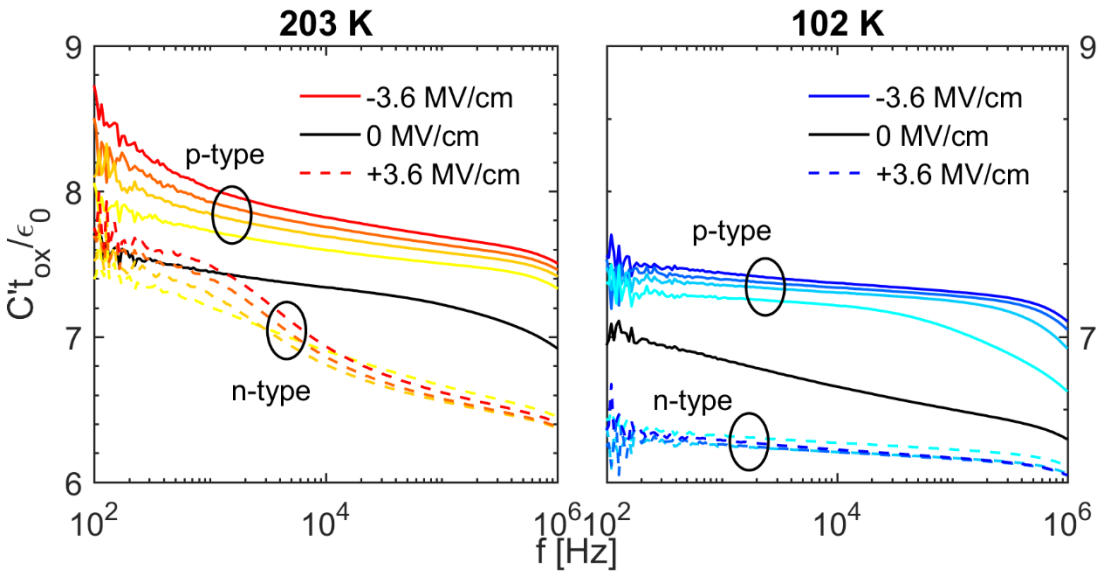

Figure 5.6: Capacitance spectra for Ge NC FET with Al contacts annealed at 400 °C at 203 K (left) and 102 K (right). No activation (frequency response) is observed for holes, while the electron response has a similar activation energy as before contact annealing

With this understanding, we can now look back at the data in Figure 5.4 for further understanding. The decreasing energy with gate bias, either towards the valence band or conduction band depending on sample preparation, represents a lowering of the charge injection barrier to the surface layer, as discussed. With proper contact preparation, such as annealing of Al contacts, this barrier can drop low enough to effective provide an ohmic contact. However, the activation energy in the FET off state remains. This activation energy is correlated with the activation energy for surface trap emission in the NC surface layer as shown in Figure 5.7. The larger energies associated with lower annealing temperatures are indicative of a large bandgap and a surface potential that is highly pinned near mid-gap by high concentrations of surface states. As the annealing temperature is increased, the bandgap decreases slightly due to grain growth and improved NC coupling decreasing the confinement potential. In addition, the mid-gap states

are reduced such that the Fermi-level is less closely pinned to mid-gap and can be moved further towards the band edge.

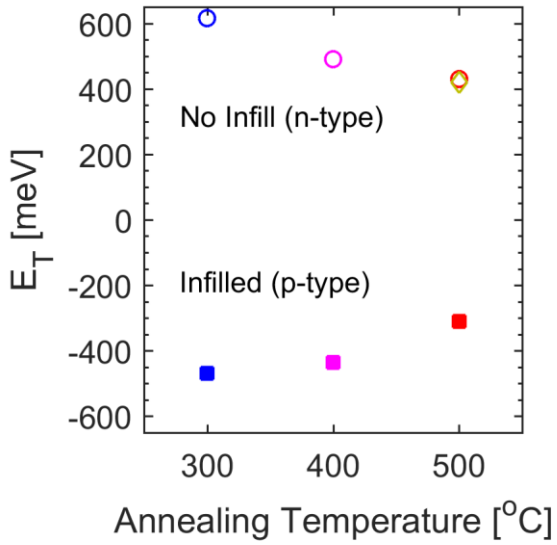

Figure 5.7: Surface trap energy for Ge NC FETs without infill (open symbols) and with infill (filled) for annealing temperatures of 300, 400, and 500 °C.

The mobility of devices with annealed Al contacts, both with and without infill, are observed to follow an Arrhenius dependence as $\frac{\partial ln\sigma}{\partial T} \propto \frac{\partial ln\mu}{\partial T} = -\frac{E_a}{k_B T}$ under the assumption that all conduction, independent of gate bias/carrier concentration, proceeds via nearest-neighbor hopping (NNH). This would be expected under the condition of low carrier concentrations and/or weak coupling between NCs. Ignoring the obvious hysteresis in our measurements and using only the data collected sweeping towards greater carrier concentration (i.e. increasing $|V_g - V_{th}|$), we find a linear relationship between current and gate bias, as shown in Figure 5.8. This measured mobility is observed to follow an Arrhenius dependence as $ln\mu \propto -\frac{1}{T}$, indicating NNH is the dominant charge transport mechanism with an activation energy of 100 meV for holes in infilled NCs and increasing to 175 meV for electrons in uncoated NCs. A common model for this NNH energy is the coulomb charging energy of the NCs within the dielectric medium of the film, given in Equation 2.4 as $E_c = e^2/4\pi\varepsilon_0\varepsilon_{eff}d_{NC}$. For a 6 nm diameter NC, the effective dielectric constant would need to be $\varepsilon_{eff} = 2.4$ to achieve a charging energy as great as 100 meV. This

would be somewhat surprising for the infilled NC film, as this value corresponds more closely to the Maxwell-Garnett approximation for Ge NCs in a void (no infill).

This might suggest that the infill is largely incomplete at the NC/gate insulator interface, leading to a smaller dielectric constant and larger charging energy. Of course, this energy alone is not strong evidence for this model, so further work is needed. However, the hysteresis observed in the infilled device, while significantly reduced from the devices with no infill, is still indicative of a large trap state concentration. A porous or low-quality of infill in the channel layer would result in a high density of interface states, so this seems like a plausible explanation. It is also suggested[78] that, in the presence of strong Fermi pinning due to a high concentration of mid-gap states, the activation energy would be $E_a = 2E_c$. In this scenario the necessary dielectric constant would be $\varepsilon_{eff} = 4.8$, which is an improvement, but still suggests an infill density well below 100% solid fraction at the interface. An inverted device structure, with the gate on top of the NC film, may be one way to investigate this, as the infill in the channel layer (top layer) would be certainly of higher quality, although other characteristics, particularly surface roughness, may limit any gains.

There are also other potential sources of energetic barriers to be consider. One likely example is the disorder energy, describing the variation in NC bandgap energy due to size distribution. Bulk Ge has a bandgap of 0.67 eV. The first quantized level has a $1/r^2$ dependence. Absorption measurements for Ge NCs with a diameter of 6 nm show a weak feature due to the indirect transition at approximately 1.1-1.2 eV, an increase of approximately 0.3-0.4 eV due to confinement. Assuming a 10% standard deviation in NC diameter, we can estimate the variation in band position to be on the order of 100 meV, which would be a significant contribution to the measured transport behavior and help explain some or all of the discrepancy between the activation energy and the charging energy often used to model it. It is likely that the larger activation energies are related to the higher concentration of traps in unpassivated NCs, but more work will be needed to explore this.

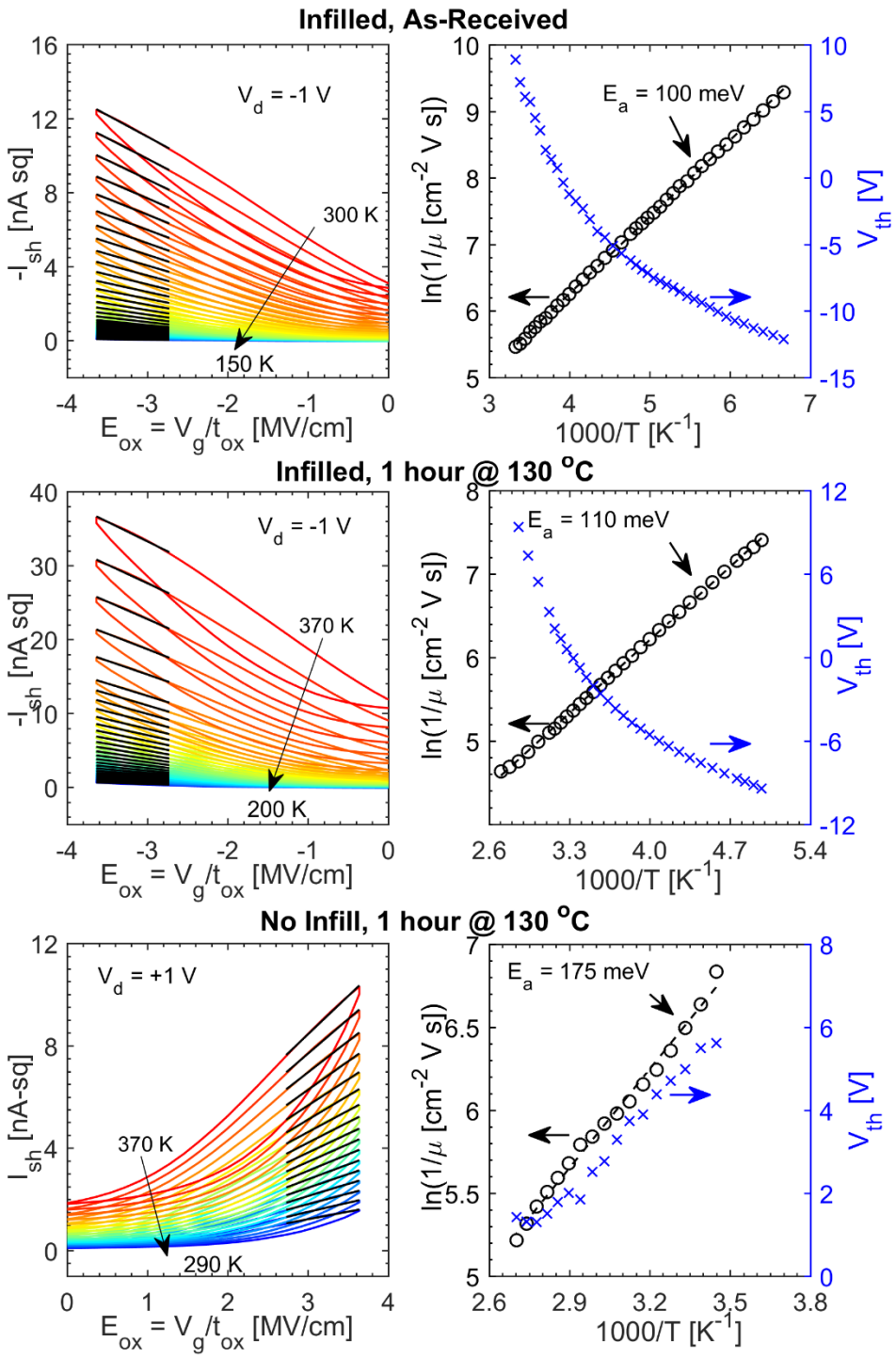

Figure 5.8: Measurements of Ge NC FET annealed at 500 °C, infilled with ALD Al_2O_3, and Al contacts annealed at 400 °C. (Left) Transfer curves with linear fits for mobility (black lines). (Right) Arrhenius plots of mobility as a function of temperature with measured activation energies (black). Threshold voltages are the x-intercepts of the linear fits of the transfer curves, which show a strong temperature dependence (blue).

Briefly, it is worth discussing an alternative way to analyze FET data that could produce interesting results, but does not seem to be relevant in the current work. We could choose to analyze each gate bias independently as a function of temperature. As long as the drain bias is kept low enough that the device is maintained in the linear regime, we can say $\frac{\partial I_d(V_g)}{\partial V_d}\frac{L}{W} = G_{sh}(V_g) = \frac{1}{R_{sh}(V_g)}$ and use these sheet resistance values to analyze the temperature-dependent conduction as a function of gate bias. This is shown in Figure 5.9 for the same device shown earlier with Al contacts and full Al_2O_3 infill at gate biases ranging from +20 V to -20 V. At positive or zero bias, activated conduction is observed with $ln\ R_{sh} \propto \frac{1}{T}$ and activation energies in the range of 250-300 meV, similar to TAS energies in this bias regime. As the gate bias becomes increasingly negative, the temperature dependence no longer follows the T^{-1} activation/NNH model, but instead changes to $T^{-0.46}$ at -10 V and $T^{-0.21}$ at -20 V. This could be taken as evidence of Efros-Shklovskii and Mott variable range hopping, respectively. However, both models assume a constant density of states at the Fermi level, with no change as a function of temperature. The measured threshold voltage shown in Figure 5.8 show a very strong dependence on temperature. By definition, $Q' = \int C' dV_g$ and the measured capacitance (Figure 5.5) is, to within a factor of ~10%, constant with voltage, allowing us to approximate $\Delta Q' = C'_{ox}\Delta V_g$. The threshold voltage is defined as the gate voltage at which current goes to zero, implying that the free charge carrier density goes to zero, $Q'_{free}(V_g = V_{th}) = 0$. From this we can define the charge density as a function of gate bias as

$$Q'_{free}(V_g) = C'_{ox}[V_g - V_{th}] - \Delta Q'_{trap} \tag{5.2}$$

The only way for this free carrier density to be constant with changing threshold voltage is for the corresponding trap filling $\Delta Q'_{trap}$ to change by an equal amount. Of course, it is also possible that the assumption implied in this analysis of a constant mobility is incorrect. Specifically, if the temperature dependence of the mobility is not constant with gate bias, the current $I_d(V_g = V_{th})$ could drop to zero, even as the population of carriers remains unchanged, implying that $\mu(V_g = V_{th}) = 0$, essentially

meaning that carriers at a given energy cannot universally be described as "free" or "trapped", but that this definition has a temperature dependence.

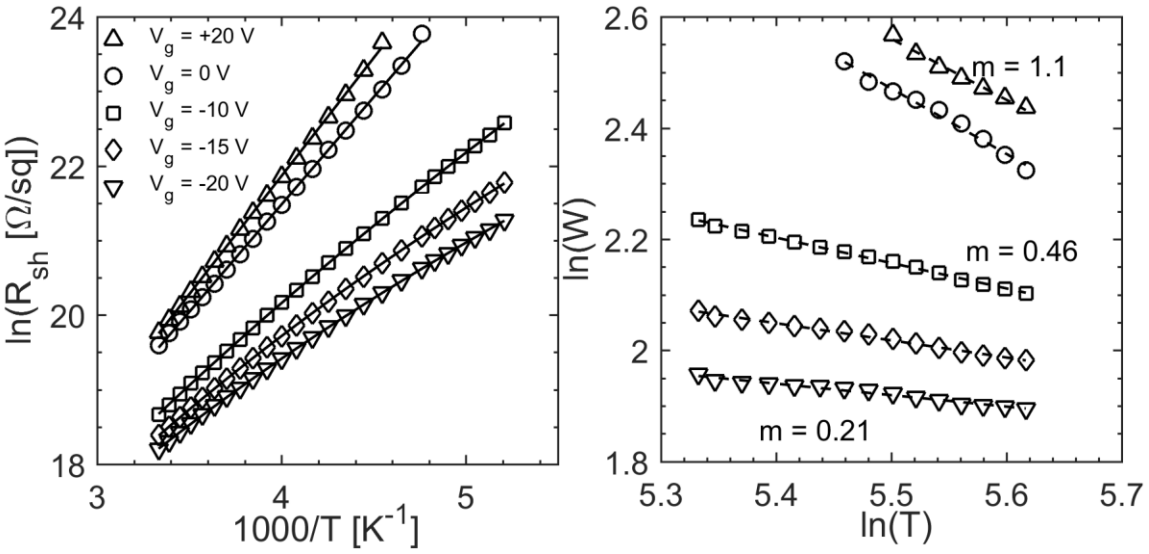

Figure 5.9: Arrhenius plots of sheet resistance in a Ge NC FET infilled with ALD Al_2O_3 showing an apparent transition from NNH to M-VRH. Further analysis shows that this is most likely not real but an artifact of the analysis assumptions.

This model is not consistent, however, with our previous analysis of the temperature dependence of the mobility extracted from the slope of the transfer curves. That analysis will almost certainly lead to an underestimate of the true mobility by assuming that $\Delta Q'_{trap} = 0$ and $Q' = Q'_{free}$, implying an effective mobility that can be stated as $\mu_{eff} \equiv \mu \frac{\tau}{\tau+\tau_{tr}}$ with τ and τ_{tr} the time constants for conduction and trapping, respectively.[196–199] However, as long as the slope $\frac{d\Delta Q'_{trap}}{dV_g}$ does not have a strong temperature dependence, this analysis remains valid. We have found good linear fits to the data over the bias range from $V_g = -15\,V \; to \; -20\,V$ with an Arrhenius dependence over the full range of temperatures, implying that our measurements are consistent with this model. In this case, the apparent observation of VRH at negative gate biases is simply an artifact of increasing carrier concentration at high temperatures. This is demonstrated in Figure 5.10, which shows the same sheet resistance data (over a wider temperature range) from Figure 5.9 along with calculated sheet resistances using the mobility values from Figure 5.8 and assumed values for threshold voltage offset, corresponding nominally to 1, 5, and 10 holes per NC.

The data for V_g = -20 V approaches the calculated line at low temperatures, while the lower biases deviate towards infinite resistance as the current levels approach zero at low temperatures. All measured values converge at high temperatures as the relative differences in threshold voltage offset converge.

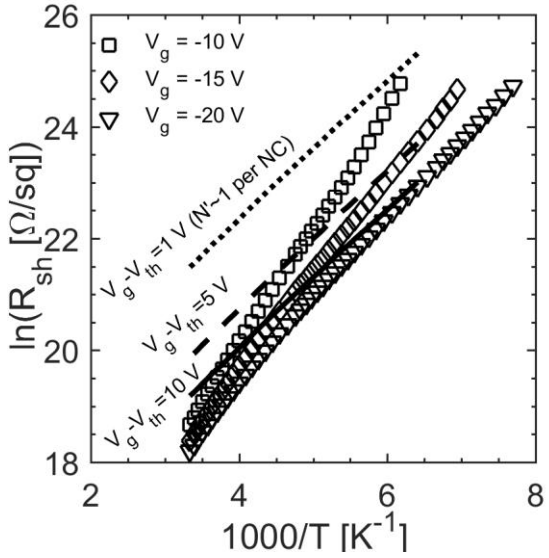

Figure 5.10: Ge NC FET sheet resistance vs temperature at gate biases of -10 V to -20 V (markers) along with the sheet resistances calculated using the mobility values in Figure 5.8 at different assume values of V_{th}. The sheet resistance at V_g = -20 V approaches the calculated value for V_g-V_{th} = 10 V at low temperatures.

5.4 Conclusion

In summary, we have demonstrated the ability to change the majority carrier type in Ge NC films from n-type to p-type by infilling with ALD Al_2O_3. This process changes polarity of conduction in FET devices fabricated using Ge NC films annealed at 500 °C, with the polarity determined by the majority carrier type of the film underneath the contacts and not by the channel material itself. This suggests that the with ALD infilling, the Ge NC channel can be gated into electron or hole accumulation, consistent with earlier work reporting ambipolar conduction in Ge NC FETs annealed at 500 °C, although without ALD infilling. In our measurements, ambipolar conduction is not observed, however. We attribute this limitation to barriers to minority charge injection from the upper NC layers to the bottom channel layer, as the work function of the metal contact does not make a significant difference to the conductivity. Electron conduction is observed in films without infill or with infill performed after contact deposition,

resulting in a channel that is doped p-type and an p-n junction forming between the NC layers underneath the source/drain contacts where the infill does not penetrate. If the infill is performed before contact deposition, then these contacts become p-type, and hole conduction is observed with a barrier now forming for electron injection. These FET observations are supported by our TAS measurements which show large barriers for minority carrier injection on the order of 10-20 $k_B T$.

5.5 Future Work

This work is still in the early stages and is intended as a starting point for future students to continue. We have learned a great deal about the need to account for the contacts in Ge NC FETs, even for large channel lengths. By understanding this key aspect of the device design, future students will hopefully be better equipped to use FET devices to investigate the fundamental charge transport phenomena in NC films. There are several experiments that are of immediate interest that should have great potential for immediate results to drive further research. The purpose of this section is to provide a summary of these ideas and details to help guide future work.

Four-contact FET

If the main goal is to remove the effect of contacts, rather than trying to understand more about the origin of our observations, then the most obvious and effective solution is to pattern a device with four contacts, two source contacts and two drain contacts. In this setup, the effects of contact resistance can be removed entirely by performing a four-point measurement (technically five-point with the gate) where one pair of source/drain contacts are used for driving current and the other pair used for sensing voltage. This may not be desirable from an ease of processing and measurement standpoint, but it should guarantee accurate measurement of the channel resistance. If pre-patterned electrodes (see below) are being used anyways, then the processing differences are trivial and it only requires relatively simple adjustments to

the measurement setup. Ultimately, however, learning more about where these contacts effects originate may be of as much or greater interest.

Pre-patterned Electrodes

While the device structure of a Au gate with ALD Al_2O_3 as a gate insulator was chosen for this work for the original purpose of minimizing oxide impedance for TAS measurements and has its advantages, a more typical NC FET device design consisting of a p+ or n+ Si wafer acting as a gate with 100-300 nm of thermal oxide as a gate insulator would probably be more effective and simpler to use and adapt for future work. Gate leakage was more of a concern than it needed to be with the current design, so having a thick SiO_2 gate dielectric would virtually eliminate these issues and allow the work to focus on the NC film properties themselves more easily.

In addition, using pre-patterned Au electrodes would be a good way to eliminate some of the film thickness and contact concerns that were reported here. This would allow for direct contact between the source/drain contacts and the surface layer itself, although it's certainly possible that this would then present its own difficulties. However, it would benefit from less uncertainty in the current pathway and fewer junctions to be concerned with.

Of course, Au electrodes would prevent annealing the NCs at temperatures beyond ~350 ˚C due to the Ge/Au eutectic point near this temperature. However, focusing on using ALD infill or other surface passivation, along with optimizing the film morphology to achieve high uniformity and density may mitigate the need for annealing to achieve reasonable conductivity. Ultimately, the NC films without annealing or with lower temperature annealing may be more interesting from a fundamental standpoint, anyways, so this deserves more attention, regardless.

Top Gate FET

Another interesting path that was attempted briefly, albeit crudely, without success but deserves further consideration is the development of a top gate FET. One of the main potential advantages of this device structure is that the active layer should be easily passivated by the ALD infilling process as compared to the bottom layer in a bottom gate FET. As a result, there may be far less hysteresis in the electrical measurements. Also, similar to the pre-patterned contacts discussed above, this would allow for direct contact between the metal and the channel layer, hopefully leading to higher conductivity and less difficulty.

This structure would consist of a NC film deposited onto any insulating substrate of convenience (oxidized wafer or polished glass would both work well). This deposition would be followed by ALD infilling, which is a potential drawback of this design, given that the NC film cannot be kept air-free and must be exposed to ALD to grow the gate insulator. However, in light of the conductivity and stability improvements observed with infilling, this is probably a beneficial processing step regardless, although its implications for oxidation and other surface chemical changes must be understood and accounted for.

After infilling, the thin layer of oxide that has formed on top of the NC film must be removed, as reported above. A dry etch would be very well suited to this, but in this work, a 500:1 solution of H_2O:BOE was used that yielded an etch rate of ~3 nm/min for Al_2O_3. A 2 minute etch was performed after ALD infilling with no discernible damage to the NC film. For a top gate device, the performance of which would depend greatly on film roughness, this step might have the additional benefit of smoothing the surface by lifting off and removing isolated NCs that protrude from the bulk of the film, reducing the overall roughness.

Related to that note, optimizing the deposition procedure, whether through controlled impaction or solution processing and spin coating, will be crucial for a high-performance device. Particularly for deposition from the gas-phase via impaction, surface thickness and roughness variations are common and difficult to control. This may or may not present a significant barrier to achieving a working device, but it

will be worth taking the time to understand and properly characterize this through SEM and AFM measurements before proceeding too far.

Finally, the gate insulator can be group with a second ALD step to any desired thickness, followed by gate deposition. Care must be taken with the gate deposition step, as most standard shadow masks will have a tendency to create small scratches in the thin gate insulator that will dramatically increase leakage or even lead to outright shorting. A specially designed shadow mask that keeps the mask/substrate contact area away from the deposition area is one method that has worked well. Otherwise, given that the entire film is at this point encased in ALD and protected from chemical or physical disruption, a standard lithographic patterning process could probably be safely and easily used.

Measurement Considerations

With these device design considerations accounted for, it is hoped that measurements will be more easily advanced. In particular, it would be very interesting to observe large changes in conduction behavior with gate bias, such as transitions to VRH and measurement of parameters like localization length and density of states. These transitions require large enough carrier concentrations and strong coupling between NCs, which should be possible if surface states can be adequately passivated and film morphology/density can be optimized. The increase in conductance of infilled films by multiple orders of magnitude over their non-infilled counterparts suggests that just a such an improvement is possible, although due to the nature of the current device geometry, it might have had only minimal impact on the trap concentration in the active area. It was also the original intent of this work to eventually add Ge/Si core/shell NCs, which would present an entirely new realm of possibilities and have not been studied electrically in any meaningful way. This should be a goal of any future work, as new material systems can yield a wide range of interesting results.

Beyond this, integrating optical excitation into FET measurements would provide an excellent way to probe NC electronic and photonic properties, which could easily be done with a top gate FET on glass or a bottom gate FET. If sufficient understanding of dark FET operation is achieved, this provides probably

the best route towards making further progress, as most of the most interesting NC phenomena involve their photonic properties, and these measurements might open up new pathways with a variety of materials.

References

(1) Liu, Y.; Tolentino, J.; Gibbs, M.; Ihly, R.; Perkins, C. L.; Liu, Y.; Crawford, N.; Hemminger, J. C.; Law, M. *Nano Lett.* **2013**, 130307111258007.

(2) Holman, Z. C.; Liu, C.-Y.; Kortshagen, U. R. *Nano Lett.* **2010**, *10* (7), 2661–2666.

(3) Chung, D. S.; Lee, J.-S.; Huang, J.; Nag, A.; Ithurria, S.; Talapin, D. V. *Nano Lett.* **2012**, *12* (4), 1813–1820.

(4) Talapin, D. V.; Murray, C. B. *Science* **2005**, *310* (5745), 86–89.

(5) Talapin, D. V.; Lee, J.-S.; Kovalenko, M. V.; Shevchenko, E. V. *Chem. Rev.* **2010**, *110* (1), 389–458.

(6) Liu, C.-Y.; Holman, Z. C.; Kortshagen, U. R. *Nano Lett.* **2008**, *9* (1), 449–452.

(7) Kim, S.-K.; Cho, C.-H.; Kim, B.-H.; Park, S.-J.; Won Lee, J. *Appl. Phys. Lett.* **2009**, *95* (14), 143120.

(8) Tang, J.; Kemp, K. W.; Hoogland, S.; Jeong, K. S.; Liu, H.; Levina, L.; Furukawa, M.; Wang, X.; Debnath, R.; Cha, D.; et al. *Nat. Mater.* **2011**, *10* (10), 765–771.

(9) Shirasaki, Y.; Supran, G. J.; Bawendi, M. G.; Bulović, V. *Nat. Photonics* **2012**, *7* (1), 13–23.

(10) Wood, V.; Bulović, V. *Nano Rev.* **2010**, *1* (0).

(11) Wang, R. Y.; Feser, J. P.; Lee, J.-S.; Talapin, D. V.; Segalman, R.; Majumdar, A. *Nano Lett.* **2008**, *8* (8), 2283–2288.

(12) Fan, F.-J.; Yu, B.; Wang, Y.-X.; Zhu, Y.-L.; Liu, X.-J.; Yu, S.-H.; Ren, Z. *J. Am. Chem. Soc.* **2011**, *133* (40), 15910–15913.

(13) Yang, H.; Jauregui, L. A.; Zhang, G.; Chen, Y. P.; Wu, Y. *Nano Lett.* **2012**, *12* (2), 540–545.

(14) Ibáñez, M.; Luo, Z.; Genç, A.; Piveteau, L.; Ortega, S.; Cadavid, D.; Dobrozhan, O.; Liu, Y.; Nachtegaal, M.; Zebarjadi, M.; et al. *Nat. Commun.* **2016**, *7*, 10766.

(15) R. Heath, J. *Chem. Soc. Rev.* **1998**, *27* (1), 65.

(16) Yin, Y.; Alivisatos, A. P. *Nature* **2005**, *437* (7059), 664–670.

(17) Murray, C. B.; Sun, S.; Gaschler, W.; Doyle, H.; Betley, T. A.; Kagan, C. R. *IBM J. Res. Dev.* **2001**, *45* (1), 47–56.

(18) Hines, M. A.; Scholes, G. D. *Adv. Mater.* **2003**, *15* (21), 1844–1849.

(19) Park, J.; An, K.; Hwang, Y.; Park, J.-G.; Noh, H.-J.; Kim, J.-Y.; Park, J.-H.; Hwang, N.-M.; Hyeon, T. *Nat. Mater.* **2004**, *3* (12), 891.

(20) Peng, X.; Wickham, J.; Alivisatos, A. P. *J. Am. Chem. Soc.* **1998**, *120* (21), 5343–5344.

(21) Talapin, D. V.; Rogach, A. L.; Kornowski, A.; Haase, M.; Weller, H. *Nano Lett.* **2001**, *1* (4), 207–211.

(22) Fan, H.; Yang, K.; Boye, D. M.; Sigmon, T.; Malloy, K. J.; Xu, H.; López, G. P.; Brinker, C. J. *Science* **2004**, *304* (5670), 567–571.

(23) Harfenist, S. A.; Wang, Z. L.; Alvarez, M. M.; Vezmar, I.; Whetten, R. L. *J. Phys. Chem.* **1996**, *100* (33), 13904–13910.

(24) Parthasarathy, R.; Lin, X.-M.; Jaeger, H. M. *Phys. Rev. Lett.* **2001**, *87* (18), 186807.

(25) Shabaev, A.; Efros, A. L.; Efros, A. L. *Nano Lett.* **2013**, *13* (11), 5454–5461.

(26) Korgel, B. A.; Fullam, S.; Connolly, S.; Fitzmaurice, D. *J. Phys. Chem. B* **1998**, *102* (43), 8379–8388.

(27) Jurbergs, D.; Rogojina, E.; Mangolini, L.; Kortshagen, U. *Appl. Phys. Lett.* **2006**, *88* (23), 233116–233116.

(28) Kovalenko, M. V.; Scheele, M.; Talapin, D. V. *Science* **2009**, *324* (5933), 1417–1420.

(29) Lee, J.-S.; Kovalenko, M. V.; Huang, J.; Chung, D. S.; Talapin, D. V. *Nat. Nanotechnol.* **2011**, *6* (6), 348.

(30) Norris, D. J.; Efros, A. L.; Erwin, S. C. *Science* **2008**, *319* (5871), 1776–1779.

(31) Hages, C. J.; Carter, N. J.; Moore, J.; McLeod, S. M.; Miskin, C. K.; Joglekar, C.; Lundstrom, M. S.; Agrawal, R. Device Comparison of Champion Nanocrystal-Ink Based CZTSSe and CIGSSe Solar Cells: Capacitance Spectroscopy; IEEE, 2013; pp 1966–1971.

(32) Milliron, D. J. *Nat. Mater.* **2014**, *13* (8), 772–773.

(33) Sun, X.; Hages, C. J.; Carter, N. J.; Moore, J. E.; Agrawal, R.; Lundstrom, M. Characterization of Nanocrystal-Ink Based CZTSSe and CIGSSe Solar Cells Using Voltage-Dependent Admittance Spectroscopy. In *2014 IEEE 40th Photovoltaic Specialist Conference (PVSC)*; 2014; pp 2416–2418.

(34) Bozyigit, D.; Yarema, O.; Wood, V. *Adv. Funct. Mater.* **2013**, *23* (24), 3024–3029.

(35) Kang, B.-H.; Kim, D.-E.; Yeom, S.-H.; Kim, K.-J.; Seo, J.-S.; Kim, J.-H.; Kong, S.-H.; Lee, J.-H.; Kwon, D.-H.; Kang, S.-W. Fabrication of Organic/Inorganic LED Device Using Nanocrystal Quantum Dots as Active Layer. In *Nano/Micro Engineered and Molecular Systems (NEMS), 2010 5th IEEE International Conference on*; IEEE, 2010; pp 832–835.

(36) Anikeeva, P. O.; Halpert, J. E.; Bawendi, M. G.; Bulović, V. *Nano Lett.* **2009**, *9* (7), 2532–2536.

(37) Barillaro, G.; Strambini, L. M. *Appl. Phys. Lett.* **2014**, *104* (9), 091102.

(38) Cheng, K.-Y.; Anthony, R.; Kortshagen, U. R.; Holmes, R. J. *Nano Lett.* **2010**, *10* (4), 1154–1157.

(39) Schlamp, M. C.; Peng, X.; Alivisatos, A. P. *J. Appl. Phys.* **1997**, *82* (11), 5837.

(40) Bisri, S. Z.; Piliego, C.; Yarema, M.; Heiss, W.; Loi, M. A. *Adv. Mater.* **2013**, *25* (31), 4309–4314.

(41) Lai, Y.; Li, H.; Kim, D. K.; Diroll, B. T.; Murray, C. B.; Kagan, C. R. *ACS Nano* **2014**, *8* (9), 9664–9672.

(42) Nugraha, M. I.; Häusermann, R.; Bisri, S. Z.; Matsui, H.; Sytnyk, M.; Heiss, W.; Takeya, J.; Loi, M. A. *Adv. Mater.* **2015**, *27* (12), 2107–2112.

(43) Turk, M. E.; Choi, J.-H.; Oh, S. J.; Fafarman, A. T.; Diroll, B. T.; Murray, C. B.; Kagan, C. R.; Kikkawa, J. M. *Nano Lett.* **2014**, *14* (10), 5948–5952.

(44) Swisher, S. L.; Volkman, S. K.; Subramanian, V. *ACS Appl. Mater. Interfaces* **2015**, *7* (19), 10069–10075.

(45) Swisher, S. L.; Volkman, S.; Braam, K.; Jang, J.; Subramanian, V. High Performance Solution-Processed Thin-Film Transistors Based on In 2 O 3 Nanocrystals. In *Device Research Conference (DRC), 2012 70th Annual*; IEEE, 2012; pp 241–242.

(46) Liu, Y.; Gibbs, M.; Puthussery, J.; Gaik, S.; Ihly, R.; Hillhouse, H. W.; Law, M. *Nano Lett.* **2010**, *10* (5), 1960–1969.

(47) Kortshagen, U. *J. Phys. Appl. Phys.* **2009**, *42* (11), 113001.

(48) Greenberg, B. L.; Ganguly, S.; Held, J. T.; Kramer, N. J.; Mkhoyan, K. A.; Aydil, E. S.; Kortshagen, U. R. *Nano Lett.* **2015**, *15* (12), 8162–8169.

(49) Liptak, R. W.; Devetter, B.; Thomas Iii, J. H.; Kortshagen, U.; Campbell, S. A. *Nanotechnology* **2009**, *20* (3), 035603.

(50) Pi, X. D.; Liptak, R. W.; Campbell, S. A.; Kortshagen, U. *Appl. Phys. Lett.* **2007**, *91* (8), 083112–083112.

(51) Holman, Z. C.; Kortshagen, U. R. *Nano Lett.* **2011**, *11* (5), 2133–2136.

(52) Rao, N. P.; Tymiak, N.; Blum, J.; Neuman, A.; Lee, H. J.; Girshick, S. L.; McMurry, P. H.; Heberlein, J. *J. Aerosol Sci.* **1998**, *29* (5), 707–720.

(53) Thimsen, E.; Johnson, M.; Zhang, X.; Wagner, A. J.; Mkhoyan, K. A.; Kortshagen, U. R.; Aydil, E. S. *Nat. Commun.* **2014**, *5*, 5822.

(54) Mangolini, L.; Thimsen, E.; Kortshagen, U. *Nano Lett.* **2005**, *5* (4), 655–659.

(55) Felbier, P.; Yang, J.; Theis, J.; Liptak, R. W.; Wagner, A.; Lorke, A.; Bacher, G.; Kortshagen, U. *Adv. Funct. Mater.* **2014**, *24* (14), 1988–1993.

(56) Gresback, R.; Holman, Z.; Kortshagen, U. *Appl. Phys. Lett.* **2007**, *91* (9), 093119.

(57) Chen, T. Electrical Transport in Thin Films of Doped Silicon Nanocrystals. PhD Dissertation, University of Minnesota, 2015.

(58) Pourret, A.; Guyot-Sionnest, P.; Elam, J. W. *Adv. Mater.* **2009**, *21* (2), 232–235.

(59) Liu, Y.; Gibbs, M.; Perkins, C. L.; Tolentino, J.; Zarghami, M. H.; Bustamante, J.; Law, M. *Nano Lett.* **2011**, *11* (12), 5349–5355.

(60) Greenberg, B. L. Conductive Networks of Plasma-Synthesized Zinc Oxide Nanocrystals. PhD Dissertation, University of Minnesota, 2017.

(61) Greenberg, B. L.; Robinson, Z. L.; Reich, K. V.; Gorynski, C.; Voigt, B. N.; Francis, L. F.; Shklovskii, B. I.; Aydil, E. S.; Kortshagen, U. R. *Nano Lett.* **2017**, *17* (8), 4634–4642.

(62) Skinner, B.; Chen, T.; Shklovskii, B. I. *Phys. Rev. B* **2012**, *85* (20).

(63) Pi, X. D.; Liptak, R. W.; Nowak, J. D.; Wells, N. P.; Carter, C. B.; Campbell, S. A.; Kortshagen, U. *Nanotechnology* **2008**, *19* (24), 245603.

(64) Vanmaekelbergh, D.; Liljeroth, P. *Chem. Soc. Rev.* **2005**, *34* (4), 299.

(65) Chen, T.; Skinner, B.; Xie, W.; Shklovskii, B. I.; Kortshagen, U. R. *J. Phys. Chem. C* **2014**, *118* (34), 19580–19588.

(66) Anderson, P. W. *Phys. Rev.* **1958**, *109* (5), 1492.

(67) Mott, N. F. *J. Non-Cryst. Solids* **1972**, *8–10*, 1–18.

(68) Murray, C. B.; Kagan, C. R.; Bawendi, M. G. *Annu. Rev. Mater. Sci.* **2000**, *30* (1), 545–610.

(69) Chandler, R. E.; Houtepen, A. J.; Nelson, J.; Vanmaekelbergh, D. *Phys. Rev. B* **2007**, *75* (8).

(70) Brus, L. *J. Phys. Chem.* **1986**, *90* (12), 2555–2560.

(71) Remacle, F.; Levine, R. D. *ChemPhysChem* **2001**, *2* (1), 20–36.

(72) Kittel, C. *Introduction to Solid State Physics 6th Ed.*.; 1986.

(73) Choi, J.-H.; Fafarman, A. T.; Oh, S. J.; Ko, D.-K.; Kim, D. K.; Diroll, B. T.; Muramoto, S.; Gillen, J. G.; Murray, C. B.; Kagan, C. R. *Nano Lett.* **2012**, *12* (5), 2631–2638.

(74) Maxwell, J. C.; Niven, W. D. (William D. *A Treatise on Electricity and Magnetism*; Oxford, Clarendon Press, 1881.

(75) Reich, K. V.; Shklovskii, B. I. *Appl. Phys. Lett.* **2016**, *108* (11), 113104.

(76) Sareni, B.; Krähenbühl, L.; Beroual, A.; Brosseau, C. *J. Appl. Phys.* **1996**, *80* (3), 1688–1696.

(77) Medeiros-Ribeiro, G.; Ohlberg, D. A. A.; Williams, R. S.; Heath, J. R. *Phys. Rev. B* **1999**, *59* (3), 1633.

(78) Shklovskii, B. I.; Efros, A. L. *Electronic Properties of Doped Semiconductors*; Springer Science & Business Media, 2013; Vol. 45.

(79) Miller, A.; Abrahams, E. *Phys. Rev.* **1960**, *120* (3), 745.

(80) Mott, N. *Conduction in Non-Crystalline Materials*, 2nd ed.; Clarendon Press: Oxford, 1993.

(81) Kang, M. S.; Sahu, A.; Norris, D. J.; Frisbie, C. D. *Nano Lett.* **2011**, *11* (9), 3887–3892.

(82) Kang, M. S.; Sahu, A.; Norris, D. J.; Frisbie, C. D. *Nano Lett.* **2010**, *10* (9), 3727–3732.

(83) Mentzel, T. S.; Porter, V. J.; Geyer, S.; MacLean, K.; Bawendi, M. G.; Kastner, M. A. *Phys. Rev. B* **2008**, *77* (7).

(84) Morgan, N. Y.; Leatherdale, C. A.; Drndić, M.; Jarosz, M. V.; Kastner, M. A.; Bawendi, M. *Phys. Rev. B* **2002**, *66* (7).

(85) Romero, H. E.; Drndic, M. *Phys. Rev. Lett.* **2005**, *95* (15).

(86) Mott, N. F. *J. Non-Cryst. Solids* **1968**, *1* (1), 1–17.

(87) Efros, A. L.; Shklovskii, B. I. *J. Phys. C Solid State Phys.* **1975**, *8* (4), L49.

(88) Shockley, W.; Read Jr, W. T. *Phys. Rev.* **1952**, *87* (5), 835.

(89) Hall, R. N. *Phys. Rev.* **1951**, *83*, 228.

(90) Hall, R. N. *Phys. Rev.* **1952**, *87* (2), 387.

(91) Anthony, R. J.; Rowe, D. J.; Stein, M.; Yang, J.; Kortshagen, U. *Adv. Funct. Mater.* **2011**, *21* (21), 4042–4046.

(92) Almeida, A. J.; Sahu, A.; Riedinger, A.; Norris, D. J.; Brandt, M. S.; Stutzmann, M.; Pereira, R. N. *J. Phys. Chem. C* **2016**, *120* (25), 13763–13770.

(93) Bozyigit, D.; Volk, S.; Yarema, O.; Wood, V. *Nano Lett.* **2013**, *13* (11), 5284–5288.

(94) Bozyigit, D.; Wood, V. *J. Mater. Chem. C* **2014**, *2* (17), 3172.

(95) Bozyigit, D.; Jakob, M.; Yarema, O.; Wood, V. *ACS Appl. Mater. Interfaces* **2013**, *5* (8), 2915–2919.

(96) Bozyigit, D.; Lin, W. M. M.; Yazdani, N.; Yarema, O.; Wood, V. *Nat. Commun.* **2015**, *6*, 6180.

(97) Nagpal, P.; Klimov, V. I. *Nat. Commun.* **2011**, *2*, 486.

(98) Kang, M. S.; Lee, J.; Norris, D. J.; Frisbie, C. D. *Nano Lett.* **2009**, *9* (11), 3848–3852.

(99) Law, M.; Luther, J. M.; Song, Q.; Hughes, B. K.; Perkins, C. L.; Nozik, A. J. *J. Am. Chem. Soc.* **2008**, *130* (18), 5974–5985.

(100) Chen, T.; Reich, K. V.; Kramer, N. J.; Fu, H.; Kortshagen, U. R.; Shklovskii, B. I. *Nat. Mater.* **2015**.

(101) Frenkel, J. *Phys. Rev.* **1938**, *54* (8), 647.

(102) Hartke, J. L. *J. Appl. Phys.* **1968**, *39* (10), 4871–4873.

(103) Shklovskii, B. I. HOPPING CONDUCTION IN SEMICONDUCTORS SUBJECTED TO A STRONG ELECTRIC FIELD. In *Sov Phys Semicond*; 1973.

(104) Houtepen, A. J.; Kockmann, D.; Vanmaekelbergh, D. *Nano Lett.* **2008**, *8* (10), 3516–3520.

(105) Oberhoff, D.; Pernstich, K. P.; Gundlach, D. J.; Batlogg, B. *IEEE Trans. Electron Devices* **2007**, *54* (1), 17–25.

(106) Bard, A. J.; Faulkner, L. R. *Electrochem. Methods* **2001**, *2*, 482.

(107) Liu, H.; Pourret, A.; Guyot-Sionnest, P. *ACS Nano* **2010**, *4* (9), 5211–5216.

(108) Roest, A. L.; Kelly, J. J.; Vanmaekelbergh, D.; Meulenkamp, E. A. *Phys. Rev. Lett.* **2002**, *89* (3).

(109) Roest, A. L.; Germeau, A.; Kelly, J. J.; Vanmaekelbergh, D.; Allan, G.; Meulenkamp, E. A. *ChemPhysChem* **2003**, *4* (9), 959–966.

(110) Wehrenberg, B. L.; Yu, D.; Ma, J.; Philippe. *J. Phys. Chem. B* **2005**, *109* (43), 20192–20199.

(111) Yu, D.; Wang, C.; Wehrenberg, B. L.; Guyot-Sionnest, P. *Phys. Rev. Lett.* **2004**, *92* (21).

(112) Yu, D.; Wehrenberg, B. L.; Jha, P.; Ma, J.; Guyot-Sionnest, P. *J. Appl. Phys.* **2006**, *99* (10), 104315.

(113) Lang, D. V. *J. Appl. Phys.* **1974**, *45* (7), 3023.

(114) Lang, D. V. *J. Appl. Phys.* **1974**, *45* (7), 3014.

(115) Lang, D. V. Space-Charge Spectroscopy in Semiconductors. In *Thermally Stimulated Relaxation in Solids*; Springer, 1979; pp 93–133.

(116) Borsuk, J. A.; Swanson, R. M. *IEEE Trans. Electron Devices* **1980**, *27* (12), 2217–2225.

(117) Kwon, Y. H.; Park, C. J.; Lee, W. C.; Fu, D. J.; Shon, Y.; Kang, T. W.; Hong, C. Y.; Cho, H. Y.; Wang, K. L. *Appl. Phys. Lett.* **2002**, *80* (14), 2502.

(118) Souifi, A.; Brounkov, P.; Bernardini, S.; Busseret, C.; Militaru, L.; Guillot, G.; Baron, T. *Mater. Sci. Eng. B* **2003**, *102* (1–3), 99–107.

(119) Engström, O.; Kaniewska, M.; Kaczmarczyk, M.; Jung, W. *Appl. Phys. Lett.* **2007**, *91* (13), 133117.

(120) Guan, W.; Long, S.; Liu, M.; Li, Z.; Hu, Y.; Liu, Q. *J. Phys. Appl. Phys.* **2007**, *40* (9), 2754–2758.

(121) Antonova, I.; Neustroev, E.; Smagulova, S.; Jedrzejewski, J. *Phys. Status Solidi C* **2009**, *6* (12), 2704–2706.

(122) Henan, N.; Liangcai, W.; Zhitang, S.; Chun, H. *J. Semicond.* **2009**, *30* (11), 114003.

(123) Antonova, I. V.; Smagulova, S. A.; Neustroev, E. P.; Skuratov, V. A.; Jedrzejewski, J.; Savir, E.; Balberg, I. *Semiconductors* **2011**, *45* (5), 582–586.

(124) Antonova, I. V.; Popov, V. I.; Smagulova, S. A.; Jedrzejewski, J.; Balberg, I. *J. Appl. Phys.* **2013**, *113* (8), 084308.

(125) Lv, T.; Zhao, L. *J. Nanomater.* **2014**, *2014*, 1–6.

(126) Nicollian, E. H.; Goetzberger, A. *Bell Syst. Tech. J.* **1967**, *46* (6), 1055–1133.

(127) Nicollian, E. H.; Brews, J. R. *MOS (Metal Oxide Semiconductor) Physics and Technology*; Wiley New York et al., 1982; Vol. 1987.

(128) Engel-Herbert, R.; Hwang, Y.; Stemmer, S. *J. Appl. Phys.* **2010**, *108* (12), 124101.

(129) Haddara, H. S.; El-Sayed, M. *Solid-State Electron.* **1988**, *31* (8), 1289–1298.

(130) Hafez, I. M.; Ghibaudo, G.; Balestra, F. *J. Appl. Phys.* **1990**, *67* (4), 1950.

(131) Jeon, S.; Park, S. *Microelectron. Eng.* **2011**, *88* (6), 872–876.

(132) Lehovec, K. *Appl. Phys. Lett.* **1966**, *8* (2), 48.

(133) Martens, K.; Wang, W.; De Keersmaecker, K.; Borghs, G.; Groeseneken, G.; Maes, H. *Microelectron. Eng.* **2007**, *84* (9–10), 2146–2149.

(134) Martens, K.; Chui, C. O.; Brammertz, G.; De Jaeger, B.; Kuzum, D.; Meuris, M.; Heyns, M.; Krishnamohan, T.; Saraswat, K.; Maes, H. E.; et al. *IEEE Trans. Electron Devices* **2008**, *55* (2), 547–556.

(135) Schulz, M.; Johnson, N. M. *Solid State Commun.* **1978**, *25* (7), 481–484.

(136) Weber, J. R.; Janotti, A.; Van de Walle, C. G. *J. Appl. Phys.* **2011**, *109* (3), 033715.

(137) Losee, D. L. *J. Appl. Phys.* **1975**, *46* (5), 2204.

(138) Barbolla, J.; Duenas, S.; Bailon, L. *Solid-State Electron.* **1992**, *35* (3), 285–297.

(139) Huang, W.; Peng, J.; Wang, L.; Wang, J.; Cao, Y. *Appl. Phys. Lett.* **2008**, *92* (1), 013308.

(140) Ip, A. H.; Thon, S. M.; Hoogland, S.; Voznyy, O.; Zhitomirsky, D.; Debnath, R.; Levina, L.; Rollny, L. R.; Carey, G. H.; Fischer, A.; et al. *Nat. Nanotechnol.* **2012**, *7* (9), 577–582.

(141) Jin, Z.; Wang, A.; Zhou, Q.; Wang, Y.; Wang, J. *Sci. Rep.* **2016**, *6* (1).

(142) Markovich, G.; Collier, C. P.; Heath, J. R. *Phys. Rev. Lett.* **1998**, *80* (17), 3807.

(143) Panthani, M. G.; Kurley, J. M.; Crisp, R. W.; Dietz, T. C.; Ezzyat, T.; Luther, J. M.; Talapin, D. V. *Nano Lett.* **2014**, *14* (2), 670–675.

(144) Ellmer, K. *J. Phys. Appl. Phys.* **2001**, *34* (21), 3097.

(145) Wang, Z. L. *J. Phys. Condens. Matter* **2004**, *16* (25), R829–R858.

(146) Cui, J. *Mater. Charact.* **2012**, *64* (Supplement C), 43–52.

(147) Wang, Z. L. *Annu. Rev. Phys. Chem.* **2004**, *55* (1), 159–196.

(148) Gao, P. X.; Wang, Z. L. *Appl. Phys. Lett.* **2004**, *84* (15), 2883–2885.

(149) Baxter, J. B.; Schmuttenmaer, C. A. *J. Phys. Chem. B* **2006**, *110* (50), 25229–25239.

(150) Hendry, E.; Koeberg, M.; O'Regan, B.; Bonn, M. *Nano Lett.* **2006**, *6* (4), 755–759.

(151) Davies, J. H. *Philos. Mag. B* **1985**, *52* (3), 511–520.

(152) Davies, J. H. *J. Phys. C Solid State Phys.* **1984**, *17* (17), 3031.

(153) Zabrodskii, A. G. *Philos. Mag. B* **2001**, *81* (9), 1131–1151.

(154) Efros, A. L. *J. Phys. C Solid State Phys.* **1976**, *9* (11), 2021.

(155) Rosenbaum, R. *Phys. Rev. B* **1991**, *44* (8), 3599.

(156) Zhang, J.; Shklovskii, B. I. *Phys. Rev. B* **2004**, *70* (11), 115317.

(157) Zhang, Y.; Dai, O.; Levy, M.; Sarachik, M. P. *Phys. Rev. Lett.* **1990**, *64* (22), 2687.

(158) Moreira, H. S.; Sampaio, J. F.; Alves, E. S.; de Oliveira, A. G. *Phys. Rev. Lett.* **1998**, *80* (8), 1706.

(159) Arginskaya, N. V.; Kozub, V. I. *Zh Eksp Teor Fiz* **1994**, *106*, 848–859.

(160) Melnick, D. A. *J. Chem. Phys.* **1957**, *26* (5), 1136–1146.

(161) Collins, R. J.; Thomas, D. G. *Phys. Rev.* **1958**, *112* (2), 388–395.

(162) Medved, D. B. *J. Chem. Phys.* **1958**, *28* (5), 870–873.

(163) Medved, D. B. *J. Phys. Chem. Solids* **1961**, *20* (3–4), 255–267.

(164) Heiland, G. *J. Phys. Chem. Solids* **1961**, *22*, 227–234.

(165) Doerffler, W.; Hauffe, K. *J. Catal.* **1964**, *3* (2), 156–170.

(166) Shapira, Y.; Cox, S. M.; Lichtman, D. *Surf. Sci.* **1976**, *54* (1), 43–59.

(167) Bonasewicz, P. *J. Electrochem. Soc.* **1986**, *133* (11), 2270.

(168) Takahashi, Y.; Kanamori, M.; Kondoh, A.; Minoura, H.; Ohya, Y. *Jpn. J. Appl. Phys.* **1994**, *33* (Part 1, No. 12A), 6611–6615.

(169) Patil, S. A.; Hwang, H.-J.; Yu, M.-H.; Shrestha, N. K.; Kim, H.-S. *RSC Adv.* **2017**, *7* (11), 6565–6573.

(170) Tamura, H.; Mita, K.; Tanaka, A.; Ito, M. *J. Colloid Interface Sci.* **2001**, *243* (1), 202–207.

(171) Henrich, V. E.; Cox, P. A. *The Surface Science of Metal Oxides*; Cambridge University Press: Cambridge ; New York, 1994.

(172) Liu, P.; Kendelewicz, T.; Brown, G. E.; Parks, G. A. *Surf. Sci.* **1998**, *412*, 287–314.

(173) Zabrodskii, A.; Zinoveva, K. *Zh Eksp Teor Fiz* **1984**, *86*, 742.

(174) Boschloo, G.; Fitzmaurice, D. *J. Phys. Chem. B* **1999**, *103* (16), 3093–3098.

(175) Zum Felde, U.; Haase, M.; Weller, H. *J. Phys. Chem. B* **2000**, *104* (40), 9388–9395.

(176) Zandi, O.; Agrawal, A.; Shearer, A. B.; Gilbert, L. C.; Dahlman, C. J.; Staller, C. M.; Milliron, D. J. *ArXiv Prepr. ArXiv170907136* **2017**.

(177) Staller, C. M.; Robinson, Z. L.; Agrawal, A.; Gibbs, S. L.; Greenberg, B. L.; Lounis, S. D.; Kortshagen, U. R.; Milliron, D. J. *ArXiv Prepr. ArXiv180100731* **2018**.

(178) Li, J. V.; Crandall, R. S.; Repins, I. L.; Nardes, A. M.; Levi, D. H.; others. *Gavin J Nanomed Nanotechnol* **2016**, *2016*, 5–10.

(179) Gresback, R.; Kramer, N. J.; Ding, Y.; Chen, T.; Kortshagen, U. R.; Nozaki, T. *ACS Nano* **2014**, *8* (6), 5650–5656.

(180) Anthony, R. J.; Cheng, K.-Y.; Holman, Z. C.; Holmes, R. J.; Kortshagen, U. R. *Nano Lett.* **2012**, *12* (6), 2822–2825.

(181) Holman, Z. C.; Kortshagen, U. R. *Langmuir* **2009**, *25* (19), 11883–11889.

(182) Cheng, K.-Y.; Anthony, R.; Kortshagen, U. R.; Holmes, R. J. *Nano Lett.* **2011**, *11* (5), 1952–1956.

(183) Johnson, N. M.; Doland, C.; Ponce, F.; Walker, J.; Anderson, G. Hydrogen in Crystalline Semiconductors: A Review of Experimental Results. In *Hydrogen in Semiconductors*; Elsevier, 1991; pp 3–20.

(184) Van de Walle, C. G.; Neugebauer, J. *Nature* **2003**, *423* (6940), 626.

(185) Weber, J. R.; Janotti, A.; Rinke, P.; Van de Walle, C. G. *Appl. Phys. Lett.* **2007**, *91* (14), 142101.

(186) Troost, D. *J. Vac. Sci. Technol. B Microelectron. Nanometer Struct.* **1987**, *5* (4), 1119.

(187) Broqvist, P.; Alkauskas, A.; Pasquarello, A. *Phys. Rev. B* **2008**, *78* (7).

(188) Tsipas, P.; Dimoulas, A. *Appl. Phys. Lett.* **2009**, *94* (1), 012114.

(189) Clarke, E. N. *Phys. Rev.* **1953**, *91* (3), 756–757.

(190) Clarke, E. N. *Phys. Rev.* **1954**, *95* (1), 284–285.

(191) Clauws, P. *Mater. Sci. Eng. B* **1996**, *36* (1–3), 213–220.

(192) Holman, Z. C. Germanium Nanocrystal Solar Cells. PhD Dissertation, University of Minnesota, 2010.

(193) Dimoulas, A.; Tsipas, P.; Sotiropoulos, A.; Evangelou, E. K. *Appl. Phys. Lett.* **2006**, *89* (25), 252110.

(194) Strohm, A.; Matics, S.; Frank, W. Diffusion of Gold in Germanium. In *Defect and Diffusion Forum*; Trans Tech Publ, 2001; Vol. 194, pp 629–634.

(195) Bracht, H.; Stolwijk, N. A.; Mehrer, H. *Phys. Rev. B* **1991**, *43* (18), 14465.

(196) Podzorov, V.; Menard, E.; Borissov, A.; Kiryukhin, V.; Rogers, J. A.; Gershenson, M. E. *Phys. Rev. Lett.* **2004**, *93* (8).

(197) Podzorov, V.; Menard, E.; Rogers, J. A.; Gershenson, M. E. *Phys. Rev. Lett.* **2005**, *95* (22).

(198) Bube, R. H. *Photoconductivity of Solids*; RE Krieger Pub. Co., 1978.

(199) Jang, J.; Liu, W.; Son, J. S.; Talapin, D. V. *Nano Lett.* **2014**, *14* (2), 653–662.